AFRL-AFOSR-VA-TR-2015-0333

HETEROGENOUS MATERIAL INTEGRATION AND BAND ENGINEERING WITH TYPE II SUPERLATTICE

Sanjay Krishna
UNIVERSITY OF NEW MEXICO

10/26/2015
Final Report

DISTRIBUTION A: Distribution approved for public release.

Air Force Research Laboratory
AF Office Of Scientific Research (AFOSR)/ RTA1
Arlington, Virginia 22203
Air Force Materiel Command

REPORT DOCUMENTATION PAGE

Form Approved
OMB No. 0704-0188

The public reporting burden for this collection of information is estimated to average 1 hour per response, including the time for reviewing instructions, searching existing data sources, gathering and maintaining the data needed, and completing and reviewing the collection of information. Send comments regarding this burden estimate or any other aspect of this collection of information, including suggestions for reducing the burden, to Department of Defense, Washington Headquarters Services, Directorate for Information Operations and Reports (0704-0188), 1215 Jefferson Davis Highway, Suite 1204, Arlington, VA 22202-4302. Respondents should be aware that notwithstanding any other provision of law, no person shall be subject to any penalty for failing to comply with a collection of information if it does not display a currently valid OMB control number.
PLEASE DO NOT RETURN YOUR FORM TO THE ABOVE ADDRESS.

1. REPORT DATE *(DD-MM-YYYY)*

2. REPORT TYPE
Final

3. DATES COVERED *(From - To)*
04/15/2010-10/14/2015

4. TITLE AND SUBTITLE
"Heterogenous Material Integration and Band Engineering with Type II Superlattices"

5a. CONTRACT NUMBER

5b. GRANT NUMBER
FA9550-10-1-0113

5c. PROGRAM ELEMENT NUMBER

6. AUTHOR(S)
Prof. Sanjay Krishna

5d. PROJECT NUMBER

5e. TASK NUMBER

5f. WORK UNIT NUMBER

7. PERFORMING ORGANIZATION NAME(S) AND ADDRESS(ES)
The Regents of the University of New Mexico
1700 Lomas Blvd. NE, Suite 3100
The University of New Mexico
Albuquerque, NM 87131-0001

8. PERFORMING ORGANIZATION REPORT NUMBER

9. SPONSORING/MONITORING AGENCY NAME(S) AND ADDRESS(ES)
AF Office of Scientific Research
875 N. Randolph St. Room 3112
Arlington, VA 22203
Pamela M. Allison
pamela.allison.2@us.af.mil

10. SPONSOR/MONITOR'S ACRONYM(S)

11. SPONSOR/MONITOR'S REPORT NUMBER(S)

12. DISTRIBUTION/AVAILABILITY STATEMENT
DISTRIBUTION A

13. SUPPLEMENTARY NOTES

14. ABSTRACT
InAs/GaSb type-II strained layer superlattice (T2SL) detectors are of great importance for a variety of military and civil applications requiring increased resolution, reliability, and operating temperature, as well as lowered size, weight, power and cost. However, despite extensive efforts on T2SL material growth, detector passivation, and fabrication, T2SL detectors still have not reached the performance level of the Rule 07 for MCT detectors. During this program, the Center for High Technology Materials at the University of New Mexico was investigating high performance heterojunction bandgap engineered infrared focal plane arrays using InAs/GaSb/AlSb strained layer superlattices.

15. SUBJECT TERMS
crystal growth, characterization, semiconductor fabrication, infrared detectors, graphene, type-II superlattices

16. SECURITY CLASSIFICATION OF:			17. LIMITATION OF ABSTRACT	18. NUMBER OF PAGES	19a. NAME OF RESPONSIBLE PERSON
a. REPORT	b. ABSTRACT	c. THIS PAGE			Sanjay Krishna
					19b. TELEPHONE NUMBER *(Include area code)*
None	None	None		47	(505) 272-7800

DISTRIBUTION A: Distribution approved for public release.

INSTRUCTIONS FOR COMPLETING SF 298

1. REPORT DATE. Full publication date, including day, month, if available. Must cite at least the year and be Year 2000 compliant, e.g. 30-06-1998; xx-06-1998; xx-xx-1998.

2. REPORT TYPE. State the type of report, such as final, technical, interim, memorandum, master's thesis, progress, quarterly, research, special, group study, etc.

3. DATE COVERED. Indicate the time during which the work was performed and the report was written, e.g., Jun 1997 - Jun 1998; 1-10 Jun 1996; May - Nov 1998; Nov 1998.

4. TITLE. Enter title and subtitle with volume number and part number, if applicable. On classified documents, enter the title classification in parentheses.

5a. CONTRACT NUMBER. Enter all contract numbers as they appear in the report, e.g. F33315-86-C-5169.

5b. GRANT NUMBER. Enter all grant numbers as they appear in the report. e.g. AFOSR-82-1234.

5c. PROGRAM ELEMENT NUMBER. Enter all program element numbers as they appear in the report, e.g. 61101A.

5e. TASK NUMBER. Enter all task numbers as they appear in the report, e.g. 05; RF0330201; T4112.

5f. WORK UNIT NUMBER. Enter all work unit numbers as they appear in the report, e.g. 001; AFAPL30480105.

6. AUTHOR(S). Enter name(s) of person(s) responsible for writing the report, performing the research, or credited with the content of the report. The form of entry is the last name, first name, middle initial, and additional qualifiers separated by commas, e.g. Smith, Richard, J, Jr.

7. PERFORMING ORGANIZATION NAME(S) AND ADDRESS(ES). Self-explanatory.

8. PERFORMING ORGANIZATION REPORT NUMBER. Enter all unique alphanumeric report numbers assigned by the performing organization, e.g. BRL-1234; AFWL-TR-85-4017-Vol-21-PT-2.

9. SPONSORING/MONITORING AGENCY NAME(S) AND ADDRESS(ES). Enter the name and address of the organization(s) financially responsible for and monitoring the work.

10. SPONSOR/MONITOR'S ACRONYM(S). Enter, if available, e.g. BRL, ARDEC, NADC.

11. SPONSOR/MONITOR'S REPORT NUMBER(S). Enter report number as assigned by the sponsoring/ monitoring agency, if available, e.g. BRL-TR-829; -215.

12. DISTRIBUTION/AVAILABILITY STATEMENT. Use agency-mandated availability statements to indicate the public availability or distribution limitations of the report. If additional limitations/ restrictions or special markings are indicated, follow agency authorization procedures, e.g. RD/FRD, PROPIN, ITAR, etc. Include copyright information.

13. SUPPLEMENTARY NOTES. Enter information not included elsewhere such as: prepared in cooperation with; translation of; report supersedes; old edition number, etc.

14. ABSTRACT. A brief (approximately 200 words) factual summary of the most significant information.

15. SUBJECT TERMS. Key words or phrases identifying major concepts in the report.

16. SECURITY CLASSIFICATION. Enter security classification in accordance with security classification regulations, e.g. U, C, S, etc. If this form contains classified information, stamp classification level on the top and bottom of this page.

17. LIMITATION OF ABSTRACT. This block must be completed to assign a distribution limitation to the abstract. Enter UU (Unclassified Unlimited) or SAR (Same as Report). An entry in this block is necessary if the abstract is to be limited.

DISTRIBUTION A: Distribution approved for public release.

University of New Mexico
Report to Fulfill the No Cost Extension Request for the Contract FA9550-10-1-0113
PI: Sanjay Krishna
Project Title: Heterogeneous Material Integration and Band Engineering with Type-II Superlattices

1.0 Table of Contents

1.0 Table of Contents....1
2.0 Overview....1
2.1 Background....1
2.2 Technical Approach....1
3.0 Results and Discussion....2
3.1. Heterojunction Bandgap Engineered Detectors....2
3.1.1. Unipolar Barrier Superlattice Detectors with pBiBn Architecture....2
3.1.2. Unipolar Barrier Superlattice Detectors with Cascade Design for MWIR Detection....4
3.2. Systematic Study of Dark Current Mechanisms....7
3.2.1. Interface optimization in MWIR T2SL structures....7
3.2.2. Optimization of Growth Conditions in LWIR T2SL structures....10
3.2.3. Photocapacitance Study of T2SL Defect Levels....12
3.2.4. Vertical mobility in InAs/GaSb superlattices....14
3.2.5 Carrier Lifetime Studies in InAs/GaSb MWIR T2SLs....16
3.2.6. InAs/InAsSb SL Structures for Improved Carrier Lifetime....18
3.2.7. Growth on (111) GaSb to Improve the Hole Confinement and Operating Temperature....20
3.3. Multimodal Sensing....24
3.3.1 Plasmonic Focal Plane Array....24
3.3.2 Three Color T2SL Detectors....25
3.3.3 Dual-band T2SL Detectors....26
3.4 Heterogeneous Material Integration....27
3.4.1. *Imaging with Metamaterial Spatial Light Modulators (SLM)*....27
3.4.2. Semiconductor Nano-scale Transistors on Insulating Layers....28
3.4.3. MWIR T2SL Detectors Integrated with Plasmonic Coupler....29
3.5 Passivation of T2SL Detectors....31
3.6 Large-Area Semiconducting Graphene Nanomesh Tailored by Interferometric Lithography....33
4.0 Papers published with the support of this grant....40
5.0 Bibliographical References....42

2.0 Overview

2.1 Background

InAs/GaSb type-II strained layer superlattice (T2SL) detectors are of great importance for a variety of military and civil applications requiring increased resolution, reliability, and operating temperature, as well as lowered size, weight, power and cost. T2SL detectors combine key advantages of InSb and Mercury-Cadmium-Telluride (MCT)-based technologies, namely, scalability of focal plane arrays (FPAs) fabrication to larger areas and high sensitivity. Moreover, a number of theoretically predicted advantages of T2SL over bulk MCT detectors, including lower tunneling currents [1] and suppressed Auger recombination rates [2], facilitates a higher operating temperature of T2SL-based imagers. Finally, T2SL technology benefits from a relatively easy growth procedure, mature III-V fabrication technology, and the commercial availability of substrates with good electro-optical homogeneity.

T2SL technology gained a lot of interest from AFRL Sensors, Space Vehicles and Materials Directorate and several AF programs needed for situational awareness endeavors. Moreover, an additional interest from Army Night Vision Laboratory and DARPA making T2SL technology an attractive option for a DoD wide tri-core service collaboration.

T2SL detectors have demonstrated tremendous progress in the past few years with low dark currents [3, 4, 5, 6], megapixel arrays [7, 8], and multicolor operation [9, 10]. Advances in heteroengineering of T2SL system resulted in excellent low temperature T2SL detector performance [11-16]. However, despite extensive efforts of various industrial and university laboratories on T2SL material growth, detector passivation, and fabrication, T2SL detectors still have not reached the performance level of the Rule 07 for MCT detectors especially at higher temperatures (>150 K) [17, 18].

2.2 Technical Approach

During this program, the Center for High Technology Materials (CHTM) at the University of New Mexico (UNM) was investigating high performance heterojunction bandgap engineered infrared (MWIR, 3-5μm/LWIR, 8-

DISTRIBUTION A: Distribution approved for public release.

12µm) focal plane arrays (FPA) using InAs/GaSb/AlSb strained layer superlattices (T2SL). Several sub-areas of development have been identified and methodically investigated for the realization of the *heterojunction bandgap engineered unipolar barrier detectors based on T2SL*:

1. Heterojunction Bandgap Engineered Detectors

A. Unipolar Barrier Superlattice Detectors with pBiBn Architecture
B. Unipolar Barrier Superlattice Detectors with Cascade Design for MWIR detection

2. Systematic Study of Dark Current Mechanisms

A. Interface optimization in MWIR T2SL structures
B. Optimization of growth conditions in LWIR T2SL structures
C. Photocapacitance study of T2SL defect levels
D. Vertical mobility in InAs/GaSb superlattices
E. InAs/InAsSb SL structures for improved carrier lifetime
F. Carrier Lifetime Studies in InAs/GaSb MWIR T2SLs
G. Growth on (111) GaSb to improve the hole confinement and operating temperature

3. Multimodal Sensing

A. Plasmonic Focal Plane Array
B. Dual-band T2SL detectors
C. Three color T2SL detectors

4. Heterogeneous Material Integration

A. Imaging with Metamaterial Spatial Light Modulators (SLM)
B. Semiconductor nano-scale transistors on insulating layers
C. MWIR T2SL detectors integrated with plasmonic coupler

5. Passivation of T2SL Detectors

3.0 Results and Discussion

In this section, the discuss in details each sub-area of research undertaken during the program for realization of program's ultimate goal, the high operating temperature FPA based on InAs/GaSb T2SL.

3.1. Heterojunction Bandgap Engineered Detectors

3.1.1. Unipolar Barrier Superlattice Detectors with pBiBn Architecture

An unipolar barrier engineered architecture called pBiBn, with electron (EB) and hole blocking (HB) barriers placed near the P type and N type contacts, respectively, has been proposed by UNM in 2010 [19]. The double-barrier heterostructure design (pBiBn) belongs to the family of band gap engineered T2SL architectures, such as nBn [20], M-structure [21], W-structure [22], N-structure [23], and complementary barrier infrared detector (CBIRD) [24]. The improved performance of these T2SL devices over the homojunction T2SL detectors is credited to reduction in dark current by use of current blocking layers either in conduction or valence bands which reduce one or several dark current components. The pBiBn design further reduces noise in T2SL-based detectors, since it contains wider bandgap potential barriers in both valence and conduction bands. In pBiBn detector design, the electron blocking (EB) layer sandwiched between P contact layer and absorber region blocks the minority carrier diffusion (electrons) current from P contact layer into the absorber region.

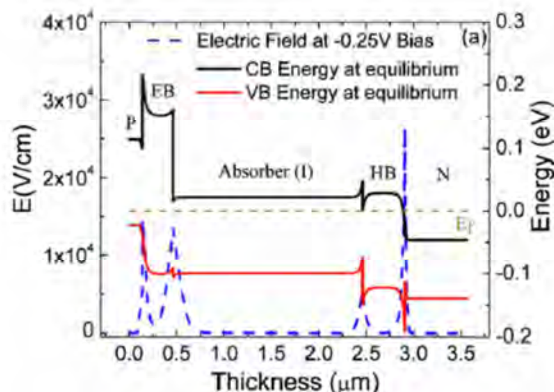

Figure 1. Equilibrium band diagram of T2SL detector with the pBiBn design showing conduction band (CB)

Similarly the hole blocking (HB) layer blocks minority carrier diffusion (holes) current from N contact layer into the absorber region. Moreover, the electric field drop across the active region is small as compared to a conventional PIN design since there is significant amount of field drop across the EB and HB layers, which have a wider band gap compared to the absorber region. This reduction in electric field leads to very small depletion region and hence reduction in the Schockley-Read-Hall (SRH) generation-recombination component of dark current. The tunneling currents are also reduced due to significant reduction in field drop. Thus the device can be made diffusion limited over wide range of operating temperatures, thereby improving the

DISTRIBUTION A: Distribution approved for public release.

and valence band (VB) at 77 K and electric field profile across the device at -0.25 V of applied bias [Gautam et al, Appl. Phys. Lett. 96, 231107, 2010]

performance of the device. The band diagram of T2SL detector with the pBiBn design biased under operational conditions is shown in Figure 1.

The MWIR pBiBn detector structure was grown on n-type GaSb substrate using a 400nm thick GaSb buffer layer. The bottom contact layer was made of 6 monolayers (ML) InAs/7ML GaSb T2SL, which was followed by the HB layer made of 11ML InAs/4ML AlSb T2SL. The absorber region was made of 1μm thick 9ML InAs/9ML GaSb
MWIR T2SL, which was followed by an EB layer made of 8ML GaSb/5ML AlSb superlattice. The top contact layer was composed by 5ML InAs/8ML AlSb T2SL. After MBE growth, the material was processed into single pixel detectors with 410 x 410 μm^2 mesa area with apertures ranging from 25-300 μm using inductively coupled plasma (ICP) dry etching. An ohmic contact was made by depositing Ti/Pt/Au on the bottom and top contact layers of the detectors.

The current-voltage relationship of this MWIR pBiBn device is shown in Figure 2 (a). A dark current density of 1.6 x 10^{-7}A/cm^2 and 6.8 x 10^{-2}A/cm^2 was measured at 80K and 200K, at an applied bias of -30mV and -80mV, respectively. Radiometric characterization was carried out using a calibrated black body source at 900K. Figure 2 (b) shows the variation of responsivity and measured detectivity as a function of temperature. The measured peak detectivity of 2.1 x 10^{11} cm-Hz$^{1/2}$/W, with 2π FOV and 300K background, was observed at -30mV, with a corresponding responsivity of 1.3A/W and quantum efficiency (QE) 38%

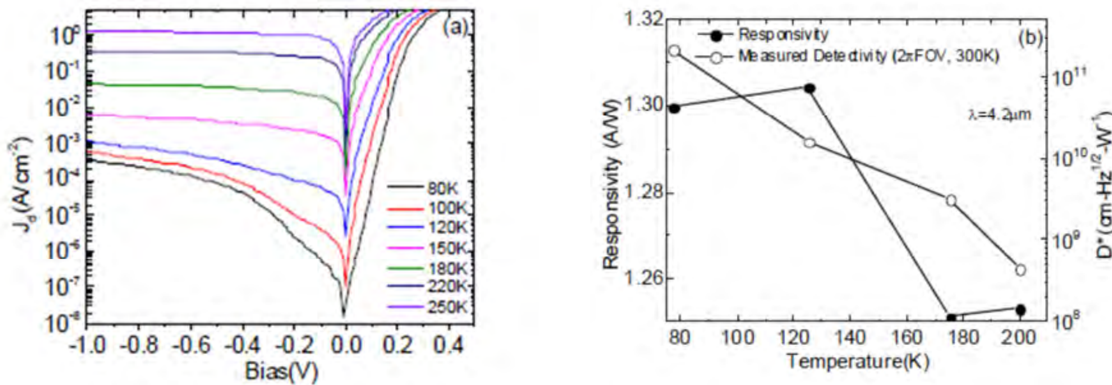

Figure 2. (a) Dark current density measured at various temperatures and (b) measured responsivity and peak detectivity at 2π FOV, 300K background as a function of temperature, at λ=4.2μm, for MWIR pBiBn T2SL detector [N. Gautam, PhD Thesis, 2012]

The InAs/GaSb T2SL LWIR detector with pBiBn design was also realized. Detector structure had 800 nm thick N contact layer made of 9 ML InAs/ 4ML GaSb doped with Te (n=3×10^{18} cm^{-3}) followed by non-intentionally doped (n.i.d) 275 nm thick hole blocking (hB) layer made of 16 ML InAs/ 4ML AlSb T2SL. This was followed by a 2 μm thick absorber region of 14ML InAs/ 7ML GaSb SLS (both T2SL layers were doped with Be, p = 1 x 10^{16} cm^{-3}) and an electron blocking (eB) layer of n.i.d 147 nm thick 7ML GaSb/ 84ML AlSb T2SL. A 130 nm thick 5ML InAs/ 8ML GaSb T2SL P contact layer doped with Be (p=2.8×10^{18} cm^{-3}) completed the structure. After MBE growth, the material was processed into single pixel detectors with 410 x 410 μm^2 mesa area with apertures ranging from 25-300 μm using ICP dry etching. An ohmic contact was made by depositing Ti/Pt/Au on the bottom and top contact layers of the detectors.

After electrical and radiometric characterization performed at CHTM, dark current densities of these LWIR pBiBn detectors have been evaluated at Raytheon Vision Systems (RVS) within 30-176K temperature range and results of representative device are shown in Figure 3 (a). At 76K, the dark current density was 1.6 x 10^{-5} A/cm^2 at -60 mV (the bias corresponds to the highest signal-to-noise ratio). The responsivity measurements were carried out at with 8.5 μm-11.5μm wide bandpass filter at 77K using a calibrated black-body source at 900K and a network analyzer. Figure 3 (b) shows measured responsivity and calculated quantum efficiency (QE), from responsivity data, at 8 μm wavelength. Without application of anti-reflection coating, single pass QE reached 35% at 0.5V of applied bias. Specific detectivity D* has been calculated based on noise measurements data, for 300K background and 2π field of view (FOV). At 0.5V of applied bias, value of D* was 2 x 10^{10} Jones.

DISTRIBUTION A: Distribution approved for public release.

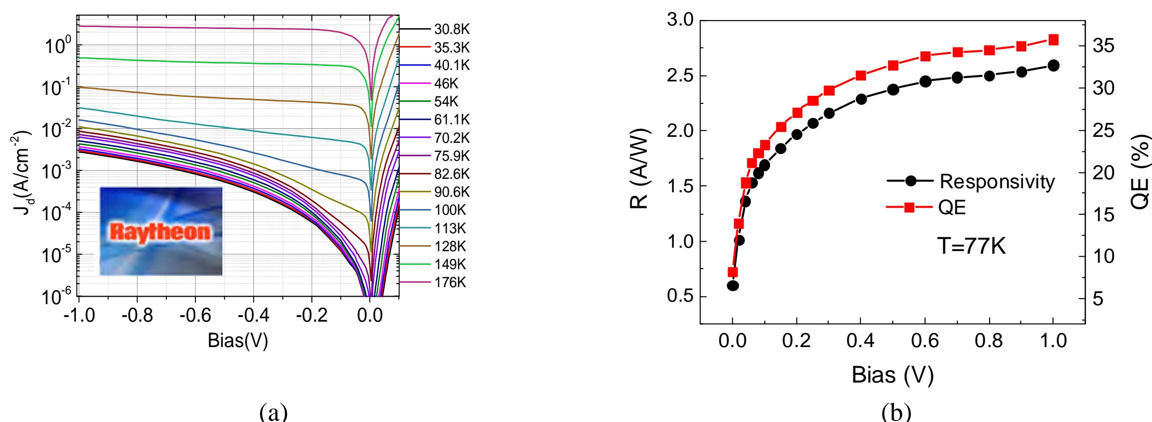

(a) (b)

Figure 3. (a) Temperature-dependent dark current density and (b) responsivity and QE values evaluated at 77K of pBiBn LWIR T2SL detector [N. Gautam, PhD Thesis, 2012]

Table 1. Performance of MWIR and LWIR pBiBn T2SL detectors

	MWIR at 4.2µm, -30mV	LWIR at 10µm, -0.5V
Dark current density at 77K (A/cm^2)	1.6 x 10^{-7}	6 x 10^{-3}
QE (%)	38	35
Specific Detectivity D* (Jones)	2.1 x 10^{11}	2.0 x 10^{10}

Summary of electric and radiometric performance of MWIR and LWIR T2SL detectors with pBiBn design is presented in Table 1. Dark current density, QE, and specific detectivity were evaluated at 77K and 4.2µm, and -30mV of applied bias (MWIR pBiBn detector), and 10µm and -0.5V of applied bias (LWIR pBiBn detector).

3.1.2. Unipolar Barrier Superlattice Detectors with Cascade Design for MWIR Detection

To improve operation temperature of MWIR T2SL detector structure, and further reduce dark current level, UNM proposed an interband cascade infrared photodetector (ICIP) structure. The 1st generation device consisted of a seven stage active region, with each stage comprised of an absorber region, relaxation region, and interband tunneling region. The absorber region was composed of a MWIR InAs/GaSb T2SL, the relaxation region formed by graded T2SL InAs/AlSb superlattice, and the interband tunneling region was made of a GaSb well in between AlSb barriers. The heterostructure schematic, calculated band diagram, and schematic of operating principle of ICIP MWIR structure is presented in Figure 4.

The device consisted of a bottom contact layer, composed of 12.5ML InAs/5ML AlSb T2SL, that is n+ doped with gallium telluride (GaTe) to a level of 3x10^{18} cm^{-3}. It was followed by seven cascade stages, which precede a 2 nm thick AlSb tunneling barrier, and then the top contact layer, made of GaSb (Pþ), doped at 3x10^{18} cm^{-3} with beryllium (Be). The absorber region is made MWIR 9ML InAs/9ML GaSb T2SL and is non-intentionally doped. The residual doping in MWIR T2SL at high temperatures was n-type[25]. All the layers except for contact layers were non-intentionally doped as well.

There are several key features in ICIP structure ensuring the improved device performance. In particular, the interband tunneling region in our device is designed so that the difference in hole energies is close to the longitudinal optical (LO) phonon energy in AlSb, to facilitate phonon-assisted tunneling. Next, our design has graded InAs/AlSb T2SL as the relaxation region, as transport through T2SL is more efficient. Finally, the Nþ contact layer is a wider bandgap 12.5 monolayers (ML) InAs/5ML AlSb superlattice, which can suppress dark current by reducing thermionic generation and tunneling currents.

In the photo-voltaic mode, photo-generation of electron hole pairs occur in the MWIR absorber region (1), and due to the built-in field, electrons move to the right while the holes move to the left. Electrons then relax in the graded SL transport region (3), while holes tunnel through region (2). The separation between the quantized energy level in the GaSb quantum well of region (2) and the valance band in region (1) was designed to be equal to the LO phonon energy in AlSb, to make the tunneling of holes a phonon-assisted process. The relaxation region (3) and the interband tunneling region (2) also act as hole and electron barriers, respectively, to block the flow of dark carriers

DISTRIBUTION A: Distribution approved for public release.

from one cascade stage into the other. The junction between regions (2) and (3) acts as recombination site for electrons and holes which leads to photoconductive (PC) gain being equal to 1/N, where N is the number of cascade stages. Reduction in photoconductive gain and zero bias operation are extremely desirable properties for FPAs to obtain a low noise equivalent temperature difference (NEdT) at a high operating temperature as it limits the rate at which the charge capacitor is filled. In the present design, the total thickness of the absorber is 1 um, and the absorption QE can be increased by increasing the number of stages. However the conversion QE is lower than that of the absorption QE by a factor of N.

The ICIP structure was grown on a n-type (Te) doped GaSb substrate by molecular beam epitaxy (MBE) technique. After MBE growth, the device fabrication was carried out using standard photolithography techniques and inductively coupled plasma (ICP) etching for mesa definition. Finally, a Ti/Pt/Au ohmic contact was deposited to form the top and bottom contacts. The devices were then passivated with silicon dioxide (SiO2) to reduce surface leakage currents.

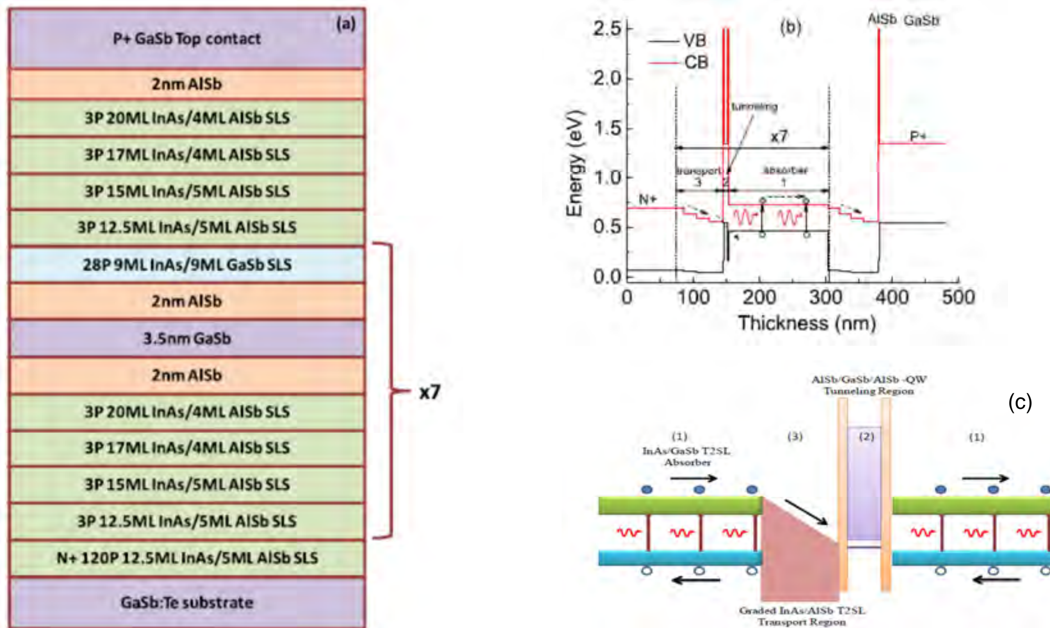

Figure 4. (a) Structural schematic, (b) calculated energy band-diagram, and (c) schematic of operating principle of the MWIR T2SL ICIP detector [Gautam *et al*, Appl. Phys. Lett. 101, 021106, 2012].

Spectral responses were undertaken from 77K to 420K, as shown in Figure 5. The 100% cutoff wavelength of 5.2 μm and 7 μm were observed at 77K and 420 K, respectively. Up to room temperature (RT), good signal to noise ratio (SNR) was observed at zero bias, while at 420K the highest SNR was obtained at 0.5V.

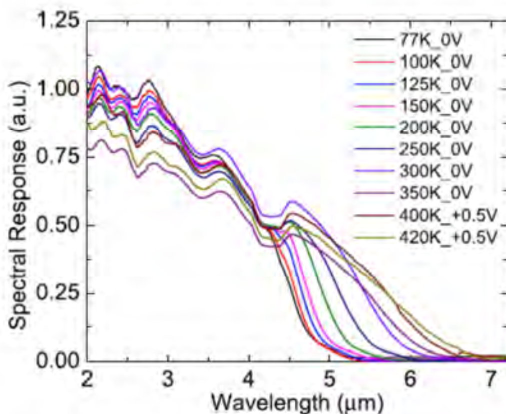

Figure 5. Measured photocurrent signal of MWIR T2SL ICIP detector as a function of temperature [Gautam *et*

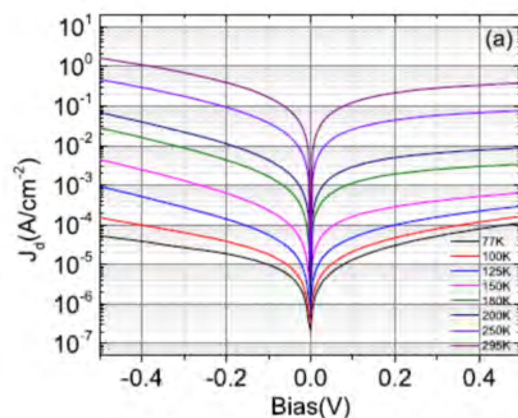

Figure 6. Dark current density as a function of bias for different temperatures in ICIP structure [Gautam *et al*,

DISTRIBUTION A: Distribution approved for public release.

al, Appl. Phys. Lett. 101, 021106, 2012]. Appl. Phys. Lett. 101, 021106, 2012].

The dark current density as a function of bias voltage has been shown in Figure 6. Dark current density of 3.6 x 10^{-7} A/cm^{-2} and 7.3 x 10^{-3} A/cm^{-2} has been measured at 77K and 295K, respectively, at -5mV of applied bias. The activation energy was extracted from the temperature-dependent dark current measurements at -5mV of applied bias. The dark current is dominated by tunneling, in the lower temperature range (70K–110 K), indicated by small activation energy of 15meV. While in the higher temperature range (130 K–250 K), the activation energy of 0.15 eV (~Eg/2), indicating that the dominant dark current mechanism is SRH recombination current. This is due to a more dramatic increase in SRH currents with temperature as compared to tunneling currents.

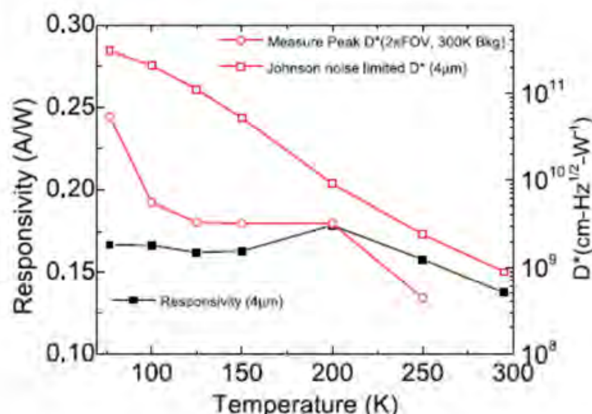

Figure 7. Measured responsivity, measured specific detectivity with 2p FOV (300K background) and Johnson noise limited detectivity as a function of temperature [Gautam *et al*, Appl. Phys. Lett. 101, 021106, 2012].

Detailed radiometric characterization was performed with a calibrated blackbody source at 900 K, and the detector placed inside a variable temperature cryostat with 2p FOV, 300K background. The measured responsivity (4 µm, -5mV) and specific detectivity, measured with 2p FOV (300K background) and calculated Johnson noise limited regime, are shown in Fig. 7 as a function of temperature.

At 77 K, measured detectivity was 5.3 x 10^{10} Jones and Johnson noise limited detectivity was 3.0 x 10^{11} Jones, while at 250 K, measured detectivity and Johnson noise limited detectivities were 4.4 x 10^{8} Jones and 2.4 x 10^{9} Jones, respectively. At room temperature, the Johnson noise limited detectivity was 8.9 x 10^{8} Jones.

2nd generation of MWIR cascade devices utilized the optimized band structure design and improved growth procedure.The samples were grown on p-type (Zn-doped) 2-inch (001) GaSb substrates with a solid-source molecular beam epitaxy (MBE) system. The absorber was composed of 30 periods (~140 nm) of non-intentionally doped InAs/GaSb (1.8 nm/2.7 nm) T2SL, the electron relaxation (eR) region consisted of InAs/Al(In)Sb coupled MQWs, and the electron transit (eT) region consisted of 4–6 pairs of GaSb/AlSb MQWs. The samples were first processed into single pixel devices to evaluate detector performance. Despite the relatively thin absorber, these MWIR single-pixel IC detectors were operational up to 450K under zero bias. The 50% cutoff wavelength was ~ 4.4 µm at 300 K. The dark current of the single pixel devices was as low as 1.10 x 10^{-7} A/cm^2 at -5mV and 150 K.

Next, T2SL material was fabricated into a 320 x 256 FPA, with pixel size of 24 x 24 µm^2 and pitch of 30 µm (filling factor 64%). UNM developed fabrication procedure for the 320x256 MWIR and LWIR FPAs. The front-side processing of 320 x 256 SLS FPA with 30µm pitch will start with inductively coupled plasma (ICP) -assisted definition of individual FPA pixels (24µm x 24µm). Etch depth will be precisely characterized using four additional test pixels with an area of 24µm x 24µm located at the boundary of the 320 x 256 FPA. Next, the contact metallization pads will be realized through e-beam evaporator and lift-off. UNM will use Ti/Pt/Au metal combination with 50nm/50nm/300nm thickness to ensure good Ohmic contact. After deposition of dielectric passivation, on each pixel passivation layer will be etched locally on top for the subsequent under bump metallization (UBM). UBM is needed to enable well defined indium bumps for the FPA hybridization with read-out integrated circuit (ROIC). UBM will be deposited in e-beam evaporator with composition and thickness of Ti/Ni/Au (30nm/150nm/50nm). Indium bumps with a thickness ~3µm will be thermally evaporated on UBM metal pads. Finally, wafers will be diced into individual 320x256 detector arrays.

After completion of the front-side processing, the 320x256 FPAs will be hybridized to an appropriate read-out integrated circuit (ROIC with standard flip-chip indium-bump technology. Next, complete removal of GaSb substrate will performed using a multi-stage process with combination of plasma-assisted and chemical etches. First, the majority of the substrate will removed by a chemical wet etch, thinning it from the starting thickness of 500µm down to approximately 20µm. Then, the remaining substrate will etched using a selective dry plasma etch, stopping

DISTRIBUTION A: Distribution approved for public release.

at the AlGaSb etch stop layer. Residues from the dry etch will be cleaned from the surface, and finally, the etch stop layer will be removed. Details of substrate removal procedure are outlined in Klein *et al* [26].

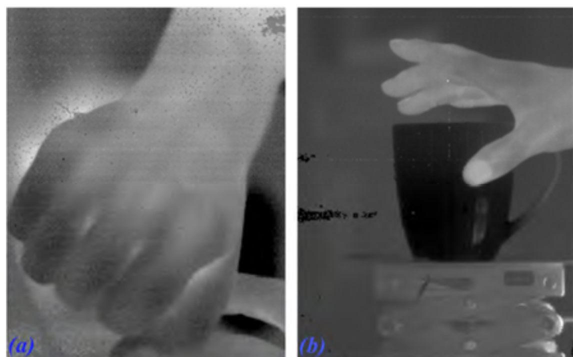

Figure 8. Infrared images acquired from IC FPAs operated at 80 K. Brighter areas indicate warmer regions. (a) is acquired from an IC FPA with 40 µm p-GaSb substrate; (b) is taken from an IC FPA with ~ 10 µm p-GaSb substrate [Tian *et al*, Appl. Phys. Lett. 105, 051109, 2014]

Fig. 8 shows the IR images acquired from IC FPAs at 80 K. A two-point non-uniformity correction (NUC, between 25°C and 32°C) was used to remove non-uniformity and fixed pattern noise between the pixels and read-out circuit, prior to image acquisition. Fig. 10 (a) is an IR image acquired from the first IC FPA with ~ 40 µm of p-GaSb substrate. The horizontal lines in the thermal image are due to the noise imposed by vibrations from the Sterling cooler. Since the p-type GaSb substrate is highly absorbent to the incoming IR photons, it will significantly reduce the overall SNR and thus the attainable NEDT. Fig. 8 (b) shows IR images acquired from an IC FPA with the GaSb substrate etched down to ~ 10 µm. The thermal image quality is significantly better than that shown in Fig. 8 (a).

The NEDT was measured by acquiring a sequence of 100 image scans with the IC FPAs exposed to a blackbody with varied temperatures. NEDT is then determined by the blackbody temperature difference divided by the SNR, where the noise is computed from the standard deviation of each individual pixel over 100 frames. Minimum NEDT (taken from top 1% pixels from a selected area in the 320 x 256 IC FPA, with over 8000 pixels) and mean NED for IC FPA with thinned to 10 µm substrate were 24 mK and 30 mK at 80 K, respectively.

3.2. Systematic Study of Dark Current Mechanisms

3.2.1. Interface optimization in MWIR T2SL structures

The large dark current demonstrated by T2SL MWIR and LWIR detectors is often attributed to the short SRH lifetime [27]. The nature of SRH centers responsible for the short lifetime is not very well understood yet. The presence of hundreds of interfaces in the T2SL sample could lead to formation of trap levels in the T2SL bandgap. Below we summarized UNM efforts to improve performance of T2SL detectors by optimizing the interfaces in T2SL stack.

SRH generation-recombination dark current is possibly caused by the presence of bandgap defect states and the interfacial states, owing to the interface roughness, which act as recombination sites for photogenerated carriers. This becomes particularly important because of non-common cation and anion interface between InAs and GaSb. The interface bonds between InAs and GaSb layers can be 'GaAs' or 'InSb' or mixed 'Ga-In-As-Sb' type bonds. One can control 'GaAs' or 'InSb' type bonds at the interfaces by the use of ultrathin GaAs/InSb layers or As_2/Sb_2 soak times.

The interface composition and abruptness in T2SL may be controlled with group V soak times, growth interruptions, or incorporation of thin layers of InSb or GaAs. In addition, the V/III beam equivalent pressure (BEP) flux ratio for both InAs and GaSb constituent layers implicitly influence the quality of interfaces. The excessive amount or deficiency of group V presented during T2SL growth will increase T2SL interface roughness, moreover, an excess of group V can incorporate into T2SL layers initiating change in net strain and potential impurities/vacancies generation. Enhanced number of scattering centers (interface roughness and impurities) will negatively affect photogenerated carrier transport, degrading the overall device performance. It has to be noted that due to the different layer thicknesses and growth conditions of MWIR and LWIR T2SL, the interfaces in these T2SL have to be optimized separately. We carried out systematic study to select the best interface structure for MWIR T2SL, and the detector performance has been the ultimate benchmark for the interface quality.

DISTRIBUTION A: Distribution approved for public release.

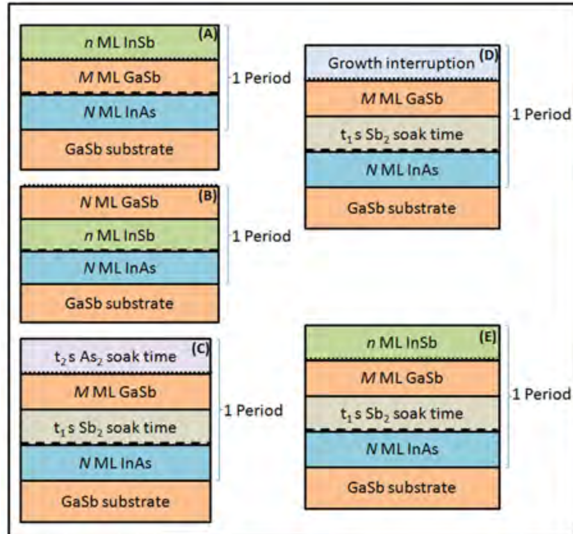

Figure 9. Different interface types studied for the optimization of MWIR detector performance; dotted and dashed lines represent tensile and compressive interfaces, respectively [N. Gautam, PhD Thesis, 2012]

Fig. 9 depicts various methods of interface control we utilized. In structure (A), tensile interface (that is "InAs on GaSb" interface) is forced to become InSb type by the growth of a 1ML InSb layer, while the compressive interface (that is "GaSb on InAs" interface) is uncontrolled. In structure (B), tensile interface is uncontrolled and compressive interface is InSb type. Structure (C) has been optimized with Sb_2 and As_2 soak times [28]. The idea behind this interface structure is to control both the interfaces of T2SL, by promoting InSb type bonds at compressive interface with Sb_2 soak time and GaAs type bonds at tensile interface with As_2 soak time. Structure (D) [29] has InSb type bonds at both the interfaces, where Sb_2 soak time has been used at compressive interface while growth interruption has been used at tensile interface. Finally, structure (E) has InSb like bonds at both the interfaces, similar to structure (D), but with the use InSb layer at tensile interface and Sb_2 soak time at compressive interface.

The samples for this study were grown by molecular beam epitaxy (MBE), in an elemental source VG SemiconV-80H MBE system equipped with valved As and Sb cracker sources, and Ga and In SUMO® cells. Epitaxial growth was carried out on GaSb:Te substrates. For all the samples in this study, GaSb buffer layer of thickness 500nm preceded the growth of T2SL structure. For T2SL growth, group V fluxes were adjusted so as to achieve V/III beam equivalent pressure (BEP) ratio equal to 4 for GaSb and 6.5 for InAs. GaSb buffer layer was grown at 500°C on pyrometer.

Room temperature PL spectra measured on MWIR T2SL material grown with interfaces A-E are shown in Fig. 10. These data reveals that the PL intensity of structure (C) is less than that of structure (A), which suggests that supporting "GaAs" type bonds reduce PL intensity and hence the optical quality of the structure. Structure (D) has a higher PL intensity compared to structures (A), (B) and (C). This indicates that "InSb'' type bonds at both the interfaces give better optical quality. However, soak times and growth interruptions lead to a significant increase in the growth time. Moreover, increased growth interruption time might deteriorate the quality of T2SL by encouraging incorporation of impurities during growth.

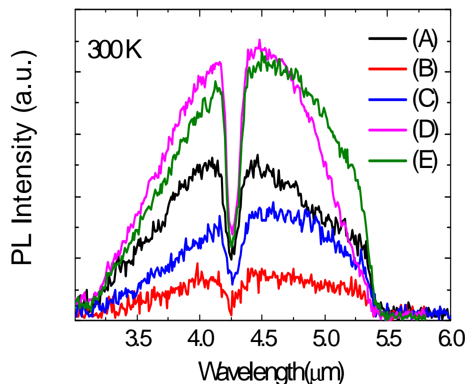

Figure 10. RT PL comparison of MWIR T2SL structure grown with five different methods of interface control [N. Gautam, PhD Thesis, 2012]

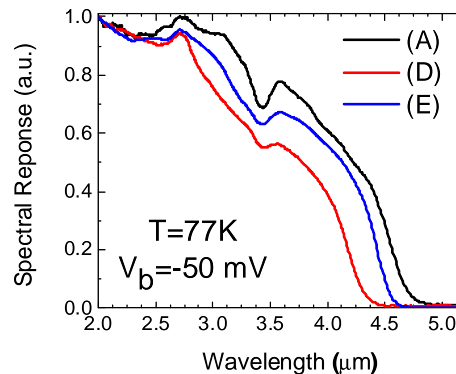

Figure 11. Comparison of normalized spectral response of three detector structures with interface (A), (D) and (E) at 77K and -50 mV of applied bias [N. Gautam, PhD Thesis, 2012]

DISTRIBUTION A: Distribution approved for public release.

Since the better interface quality in InAs/GaSb T2SL stack would imply better transport of photogenerated carriers and lower dark current, the impact of different interface structure on infrared detector performance was studied. Three homojunction PIN detectors with structure (A), (D) and (E) chosen for the best PL performance were grown. All three detectors consist of 150 periods thick 8 ML InAs/8 ML GaSb T2SL Te doped N contact layer (n = 3×10^{18} cm^{-3}), followed by 40 periods thick graded n-doping region. This is followed by a 200 periods thick non-intentionally doped (n.i.d) 8 ML InAs/8 ML GaSb T2SL absorber region, followed by p-type graded doping region, 40 periods, of 8 ML InAs/8 ML GaSb T2SL. The topmost layer was 50nm thick Be doped GaSb P contact layer (p = 2.8×10^{18} cm^{-3}). It is to be noted that our aim was to study the impact of interfaces on detector performance rather that to design high performance detectors, hence simple homojunction PIN detectors were fabricated for study instead heterojunction photodiodes.

The normalized spectral response data for three detectors is shown in Fig. 11 (77K, at a reverse bias voltage of 50mV). The 50% cutoff wavelength (λ_c) for structures (A), (D) and (E) was 4.2µm, 3.8µm and 4.1µm, respectively. Structure (A) contains InSb layer for strain compensation which results in higher cutoff wavelength, while structure (D) totally relies on soak time and growth interruption to achieve strain compensation and hence has the smallest λ_c.

Radiometric characterization of the detectors has been performed using a calibrated blackbody source at 900K, and a 2.5µm long pass filter (LPF). Spectral peak responsivity and detectivity as a function of temperature has been shown in Fig. 12. The noise measurements for detectivity were carried out with 2π field of view (FOV) and 300K background.

It can be seen that the responsivity is highest for structure (A), but very close to that of structure (E) which surpasses structure (A) at 200K, and is the least for structure (D). Measured detectivity is maximum for structure (D) at 77K and 100K, however it becomes comparable to that of structure (E) at higher temperature (above 150K), while structure (A) has the least detectivity at all the temperatures. The lowest detectivity in structure (A), in spite of high responsivity, is due to higher noise compared to structures (D) and (E). We attribute this to increased interface scattering with respect to other structures which leads to high non-radiative recombination rate. This corroborates well with PL data of structure (A) had the least intensity of all the samples while the intensity of structure (E) became comparable to that of structure (D) at higher temperatures. Structure (E) has higher detectivity than structure (A) and higher responsivity and comparable detectivity to structure (D).

Figure 12. Temperature dependent measured peak detectivity comparison of detectors with (A), (D), and (E) interface bonds measurement at 2π FOV and 300K background [N. Gautam, PhD Thesis, 2012]

(a) (b)

Figure 13. (a) TEM and (b) HRTEM images of MWIR T2SL grown on GaSb substrate with optimized growth conditions [Images by courtesy of Dr. S. J. Lee, KRISS]

Peak responsivity and detectivity of structure (E) at 77K, at reverse bias of 20mV, is 3A/W and 4.3×10^{10} Jones while peak responsivity and detectivity at 200K were 2.2A/W and 6.7×10^{8} Jones, respectively. Thus, during this interface study, we found that promoting "InSb" type bonds at both the interfaces of T2SL improves the optical quality of material and signal to noise ratio at high operating temperatures as compared to structures with one uncontrolled interface. Use of InSb layer at tensile interface and use of Sb_2 soak time at compressive interface is optimal in terms of material optical quality, device performance and growth time.

DISTRIBUTION A: Distribution approved for public release.

Quality of MWIR T2SL structures growth with optimized interfaces is confirmed by transmission electron microscopy (TEM) measurements, as illustrated in Figure 13.

3.2.2. Optimization of Growth Conditions in LWIR T2SL structures

We performed systematic study to select the best interface structure for LWIR ($\lambda_{100\%}$ ~ 8-12μm) T2SL, with the detector performance being the ultimate benchmark for the interface quality [30, 31]. The thickness of InAs layer in LWIR T2SL stack is typically exceeds that of the GaSb layer in order to shift the highest valence miniband upwards and realize the T2SL with smaller bandgap. InAs has a smaller lattice parameter than GaSb and it is therefore necessary to compensate the net strain in T2SL stack by adding a material with a larger lattice constant than GaSb. Only two III-V binaries satisfy this condition, AlSb (0.66% lattice mismatched with GaSb) and InSb (6.29% lattice mismatched with GaSb). AlSb has an absolute mismatch almost equivalent to that of InAs, and therefore, it would require a number of AlSb MLs equals to that of InAs to compensate the T2SL strain. But it is also a very large band-gap material (2.3 eV) that would decrease dramatically the cut-off wavelength of the T2SL. With this being said, an "InSb" type of interface is desired in LWIR T2S to suppress the natural tensile strain of the InAs layer on the GaSb- layer. InSb interface may be promoted either by intended insertion of thin InSb layer after GaSb in T2SL stack or by forming InSb interfaces on the InAs layers using a Sb soak that enabled preferential group V exchange on the growth front.

We grew two set of samples with 60 periods of T2SL with the same composition (13 MLs InAs/ 7 MLs GaSb) and enforced InSb interface. In a first set InSb interface was intentionally grown after GaSb layers in every T2SL periods and in the second set the InSb interface was formed by applying of Sb-soak time after InAs layers. The crystalline quality of grown material was assessed by high-resolution x-ray diffraction (HRXRD) performed with a Philips double-crystal X-ray diffractometer using the Cu-$K_{\alpha1}$ line measurements. Comparison of full width at half maximum (FWHM) of 1st satellite T2SL peak, lattice mismatch between T2SL and GaSb substrate, and T2SL period thickness for both sets is shown in Fig. 14.

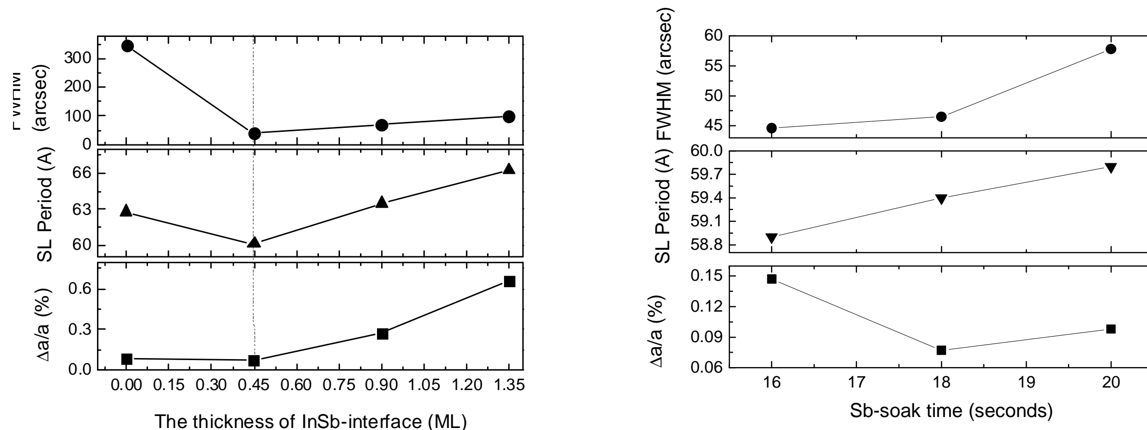

Figure 14. Comparison of full width at half maximum (FWHM) of 1st satellite T2SL peak, lattice mismatch between T2SL and GaSb substrate, and T2SL period thickness for the LWIR InAs/GaSb T2SL samples with InSb interface (a) intentionally grown after GaSb layers and (b) formed by applying of Sb-soak time after InAs layers [Plis et al, Proc. SPIE, 2011]

The best structural properties were demonstrated by the sample with 0.45 ML of InSb intentionally grown after GaSb constituent layer and 18 sec of S-soak time applied after the InAs constituent layer. Since with the same thickness of LWIR T2SL constituent layers the additional 18 sec of Sb time in every T2SL period would lead to a significant increase of total growth time, we utilized the other approach (growth of InSb thin layer in every T2SL period) for further studies. Next, we investigated the dependence of LWIR T2SL structural, optical, and electrical quality on flux ratios of Sb/ Ga and As/In BEPs. Set of three LWIR T2SL detector samples was grown with fixed flux ratio of Sb and Ga BEPs ($F_{Sb/Ga}$ = 3.8) and $F_{As/In}$ varied as 5.5, 6, and 7, supplemented by other set of LWIR T2SL detectors grown with fixed flux ratio of As and In BEPs ($F_{In/As}$ = 6) and $F_{Sb/Ga}$ varied as 3.2 and 3.8. All investigated detectors had the same structure, formed by 225 periods of 14 ML InAs/7 ML GaSb T2SL non-intentionally doped absorbing region grown on top of 75 periods of n-type (n = 4 x 10^{18} cm^{-3}) T2SL with the same composition and capped by 100 nm of GaSb p-type (p = 4 x 10^{18} cm^{-3}) layer. The top and bottom 25 T2SL periods

DISTRIBUTION A: Distribution approved for public release.

of absorbing layer were doped p-and n-type, respectively, in order to improve transport of photogenerated carriers. Due to the same purpose, doping level was gradually changed from p = 1 x 10^{16} cm^{-3} to 4 x $10^{18}$$cm^{-3}$ in the top 25 periods of absorbing region.

Device performance has been evaluated Spectral response measurements were performed with Fourier transform IR spectrometer (FTIR) equipped with glow-bar black body source (Fig. 15).

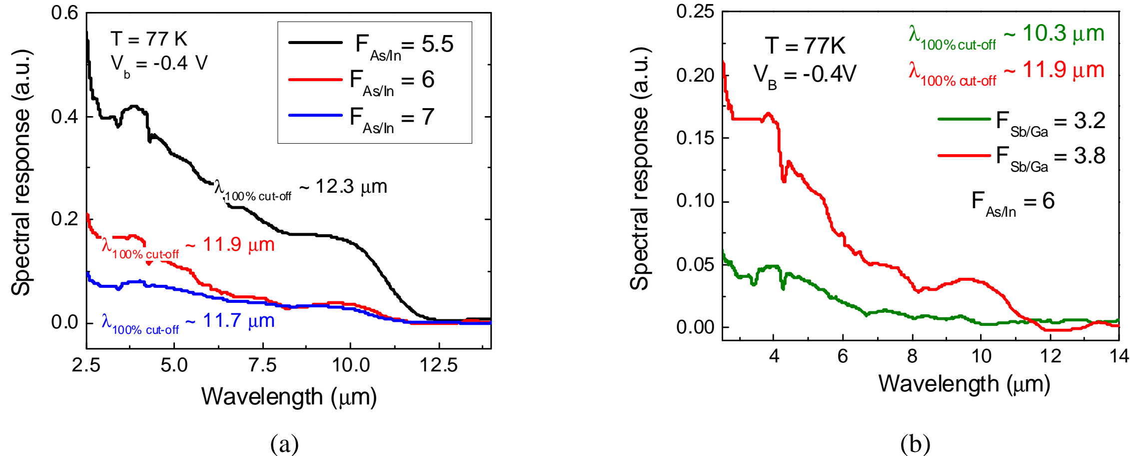

(a) (b)

Figure 15. Spectral response measured at 77K and -0.4V for LWIR T2SL detector samples grown with (a) fixed flux ratio of Sb and Ga BEPs ($F_{Sb/Ga}$ = 3.8) and $F_{As/In}$ equal to 5.5, 6, and 7 and (b) with fixed flux ratio of As and In BEPs ($F_{In/As}$ = 6) and $F_{Sb/Ga}$ varied as 3.2 and 3.8. [Plis et al, Proc. SPIE, 2011]

It should be noted that presence of excessive amount of As during InAs/GaSb T2SL growth ($F_{As/In}$ = 7) would possibly lead to formation of GaAs interfacial layer due to interdiffusion of As into GaSb layers. Similarly, reduced amount of As during the growth of T2SL stack ($F_{As/In}$ = 5.5) would favor to formation of InSb-like interfacial layer. Different thicknesses of GaAs-and InSb-like interfacial layers in every T2SL period will alter T2SL cut-off wavelength. In particular, the excessive formation of GaA-like interfacial layer would cause blue shift of T2SL cut-off wavelength, whereas the thick InSb-like interfacial layer will shift T2SL cut-off wavelength towards longer wavelengths, as observed from spectra in Fig. 15 (a). In a similar manner, sample grown with excessive amount of Sb ($F_{Sb/Ga}$ = 3.8) would demonstrate the longer cut-off wavelength as evident form Fig. 15 (b).

Dark current density as a function of applied bias has been measured at different temperatures for both sets of LWIR T2SL samples (Fig. 16). We attribute larger dark current observed in detector structure grown with excess of As to the increased roughness of interfaces and presence of impurities/vacancies acting as a scattering centers. Best electrical performance have been demonstrated by detector structure grown with $F_{As/In}$ = 6 and $F_{Sb/Ga}$ = 3.2.

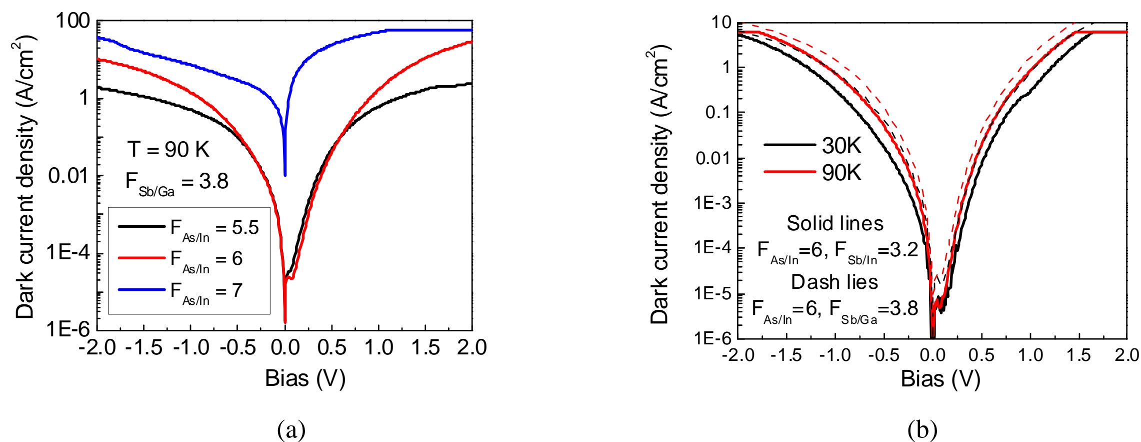

(a) (b)

DISTRIBUTION A: Distribution approved for public release.

Figure 16**.** Dark current density as a function of applied bias for LWIR T2SL detector samples grown with (a) fixed flux ratio of Sb and Ga BEPs ($F_{Sb/Ga}$ = 3.8) and $F_{As/In}$ equal to 5.5, 6, and 7 and (b) with fixed flux ratio of As and In BEPs ($F_{In/As}$ = 6) and $F_{Sb/Ga}$ varied as 3.2 and 3.8. [Plis et al, Proc. SPIE, 2011]

3.2.3. Photocapacitance Study of T2SL Defect Levels

Recently, Sanjay Krishna's group used photocapacitance measurements to study defect levels in superlattice and GaSb. While GaSb has been previously studied for defects, the effects of its use in T2SL have rarely been. Two key differences between bulk GaSb and GaSb in T2SL are: 1) bulk GaSb is grown at much higher temperatures (500°C), compared to T2SL (400-440°C), and 2) there is intermixing of the In and As from the alternate layers with the GaSb. These differences could potentially contribute to the low lifetimes found in the Ga-containing superlattices. We used steady-state photocapacitance as a characterization method to show at what energy levels defects appear.

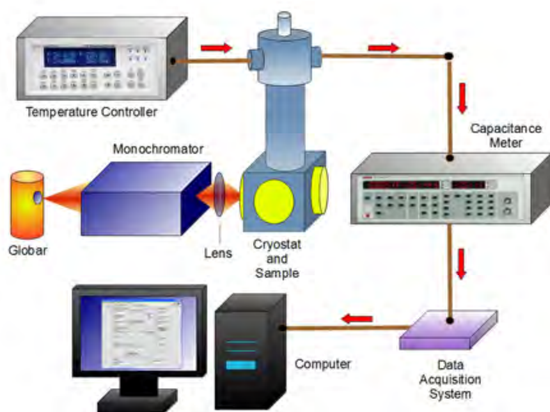

Figure 17. Diagram of photocapacitance setup. Light from the IR source gets focused into a monochromator with an off-axis parabolic mirror (not shown). The monochromator selects the wavelength of light to send out through the lens and to the sample in the cryostat [B. Klein, PhD thesis, 2014]

A diagram of the photocapacitance setup for this project is illustrated in Figure 17. A HawkEye IR-18 glow-bar with a maximum temperature of 1150°C and equipped with a parabolic reflector is the broad-spectrum IR source. This light is focused onto the input slit of the monochromator (CM110 1/8-meter) by an off-axis parabolic mirror (not shown in diagram), the monochromator's internal diffraction grating is used to select an output wavelength which is then directed out of the monochromator. This light is focused by a KBr lens onto the sample under test held within the cryostat (Janis VPF-100). Temperature control was achieved with a LakeShore 330 temperature controller. A capacitance meter (Agilent 4263 LCR meter) is connected to the sample by electrical throughputs; the meter records the capacitance of the sample as the incident wavelength is varied. These values are sent to a computer via GPIB and the data is saved.

Each photocapacitance data set was taken using the same method. First, the sample was cooled in the cryostat to the desired temperature and allowed to stabilize for a minimum of half an hour. Then, the sample was connected to the capacitance meter by a 4-point probe configuration. Light from the IR source and monochromator combination was directed onto the sample, and the sample was carefully positioned by a 3-dimensional linear translation stage to maximize the change in capacitance between when light was allowed on it and when light was blocked. To condition the sample prior to every run, any hole traps were filled by briefly shining above-bandgap light on the sample. Then, the photocapacitance data was collected, starting with the lowest energy (highest wavelength) and scanning to the highest energy (lowest wavelength) of interest, while the capacitance of the sample was monitored. At each wavelength, the sample was allowed a settling time before capacitance data was collected. The capacitance data from each wavelength was measured by collecting several data points and averaging.

Table 1. Photocapacitance samples

#	Sample	Growth Temperature
1	GaSb	400
2	GaSb : In	400
3	GaSb : As	400
4	GaSb	500

Samples 1-3 in **Table 1** were grown to see if any defects, observable through photocapacitance measurements, were formed in GaSb through doping by In and As. Since these atoms constitute the layers above and below each GaSb layer, they are very likely to mix into the GaSb. Each of these samples was grown on undoped (residually p-

DISTRIBUTION A: Distribution approved for public release.

type) GaSb epi-ready, double-side polished (100)-oriented substrates, at the T2SL growth temperature (≈400°C). The epitaxy was approximately 4 μm-thick for all three devices, and was fabricated into Schottky diodes. Sample 1 was an undoped GaSb control, sample 2 was GaSb incorporated with 1.2% In, and sample 3 was incorporated with 2.2% As by opening the valve to 200 mils but growing with the As shutter closed. Incorporation levels were confirmed by overlaying the x-ray diffraction (XRD) data from each sample with simulated XRD from RADS Mercury simulation software.

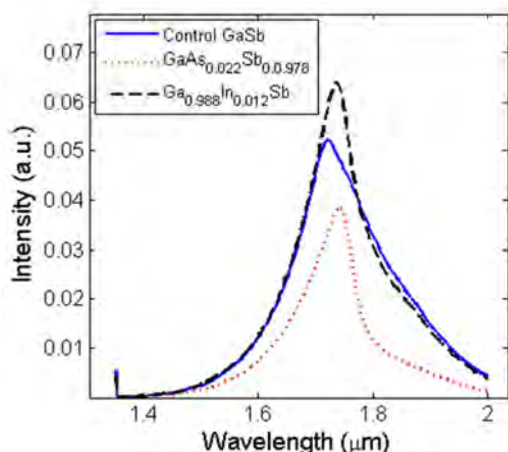

Figure 18. Photoluminescence of the incorporation samples at room temperature**.** [B. Klein, PhD thesis, 2014]

Photoluminescence plots of these three samples are given in figure 18. The addition of In actually increased the PL intensity compared to the control sample, while As reduced it. The control sample's intensity was 80% of the GaInSb samples', and the GaAsSb sample's intensity was 60% of the GaInSb samples'. The stronger PL of the In-incorporated sample is expected; a previous study[32] had shown increasing lifetime in $InAs/In_xGa_{1-x}Sb$ superlattices with increasing In content. The reduced PL intensity of the GaAsSb sample may support why growers promote InSb-like interfaces rather than GaAs-like ones. Degrading PL intensity may coincide with reduced sample performance for T2SL grown with GaAs-like interfaces.

Two features appear in the photocapacitance plots for all of the samples, labeled as features A and B. Feature A begins at approximately 0.5 eV with a maximum at about 0.6 eV and feature B is at approximately 0.8 eV.

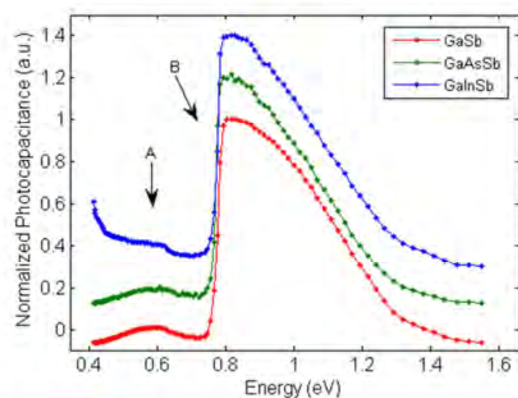

Figure 19. Photocapacitance results for GaSb with As, In, and a control. Data is stacked for easier comparison. [B. Klein, PhD thesis, 2014]

Because the bandgap of GaSb is calculated to be 0.8 eV at 77 K[33], feature B can be attributed to transitions from traps slightly above the valence band edge to the conduction band. Feature A is near mid-gap, and appears regardless of whether the material is pure GaSb, or alloyed with In or As, suggesting that it is intrinsic to GaSb. These results appear to confirm the presence of a GaSb trap feature at 0.63eV first reported by Kuramochi[34]. They had attributed this trap to Te diffused into the GaSb from the Te-doped substrate. Te is likely not the cause of this level in the photocapacitance results, since Te was not intentionally put into the structure and the substrates were undoped.

However, it could still be present in the background levels of the growth chamber and cannot be completely ruled out. The change in capacitance of feature A is smaller for the sample with In incorporation. This may indicate a reduction in the trap density for this sample.

Our next task was to find out if any change in defect levels due to different growth temperatures could be detected through photocapacitance measurements. For this study, a GaSb sample (sample 1) grown at T2SL growth temperature 400°C and one at 500°C (optimal GaSb growth temperature, sample 4) were fabricated into Schottky diodes and their photocapacitance spectra were measured with 2.4 mm monochromator slits and a 1 V applied reverse bias. The results are shown in figure 20, which shows that the peak normally observed at 0.5 eV for the samples grown at T2SL temperature is much smaller in sample 4. This plot looks very similar to the GaInSb photocapacitance result in figure 19. The reduced change in capacitance of this feature may suggest that the trap level seen in sample 1 has changed for sample 4. However, there is still a feature present, even for the sample with

DISTRIBUTION A: Distribution approved for public release.

increased the growth temperature.

Photoluminescence measurements were conducted on these samples as well, with room-temperature results plotted in figure 21. The GaSb grown at 500°C does have a slightly higher intensity, 1.3 times that of the sample grown at ~400 °C. This suggests that there might be a slight improvement in GaSb quality with higher temperatures, though this difference is small enough that it could be within the variation of the PL intensity across the sample.

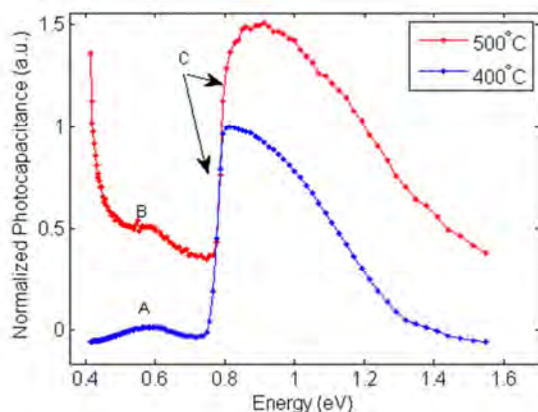

Figure 20. Photocapacitance spectrum comparison for GaSb grown at 400°C and 500°C. These plots are stacked for easier comparison. [B. Klein, PhD thesis, 2014]

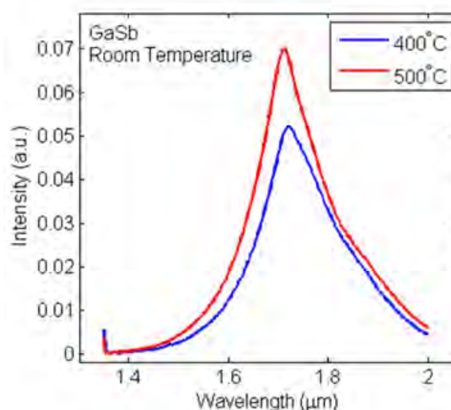

Figure 21. Room-temperature photoluminescence comparison for GaSb grown at 400° C and 500°C. [B. Klein, PhD thesis, 2014]

3.2.4. Vertical mobility in InAs/GaSb superlattices

In collaboration with Prof. Laurie Faraone's group in University of Western Australia, Sanjay Krishna's group reported the results of an experimental study of the vertical carrier mobility in InAs/GaSb T2SL using variable magnetic field geometric magneto-resistance measurements and a mobility spectrum analysis (MSA) technique for data analysis[35,36,37]. This procedure makes it possible to determine the vertical mobility and the concentration of individual carriers contributing to the conductivity. Using this approach, it is found that at 300 K, there are four carriers present, which can be attributed to majority holes, two species of minority bulk-electrons and side-wall inversion-layer electrons. It is also found that the background concentration of holes contributing to the transport at T=80 K, the temperature at which most T2SL diodes are operated, is about $3x10^{14}$ cm^3 in agreement with reported CV measurements. The contribution of the sidewall electrons to the total conductivity (≈37%) is consistent with the results obtained from variable area devices at room temperature.14 The influence of this parasitic sidewall inversion layer increases at lower temperatures (≈47% at 80 K) thus stressing the importance of developing high-quality surface passivation schemes for small area T2SL-based diodes.

The InAs/GaSb T2SL structure used in this study consisted of a lightly p-type (p) doped superlattice layer, with 14 ML InAs and 7ML GaSb, sandwiched between two P-doped superlattice layers. All measurements were performed in a vertical $P^+/\pi/P^+$ homojunction configuration that mimics the architecture of a T2SL diode with the p-doped layer corresponding to the absorber region of a photodiode detector. The samples were grown in a VG semicon V-80H molecular beam epitaxy system on a Te-doped (100) GaSb substrate. The top and bottom heavily p-type Be-doped (Pþ : 2e18cm^3) layers act as SL ohmic contacts to the 2.025 µm thick lightly p-type Be-doped region (p : 1e16cm^3) composed of 300 periods each consisting of 14 ML InAs and 7 ML of GaSb. The composition and doping of the p region are similar to the absorber region that is typically used in LWIR detectors in this material system. The sample was processed into 410x410 μm^2 test-structures, topologically similar to normal incidence single pixel photodiodes, with mesas formed by BCl3-based dry- etching. Following Ohmic contact metallization, the mesa side- walls were passivated with SU-8 film. However, parasitic sidewall leakage was found to be significant at 300 K. Figure 22 shows the detailed heterostructure schematic of the fabricated device and the four-wire Kelvin mode magneto-resistance measurement set up.

The current-voltage characteristics (IV) were found to be Ohmic for all temperatures and all magnetic field intensities employed (61 values from 12T to 12 T). Hence the geometrical magneto-resistance was obtained

DISTRIBUTION A: Distribution approved for public release.

from the dynamic resistance of the IV characteristics (dV/dI) for applied voltages between -5mV and 5mV, equivalent to electric fields below 25 V/cm. Due to the relatively low sample resistance (1:71X at 300 K), a four-contact Kelvin set-up was employed to minimize the influence of parasitic series resistance, as described in Ref. 14. Although all measurements were undertaken in the linear IV regime, the measured magneto-resistance characteristics departed significantly from those expected for the case of a single discrete carrier. According to the relation, $R(B) = R(0)(1 + \mu^2 B^2)$ where R(B) is the resistivity at magnetic field intensity B and l is the carrier mobility, a plot of R(B)/ R(0) versus B^2 is linear if a single carrier species is present.

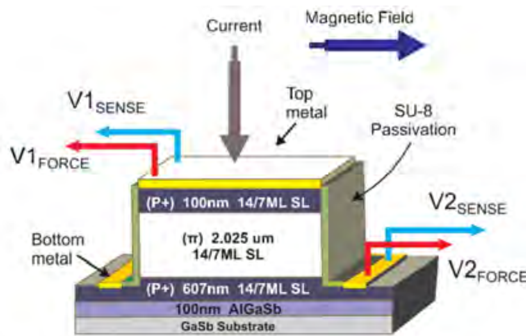

Figure 22. Four-point probing configuration for single pixel structures [Umana-Membreno et al, APL 101, 235515, 2012]

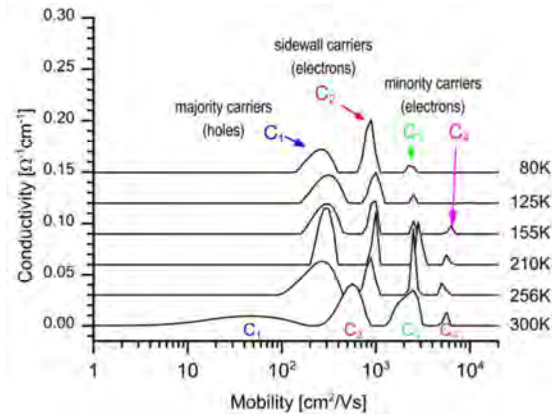

Figure 23. Mobility spectra for selected temperatures from 80 to 300 K. Each conductivity peak represents a single carrier species [Umana-Membreno et al, APL 101, 235515, 2012]

The extracted mobility spectra for all temperatures are presented in Fig. 23, in which each conductivity peak in a given spectrum corresponds to a single carrier species. Thus, the four distinct conductivity peaks evident at 300K correspond to four distinct carriers, each with a well-defined mobility distribution. In contrast, only the peaks labelled C1; C2, and C3 were detectable at 80K. The concentration n_i and mobility μ_i for the carrier species represented by the ith conductivity peak in the spectrum were obtained.

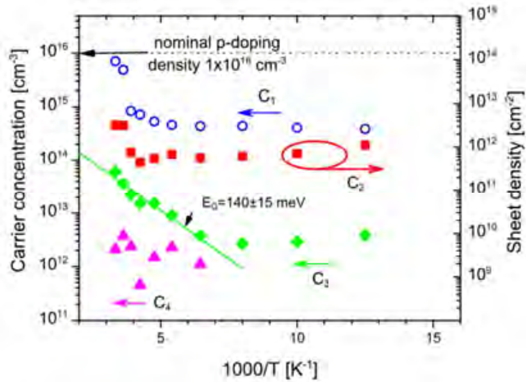

Figure 24. Carrier concentrations extracted from the spectra in Fig. 23. The density of the C2 carriers, interpreted as sidewall inversion layer electrons, is referred to the right-hand scale as a sheet density [Umana-Membreno et al, APL 101, 235515, 2012]

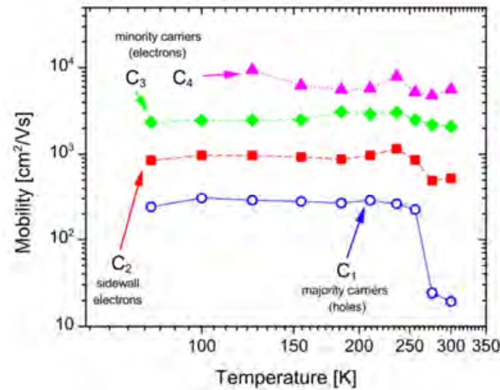

Figure 25. Individual carrier mobilities extracted from the spectra in Fig. 23. [Umana-Membreno et al, APL 101, 235515, 2012]

The extracted n_i and μ_i values for all carriers in the spectra of Fig. 23 are summarized in Figs. 24 and 25, respectively. Here, the extracted carrier concentration n_i is the effective concentration of carriers contributing to conductivity along the superlattice's growth direction (vertical conductivity). It should also be noted that, in contrast to traditional lateral Hall-effect measurements in which the carrier type is discerned from the sign of the Hall-coefficient, the carrier type cannot be discriminated from vertical magneto-resistance measurements since the

DISTRIBUTION A: Distribution approved for public release.

Hall voltage is effectively zero. Thus, the assignment of carrier type, and physical origin, needs to take into account known physical characteristics of the sample, such as intentional doping density and impurity type, as well as the temperature dependence of the experimentally extracted mobilities and concentrations. The carrier assignments shown in Figs. 24 and 25 arise from the following considerations: (a) For T¼300 K, the concentration of the lowest mobility C1 peak is consistent with low mobility holes and with the nominal intentional acceptor doping, thus this conductivity peak is interpreted as corresponding to the majority-carrier holes; (b) the C2 peak exhibited a nearly temperature-independent carrier sheet concentration and mobility, similar to the parasitic electron accumulation and/or inversion layers commonly found in narrow-bandgap materials such as HgCdTe, and a conductivity contribution that was consistent with variable area device analysis, thus it has been interpreted as arising from electrons forming an inversion layer at the test-structure sidewalls; and (c) the high mobility peaks labelled C3 and C4 are interpreted as minority carrier electrons arising from distinct energy levels in the T2SL conduction band.

In summary, a study of vertical carrier transport in InAs/GaSb T2SL employing geometrical magneto-resistance measurements and high-resolution mobility spectrum analysis has enabled the extraction of the individual transport parameters of the carriers present in a lightly p-type doped InAs/GaSb type-II superlattice sample. From 80 to 155 K, the conductivity was found to be dominated by three distinct carriers attributed to majority holes, minority electrons, and parasitic sidewall inversion layer electrons. Over this temperature range, which corresponds to the typical operational temperature range of LWIR photodetectors, the minority electron mobility was found to be 2460675cm2=Vs and approximately temperature independent. A superlattice energy gap of 140meV was estimated from the thermal activation of the minority carriers for T > 155K.

3.2.5 Carrier Lifetime Studies in InAs/GaSb MWIR T2SLs

Recently, Dr. Krishna's group at UNM has investigated the dependence of the minority carrier lifetime in MWIR T2SLs on a number of varied parameters: layer placement of two dopants (either Be or Te), and interface treatment between InAs and GaSb layers [38].

Growth was performed using a solid-source VG-80 molecular beam epitaxy (MBE) system with valved As_2 and Sb_2 crackers. All samples possessed the same base architecture, with the only variations in sample growth in the 2-µm thick 8 monolayer (ML) InAs / 8 ML GaSb T2SL test region. An 8/8 T2SL configuration was chosen due to a desired cutoff wavelength in the MWIR (~4.5 µm) and the even number of monolayers for InAs and GaSb, which enabled a more consistent comparison in the doping study. On either side of the T2SL were 10 nm AlSb barriers to contain optically-injected carriers to the T2SL region and prevent surface recombination. The GaSb capping layer was grown to prevent oxidation of the AlSb layer.

To determine the effect of the doping placement in the T2SL constituent layers seven samples (A-G) were grown. The top half of **Table 2** outlines the placement of doping for a single superlattice period. Te and Be were used as n- and p-type dopants, respectively. To ensure that the doping level would be as similar as possible in both T2SL constituent layers, the Ga and In growth rates were held at the same rate, 0.48 ML/s.

The top half of Table 3 provides a summary of the interface study. The first column defines each layer constituting of a single T2SL period, in growth order from top to bottom. Each subsequent column represents one of the three samples grown for this experiment. Interface A, the interface between InAs and GaSb, consisted of either no controlled interface or a 0.6-s Sb soak. Interface B, the interface between GaSb and the subsequent InAs layer, had either an InSb strain compensation layer or a 1-second growth interrupt.

The carrier lifetimes were determined using time-resolved photolumimescence (TRPL) measurements. Samples were temperature controlled from 8 – 300 K using closed-cycle helium cryostat, and pumped with a 2-µm laser with ~100-fs pulse width and 250-kHz repetition rate. Off-axis parabolic mirrors were employed to collect the photoluminescence, and focus the PL onto a fast HgCdTe detector (1 mm x 1 mm, 3-ns temporal response, 200 K operating temperature). A 3.6-µm longpass filter was used to isolate the PL signal from scattered laser light. The detected signal was amplified and sent to a data acquisition system. A variety of pump laser intensities we used, corresponding to different initial excess carrier densities of 7.3 x 10^{16}, 3.6 x 10^{16}, 2.1 x 10^{16}, 1.1 x 10^{16}, 5.5 x 10^{15}, 3.1 x 10^{15}, 1.6 x 10^{15}, 1.0 x 10^{15}, 5.1 x 10^{14} cm^{-3}.

Table 2. Summary of doping placement study. Low injection is defined by injection levels from 1 to 5 x 10^{15} cm^{-3} and high injection is defined as an injection level of 7.3 x 10^{16} cm^{-3}.

Table 3. Summary of interface treatment study. Low injection is defined by injection levels from 1.6 x 10^{15} to 2.1 x 10^{16} cm^{-3} and high injection is defined as an injection level of 7.3 x 10^{16} cm^{-3}.

DISTRIBUTION A: Distribution approved for public release.

Layer		Samples						
		A	B	C	D	E	F	G
InAs		NID	Te	NID	Te	Be	NID	Be
GaSb		NID	NID	Te	Te	NID	Be	Be
	T, K	Lifetime (ns)						
Low Injection	8	49.4	3.1	< 3	8	12.2	11.7	12.8
	77	48.5	< 3	< 3	77	14.8	11.6	9.4
	300	47.9	NA	NA	300	44	34.3	33
High Injection	8	37.7	13.9	8.4	< 3	35.4	33.6	29.1
	77	36.3	16.2	8.4	3.1	38.2	34.7	29.7
	300	39.2	NA	NA	NA	38.9	37.2	31.6

Layer		Sample 1	Sample 2	Sample 3
InAs				
Interface A		Uncontrolled	Sb Soak	Sb Soak
GaSb				
Interface B		InSb Strain Compensation	Growth Interrupt	InSb Strain Compensation
	T, K	Lifetime (ns)		
Low Injection	8	47.1	31.5	49.4
	77	48	36.4	48.5
	300	44	42.8	47.9
High Injection	8	36.5	30.9	37.7
	77	29.8	31.3	36.3
	300	36.5	34.8	39.2

A representative plot of the TRPL data over a temperature range of 8 to 300 K is shown in Fig. 26 for Sample 2. The carrier lifetime was extracted from the TRPL data using the equations for a single exponential decay: $S_{PL} = S_{t=0} e^{-t/\tau}$, where S_{PL} is the time-dependent PL intensity, $S_{t=0}$ is the PL intensity at time zero, t is time, and τ is carrier lifetime. This treatment assumes that the low-injection limit has been reached in order to determine the minority carrier lifetime.

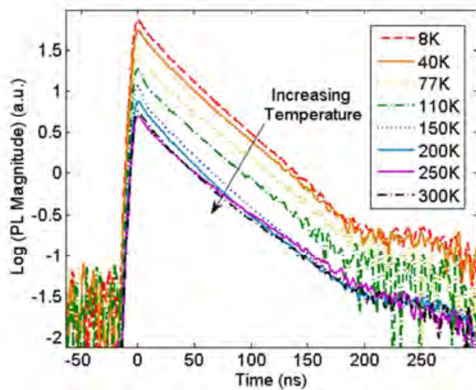

Figure 26. Representative TRPL plot from 8 – 300 K [Klein et al, JVST B 32, 02C101, 2014]

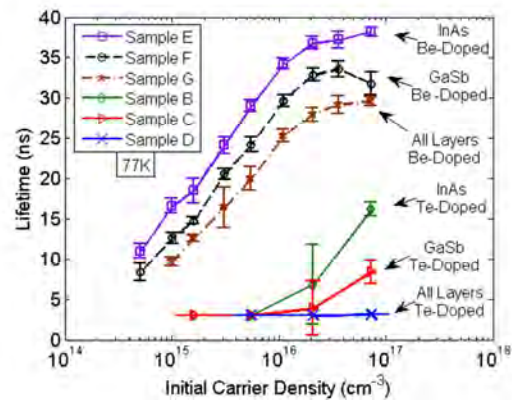

Figure 27. Lifetime as a function of initial carrier density fc doping study Samples B – E at 77 K. All of these sample exhibited trap saturation [Klein et al, JVST B 32, 02C10 2014].

The lower half of **Table 2** provides the measured PL lifetimes from TRPL at 8 K, 77 K, and 300 K, for both low (1 – 5x10^{15} cm^{-3}) and high injection conditions (7.3x10^{16} cm^{-3}). Fig. 27 shows the lifetime's dependency on initial carrier injection at 77 K for the Te- and Be-doped samples B – G. Error bars were calculated by taking the difference of the integrated intensity of the PL decay and the integrated intensity of the fit. The lower half of **Table 3** summarizes the measured lifetimes of the samples that investigate the effect of varying the interface treatment at both low (1.6x10^{15} to 2.1x10^{16} cm^{-3}) and high injection (7.3 x 10^{16} cm^{-3}) for temperatures of 8 K, 77 K, and 300 K. Fig. 28 presents lifetime as a function of initial excess carrier density for the interface study Samples 1-3 at 77 K. Sample 3 had the longest lifetimes.

DISTRIBUTION A: Distribution approved for public release.

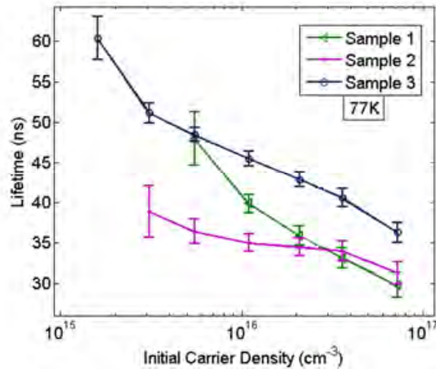

Figure 28. Lifetime as a function of initial excess carrier density for interface study. [Klein et al, JVST B 32, 02C101, 2014]

Trap saturation, which is observed as an intensity-dependent behavior in the TRPL decay, where the lifetime increases with increased carrier injection, was observed in both the Te- and Be-doped samples. It appears that the sample with the InAs layer doped had longer lifetimes than the samples where the GaSb layer was doped, or the samples where both layers were doped. This trend is also seen in the high-injection data of the Te-doped samples. Moreover, it was found that the growth sequence that resulted in the longest observed lifetime consists of, in order, an InAs layer, Sb soak, GaSb layer, and InSb strain compensation layer.

3.2.6. InAs/InAsSb SL Structures for Improved Carrier Lifetime

The SRH generation-recombination process occurs through the trap levels within the energy bandgap. The statistical theory of SRH process states the SRH rate approaches a maximum as the energy level of the trap center approaches midgap. Thus, the most effective SRH centers are those located near the middle of the bandgap [39]. Analysis of the defect formation energy of native defects dependent on the location of the Fermi level stabilization energy has been performed by Walukiewicz [40]. He found that in bulk GaAs and GaSb the stabilized Fermi level locates near the valence band or the midgap, whereas in bulk InAs the stabilized Fermi level locates above the conduction band edge. This observation leaves the mid-gap trap levels in GaAs and GaSb available for SRH recombination whereas in InAs they are inactive for SRH process, suggesting the shorter carrier lifetime in bulk GaSb and GaAs materials. Indeed, the experimentally measured values of carrier lifetimes yielded in ~ 325ns for the bulk InAs and ~ 100ns for the bulk GaSb [41]. We may hypostatize now that a native defects associated with the GaSb is responsible for the SRH limited minority carrier lifetime in InAs/GaSb T2SL.

To overcome the carrier lifetime limitations imposed by GaSb layer in InAs/GaSb T2SL, we suggest to use type-II "Ga-free" T2SL, i.e. InAs/InAsSb T2SL. It should be noted that measured value of bulk $InAs_{0.2}Sb_{0.8}$ material was ~250ns [42], that is still higher than that of bulk GaSb, thus making InAs/InAsSb T2SL approach for realization of high performance infrared detector feasible.

First, we model the electronic band structure of the $InAs/InAs_xSb_{1-x}$ SL (x = 0.65) in the growth-axis (z) direction as well as band alignment between InAs and $InAs_{0.65}Sb_{0.35}$ layers with with empirical pseudopotential method [43] (Fig. 29). The simulation resulted in an effective SL bandgap, which is separation between C1-HH1 minibands, of ~0.28eV (77K). Since simulation does not take into account interfaces between SL layers, the SL bandgap is underestimated. Nevertheless, this simulation gives a good estimation of the bandgap and bandoffsets in type-II InAs/ $InAs_xSb_{1-x}$ SL system, especially for designing heterostructures.

Figure 29. Band structure simulation of 14MLs InAs /

Figure 30. (a) HRXRD and (b) room-temperature PL

DISTRIBUTION A: Distribution approved for public release.

12 ML $InAs_xSb_{1-x}$ (x = 0.65). Inset shows band line up of InAs/InAsSb SL with the same layer composition and thicknesses [Schuler-Sandy et al, Appl. Phys. Lett. 101, 071111, 2012]

spectra of InAs/ $InAs_{0.35}Sb_{0.65}$ SL detector material. [Schuler-Sandy et al, Appl. Phys. Lett. 101, 071111, 2012]

Then a homojunction p-i-n architecture was designed with an absorber region composed of a ~ 1µm thick 14 monolayers (MLs) InAs / 12 MLs $InAs_xSb_{1-x}$ (x = 0.65) SL (130 periods) grown on top of a ~ 0.5µm thick n-type (4 x 10^{18} cm^{-3}) contact layer (composed of SL with the same composition and thickness but with Te-doped layers). The structure was capped with a p-type (Be-doped, p~ 4 x 10^{18} cm^{-3}) ~ 80 nm thick top contact layer with the same superlattice composition and thickness as the bottom contact layer. Thin (10 periods) layers with linearly graded doping were grown below and above the absorber region to enhance transport of photogenerated carriers between contacts. The structural quality of as-grown material was assessed by high-resolution x-ray diffraction (HRXRD) performed with a Philips double-crystal X-ray diffractometer using the Cu-$K_{\alpha 1}$ line. The overall period of the SL was equal to 79.1 Å, which closely corresponds to the designed value (80.3 Å). Room-temperature photoluminescence (PL) measurements were performed on the InAs/InAsSb SL material using a 514nm argon laser, InSb detector, calcium fluoride collection optics, a germanium filter, and a monochromator equipped with a grating rated for 2.6 to 6um. HRXRD and room-temperature PL spectra are shown in Fig. 30.

Devices 410µm x 410µm square mesas with apertures ranging from 25 to 300 µm were fabricated with standard optical photolithography, ICP etch, and e-beam metal deposition techniques. Ohmic contact were formed by Ti (500Å) / Pt (500Å) /Au (3000Å) for both top and bottom contact layers. Devices were passivated with a plasma enhanced chemical vapor deposition (PECVD) SiNx (~230nm thick) layer.

After device fabrication, temperature-dependent dark current measurements as well as spectral response measurements were performed. Results are presented in Figure 31 (a) and (b), respectively.

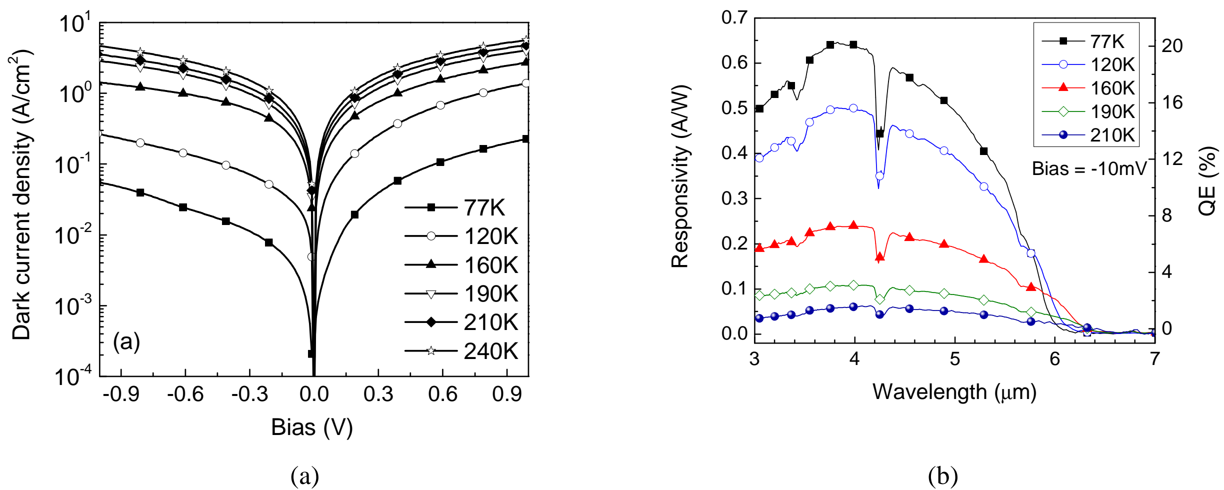

(a) (b)

Figure 31. (a) Current voltage characteristics of InAs/InAsSb SL detector measured at selected temperatures (b) Temperature dependent spectral response and quantum efficiencies under -10mV of applied bias measured with a Nicolet 670 Fourier transform infrared spectrometer. [Schuler-Sandy et al, Appl. Phys. Lett. 101, 071111, 2012]

The detector 50% cut-off wavelength was ~ 5.4µm at 77K. It should be noted that the photoresponse was clearly visible up to 210K. Under -10mV bias and 77K, the device exhibits peak a responsivity of 0.64 A/W corresponding to a QE of ~ 20%. In the case of a focal plane array configuration (with the substrate removed, the top metal contact acts as a mirror to ensure a double pass through the active region), and an adequate antireflection coating, the QE would reach about 50% at 4µm.

At 77K and operational bias of -10mV, the device exhibited dark current density of 2.1 x 10^{-4} A/cm^2, which is higher than dark current density demonstrated by state-of-the-art MWIR InAs/GaSb T2SL detectors with pin architecture [44]. The activation energy has been extracted from temperature-dependent dark current measurements, as shown in Fig. 32. The activation energy in the low temperature regime (60K-90K) was measured to be 8.5meV, which can be attributed to either tunneling or surface effects. A careful variable area diode study is needed to investigate the effect of surfaces in this low temperature regime. In the mid temperature range (100K-160K), an activation energy of 76meV~E_g/3 was observed.

DISTRIBUTION A: Distribution approved for public release.

Figure 32. The temperature-dependent dark current densities of InAs/InAsSb SL detector measured at -10mV of applied bias along with the calculated activation energies. [Schuler-Sandy et al, Appl. Phys. Lett. 101, 071111, 2012]

Since the SRH lifetimes in “Ga free” SL have been measured to be much longer compared to InAs/GaSb T2SL, the origin of Eg/3 states and their contribution to the dark current need further investigation. At higher temperatures (170K-240K), activation energy of 32meV has been measured. This is possibly due to the tunneling mechanism dominating the dark currents. In the InAs/InAsSb SL, the conduction (ΔE_C) and valence (ΔE_V) band offsets are much smaller (ΔE_C ~ 142 meV, ΔE_V~ 226 meV) as compared to InAs/GaSb T2SL (ΔE_C ~ 930 meV, ΔE_V~ 510 meV [45]). We believe that at higher temperatures as the carrier energy increases the probability of tunneling increases too, resulting in dark current dominated by a tunneling mechanism. We did not observe dark current dominated by the diffusion process as is the case in InAs/GaSb T2SL at higher temperatures.

In conclusion, after detailed electrical and optical characterization of a MWIR detector structure based on a InAs/ $InAs_xSb_{1-x}$ (x = 0.65) SL, we found that “Ga-free” detector performance was not superior compared to that of state-of-the-art MWIR detectors operating in a similar wavelength range. A strong possibility is an increased probability of carrier tunneling brought about by reduced valence and conduction band offsets in InAs/InAsSb SL systems. Further investigation is required before using the “Ga-free” SL system as an alternative to the conventional InAs/GaSb T2SL.

3.2.7. Growth on (111) GaSb to Improve the Hole Confinement and Operating Temperature

UNM also investigated different approach for the reduction of dark current in InAs/GaSb T2SL MWIR and LWIR detector structures. Since their original proposal for IR detection in 1970s [46], InAs/GaSb T2LS were almost exclusively grown on (100) GaSb substrates. However, use of (111)-oriented GaSb substrates for T2SL growth offers potentially better performance, with higher absorption and thinner layers as predicted by theoretical studies [4647]. Moreover, the large piezoelectric fields that occur in the (111) orientation in III-V materials lead to better hole confinement improving absorption with thin layers [48]. However, growth on high-index plane substrates such as (n11)-oriented GaSb substrates for InAs/GaSb T2SL structures has been associated with many growth challenges, in particular, facilitated defect formation and faceted growth in this direction [49]. During the review period we developed growth procedure and fabricated the mid-wave infrared ($\lambda_{100\%\ \text{cut-off}}$ ~ 5.6 μm at 300K) InAs/GaSb T2SL detectors grown on GaSb (111)B substrate.

All structures were grown on n-type (Te-doped) GaSb (111)B epi-ready substrates with 1.5° miscut towards (2 -1 -1) axis using solid source molecular beam epitaxy (MBE) in a VG-80H system equipped with cracker sources for group V (Sb_2 and As_2) and Ga/In SUMO® cells. Prior to detector growth, we optimized growth conditions of the GaSb smoothing layer on the GaSb (111)B substrate with respect to the substrate temperature and the Sb/Ga beam equivalent pressure (BEP) ratio in order to start the T2SL growth on a perfectly flat and defect free surface. A set of 0.5μm thick GaSb non-intentionally doped (n.i.d.) samples was grown on GaSb (111)B substrates. Fig. 33 presents the root mean square (RMS) roughness and integrated room temperature (RT) photoluminescence (PL) intensity measured for 0.5μm thick GaSb layers grown at different substrate temperatures. The maximized PL signal as well as the RMS roughness within two atomic monolayers (~ 0.5nm) has been achieved at a substrate temperature of 454°C.

DISTRIBUTION A: Distribution approved for public release.

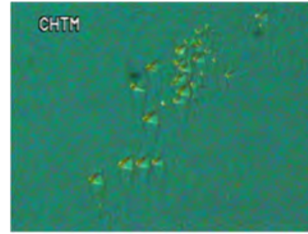

Figure 33. RMS roughness and integrated PL intensity measured for GaSb layers grown at different temperatures on GaSb (111) substrate. [Plis et al, J. Vac. Sci. Technol. B 31, 03C123, 2013]

Figure 34. Nomarski images taken from 0.5µm GaSb layer grown on (111)B GaSb substrate at optimized (454°C) (top) and selected non-optimal temperatures (bottom). [Plis et al, J. Vac. Sci. Technol. B 31, 03C123, 2013]

Fig. 34 presents the Nomarski images taken from 0.5µm GaSb layer grown on (111)B GaSb substrate at optimized (454°C) and one of non-optimal temperatures. Sample grown at optimized substrate temperature revealed a few pyramidal-shaped growth defects, whereas morphology of samples grown at non-optimal temperatures was similar to that shown in fig. 33 (bottom).

Next, morphology and optical quality of GaSb layers grown on (111)B GaSb substrate has been optimized with respect to Sb/Ga BEP ratio. The smooth, defect-free surface, along with the maximum integrated PL intensity was obtained for the sample grown at Sb/Ga BEPof approximately 6.7 (at growth temperature of 454°C).

After optimization of GaSb growth on GaSb (111)B substrate, the T2SL structures were realized. We grew 100 periods of T2SL in the sequence of [10 ML InAs/1s of growth interrupt/10 ML GaSb] for one T2SL period with a bandgap corresponding to the MWIR spectral region. The structural quality of as-grown material was assessed by high-resolution x-ray diffraction (HRXRD) performed with a Philips double-crystal X-ray diffractometer using the Cu-$K_{\alpha 1}$ line. Fig. 35 presents HRXRD spectrum of the T2SL grown on (111)B GaSb substrate (top) compared with HRXRD of T2SL the same composition grown on (100)GaSb substrate (bottom). In both cases, T2SL growth was optimized with respect to substrate temperature, As/In and Sb/Ga BEP ratios. Both T2SL samples demonstrated good structural quality, with comparable full width of half maximum (FWHM) of 1st order T2SL satellite peak (~ 40 arcsec), nearly zero lattice mismatch and symmetric T2SL satellite peaks implying the good quality of T2SL interfaces.

Figure 35. HRXRD spectra of the T2SL with the same composition grown on (111)B GaSb (top) and (100)GaSb (bottom) substrates. [Plis et al, J. Vac. Sci. Technol. B 31, 03C123, 2013]

The comparable quality of T2SL grown on (111)B and (100) GaSb substrates suggests that we fixed the optimal T2SL growth parameters for (111) GaSb orientation. The transmission electron microscopy (TEM) measurements were performed on both T2SL samples grown on (111)B GaSb and (100) GaSb substrates. Results are presented in Fig. 36.

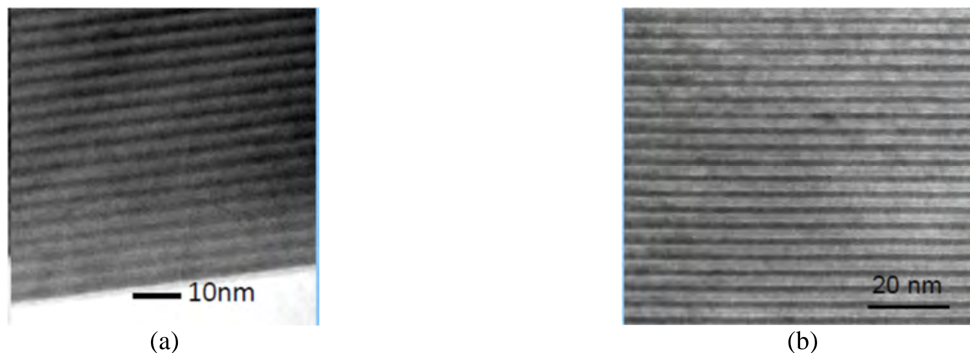

(a) (b)

Figure 36. TEM images of MWIR T2SL grown on GaSb substrates with (a) (111) and (b) (100) orientation [Plis et

DISTRIBUTION A: Distribution approved for public release.

al, J. Vac. Sci. Technol. B 31, 03C123, 2013]

Both T2SL samples demonstrated very good periodicity of the individual layers and abrupt interfaces, suggesting the good structural quality of grown T2SL material. Since the structural properties of T2SL grown on (111)B GaSb substrate is not substantially differ from those of T2sL grown on conventional substrate, we conclude that our growth optimization procedure was very successful.

A homojunction p-i-n architecture was designed with an absorber region composed by 300 periods of 6 monolayers (MLs) InAs / 7 MLs GaSb grown on top of a 150 period thick n-type (4 x 10^{18} cm^{-3}) contact layer (composed of T2SL with the same composition and thickness but with Te-doped InAs layers). The structure was terminated with a p-type (Be-doped, p~ 4 x 10^{18} cm^{-3}) ~ 100 nm thick GaSb top contact layer. Thin regions composed of the T2SL with the same composition with linearly graded doping were grown below and above the absorber region to enhance transport of photogenerated carriers between contacts. Room-temperature photoluminescence (PL) measurement, shown in Fig. 37, was performed on the T2SL detector material using a He-Ne laser with a power ~ 1W, InSb detector, germanium filter, and a monochromator equipped with a grating rated for 2.6 to 6um. Inset to Fig. 37 present the heterostructure schematic of p-i-n T2SL MWIR detector.

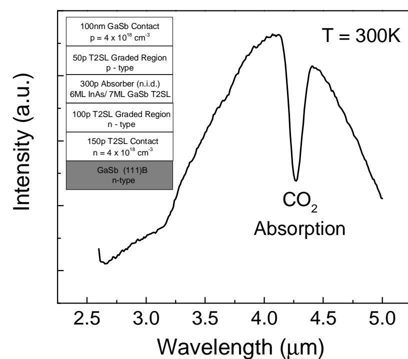

Figure 37. Room-temperature PL spectrum of MWIR T2SL detector material grown in GaSb (111)B substrate. The inset shows the heterostructure schematic of the T2SL detector. [Plis et al, J. Vac. Sci. Technol. B 31, 03C123, 2013]

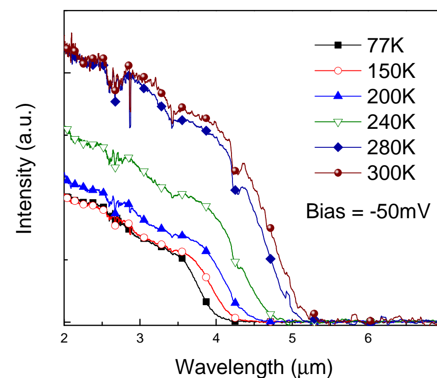

Figure 38. Temperature dependent spectral response under -50mV of applied bias measured with a Nicolet 670 Fourier transform infrared spectrometer. [Plis et al, J. Vac. Sci. Technol. B 31, 03C123, 2013]

Photodetectors were fabricated with standard optical photolithography to define 410μm x 410μm square mesa devices with apertures ranging from 25 to 300 μm. Etching was performed using an inductively coupled plasma (ICP) reactor with BCl_3 gas. The resulting etch depth was ~ 1.8μm which corresponds to the middle of the bottom contact layer of the detector. Ohmic contacts were then evaporated on the bottom and top contact layers using Ti (500Å) / Pt (500Å) /Au (3000Å) in both the cases. Finally, devices were passivated with a plasma enhanced chemical vapor deposition (PECVD) SiO_2 (~100nm thick) layer. Prior to SiO_2 deposition, the wafer was dipped in an H_3PO_4-based acid solution for oxide removal.

The detector spectral response was measured with Fourier transform IR spectrometer (FTIR) equipped with a glow-bar black body source. Fig. 38 presents the temperature dependent spectral response of the T2SL detector grown on a GaSb (111) substrate measured at -50mV of applied bias. At room temperature, the detector zero-response cut-off wavelength ($\lambda_{100\%\ cut\text{-}off}$) was 5.6μm. Fig. 39 compares zero bias spectral response measured at 77K for two detectors structures with the same design and T2SL composition grown on GaSb (100) and GaSb (111)B substrates. At 77K, the $\lambda_{100\%\ cut\text{-}off}$ of the detector grown on the GaSb (111)B substrate is red-shifted by ~ 1.2μm with respect to the device grown on the GaSb (100) substrate. The difference of $\lambda_{100\%\ cut\text{-}off}$ for both devices measured at the (77-300)K temperature range is shown in the fig. 39 inset. The red shift of the cut-off wavelength demonstrated by the detector grown on the GaSb (111)B substrate is attributed to the increased heavy hole effective mass in the (111) direction, as compared to (100) direction, causing upward shifting of HH1 band that leads to reduction of T2SL effective bandgap. Another interesting feature of the temperature-dependent spectral response of the detector grown on the GaSb (111)B substrate is an increase of the response intensity with temperature.

DISTRIBUTION A: Distribution approved for public release.

Temperature dependent current-voltage curves are presented in fig. 40. At 295K, the device exhibited zero-bias dynamic resistance-area product (R_0A) and dark current density of 0.34 $\Omega\cdot cm^2$ and 0.53 A/cm^2 (under an operational bias of -50mV), respectively, which is significantly lower than R_0A and a dark current density demonstrated by state-of-the-art MWIR InAs/GaSb T2LS detectors grown on GaSb (100) substrates under the same measurement conditions [50-52]. The activation energy (E_a) was extracted from the temperature-dependent dark current data as shown in the inset of fig. 40. At high temperatures (200K-295K), the E_a was very close to the nominal value of the optical band gap of the device (0. 264eV). This behavior indicates that the current is dominated by the diffusion mechanism at high temperatures.

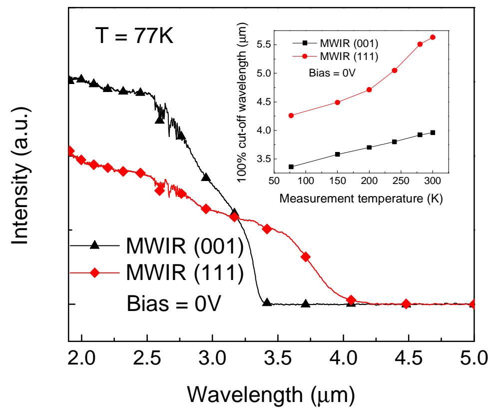

Figure 39. Zero bias spectral response measured at 77K for two detectors structures with the same design and T2SL composition grown on GaSb (100) and GaSb (111)B substrates. The inset illustrates difference of $\lambda_{100\%\ cut\text{-}off}$ for both devices measured at (77-300)K temperature range. [Plis et al, J. Vac. Sci. Technol. B 31, 03C123, 2013]

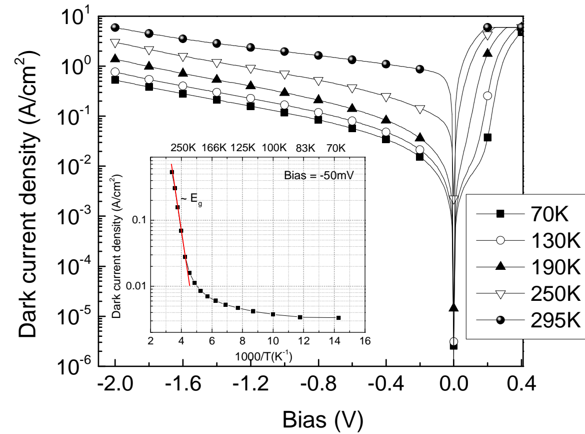

Figure 40. Current voltage characteristics of the T2SL detector grown on the GaSb (111)B substrate measured at selected temperatures. Inset shows the temperature-dependent dark current densities measured at -50mV of applied bias. [Plis et al, J. Vac. Sci. Technol. B 31, 03C123, 2013]

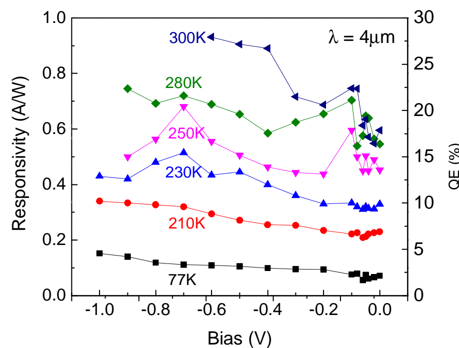

Figure 41. The bias-dependent responsivity and quantum efficiency of the T2SL detector grown on the GaSb (111)B substrate measured within the (77-295)K temperature range at 4μm. [Plis et al, J. Vac. Sci. Technol. B 31, 03C123, 2013]

The radiometric characterization of the T2SL detector grown on GaSb (111)B substrate was performed with a calibrated Mikron blackbody at 800°C. Fig. 41 presents the bias-dependent responsivity and quantum efficiency (QE) of the T2SL detector grown on GaSb (111)B substrate measured within the (77-300)K temperature range at 4μm. At 295K and -50mV of applied bias, the responsivity of 0.63A/W was achieved, corresponding to a QE of 18% (at wavelength of 4μm).

It should be noted that responsivity of the device increases with the measurement temperature. The nature of this phenomenon is not clear yet; however, the similar behavior of quantum efficiency, attributed to the enhancement of the absorption coefficient with increasing temperature, was observed by Li *et al* [53] for the MWIR T2SL device grown on (100) GaSb substrate.

At 295K, the T2SL MWIR detector grown on GaSb (111)B substrate have demonstrated improved electrical performance with dark current density being factor of ~ 2.5 lower than that of MWIR T2SL device with the same architecture and grown on (100) GaSb substrate [54]. Moreover, under zero applied bias the D* value reached 8.5 x

DISTRIBUTION A: Distribution approved for public release.

10^9 Jones for the MWIR T2SL detector grown on (111)B GaSb, which is significantly higher than D* demonstrated by T2SL MWIR detectors with pin [55] and nBn [56] designs grown on (100) GaSb substrates.

3.3. Multimodal Sensing

3.3.1 Plasmonic Focal Plane Array

UNM demonstrated [57] the first monolithically integrated plasmonic camera using near field spectrally resonant coupling of the SPPs with infrared absorption in the quantum dots as an important step towards this broader, biomimetic vision of infrared imaging. Moreover, the plasmonics approach is detector agnostic and can be introduced into a standard imaging camera fabrication process using a single photolithography step. Fig. 42 presents spectral response of the two halves of the plasmonic FPA using amonochromator system. Blue curve corresponds to the spectral response of surface plasmons (SP)-FPA whereas black curve corresponds to the spectral response of FPA. The theoretically modelled (1,0) and (1,1) SP resonances are also shown on the same figure using k = 0.04 and k = 0.02, respectively (k is the imaginary part of the semiconductor dielectric function dominated by the quantum dot infrared photodetector absorption). Green curve shows difference of spectral response between SP FPA and FPA; red (magenta) curve corresponds to the theoretically modelled first (second) order SP resonances using k = 0.04 (0.02). Representative image of the blackbody seen through the open slot (no filter) in the filter wheel assembly is illustrated in Fig. 42 (c). The clear image of the human hand clearly showing temperature differences of < 50 mK should be noted. Infrared image of the blackbody (Figure 30, d) below the (1,1) resonance at λ = 3.99 µm, (Fig. 42, e) near the (1,1) resonance, λ = 4.54 µm, (Fig. 42, f) close to the (1,0) resonance, λ = 5.95 µm and (Fig. 42, g) beyond the (1,0) resonance, λ = 6.83 µm. It is clear that at the (1,0) and (1,1) resonances, the response of the SP-FPA is brighter than that of the non-SP-FPA, whereas the effect is reversed off resonance. This is in very good agreement with the independent spectral response measurements shown in Fig. 42 (a).

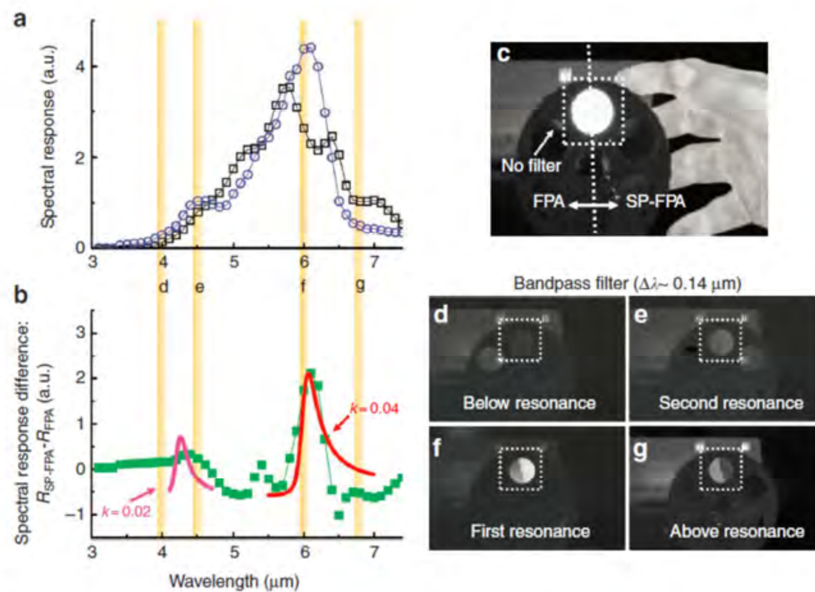

Figure 42. Spectrally resonant enhancement in plasmonic DWELL camera. (a) Spectral response of the two halves of the plasmonic FPA using a monochromator system. Blue, spectral response of SP-FPA; black, spectral response of FPA. (b) Difference plot showing the experimentally observed peaks. The theoretically modelled (1,0) and (1,1) SP resonances are also shown using k = 0.04 and k = 0.02, respectively (k is the imaginary part of the semiconductor dielectric function dominated by the quantum dot infrared photodetector absorption). Green, difference of spectral response between SP FPA and FPA; red (magenta), theoretically modelled first (second) order SP resonances using k = 0.04 (0.02). (**c**) Representative image of the blackbody seen through the open slot (no filter) in the filter wheel assembly. Infrared image of the blackbody (**d**) below the (1,1) resonance at λ = 3.99 µm, (**e**) near the (1,1) resonance, λ = 4.54 µm, (**f**) close to the (1,0) resonance, λ = 5.95 µm and (**g**) beyond the (1,0) resonance, λ = 6.83 µm [Lee et al, Nature Communications 2, 286, 2011]

DISTRIBUTION A: Distribution approved for public release.

3.3.2 Three Color T2SL Detectors

Recently UNM has demonstrated the extension of unipolar barrier architecture to the three-color detector [58]. This three terminal device used a NbNbiP heterostructure with a top N-contact, a middle N-contact and a bottom P-contact. The SWIR and MWIR absorbers were embedded in the nBn architecture between the top and the middle contact and the LWIR absorber is incorporated in the NbIP section between the middle and bottom contact. The dual color nBn device provided sequential SWIR/MWIR detection by switching the polarity of the applied bias. The LWIR detector region was a NbIP heterojunction design with a hole blocking layer sandwiched between absorber region and N contact layer, where "I" refers to absorber region. Calculated equilibrium band diagram showing conduction band and valence band at 77K in the NbNbIP heterostructure is presented in Fig. 43. The position of the superlattice was obtained using semi-empirical psedopotential method, while the bandstructure was calculated using Sentauraus TCAD simulator.

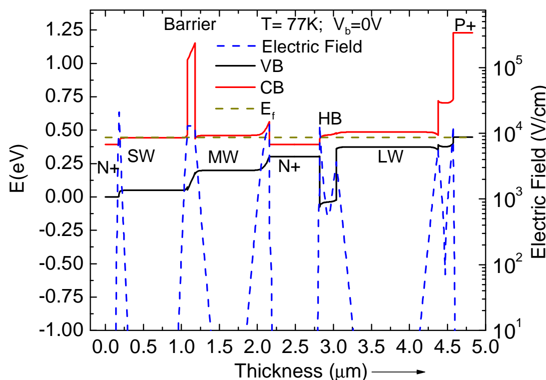

Figure 43. Calculated equilibrium band diagram showing conduction band and valence band at 77K in the NbNbIP heterostructure. The electric field profile across the device for no externally applied bias is also shown [Gautam et al, Appl. Phys. Lett. 98, 121106, 2011]

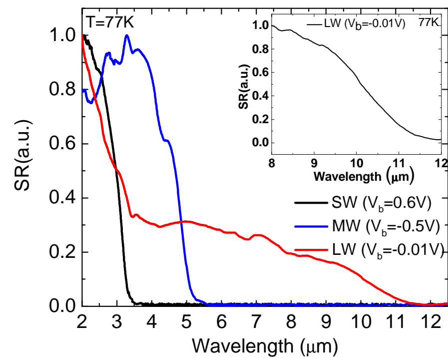

Figure 44. Spectral response of SWIR, MWIR and LWIR absorber regions at 77K. The inset shows response of LWIR absorber from 8μm to 12μm range (since a LWIR band pass filter was used for the calibrated radiometry measurements). [Gautam et al, Appl. Phys. Lett. 98, 121106, 2011]

The hole blocking layer in the LWIR section of the device blocks the flow of minority carrier hole from N contact layer of the device into the absorber region and hence reduces the noise in the system. Moreover, the electric field drops across the wider band gap barrier layer leading to reduced SRH recombination. There is also significant field drop across the T2LS layer sandwiched between the LWIR absorber region and the bottom P+ GaSb contact layer. The LWIR NbIP section can be operated independent of MWIR and SWIR nBn section by applying reverse bias between the middle contact and bottom contact. FPA realization of this device structure would require three bumps per pixel technology. Read out integrated circuits with 3 bumps per pixel (for simultaneous two color detection) have already been demonstrated [59].

Fig. 44 shows the spectral response of the NbNbiP detector when a bias is applied between the top and middle contact, and the bottom contact is floating. When a negative bias is applied to the top contact, photogenerated electrons in the MWIR absorber are collected at the middle contact while the photogenerated holes are collected at the top contact. The electrons from SWIR region are blocked by the barrier layer from reaching the middle contact, thus leading to reduced spectral cross talk. On the other hand, when a positive bias is applied at the top contact, photogenerated electrons from SWIR are collected at the top contact and photogenerated holes are collected at the middle contact. In this case, the electrons from the MWIR absorber are blocked by the barrier layer. The 50% cutoff wavelength (λ_c) for MWIR and SWIR response was 4.7μm (V_b=-0.5V) and 3μm (V_b=0.6V) respectively. The 50% cutoff wavelength of LWIR region was 10.1 μm (77K), as shown in inset of Fig. 28. For LWIR absorber a reverse bias of 10 mV was applied between across middle and bottom contact, while the top contact was floating.

The observed responsivity and quantum efficiency for SWIR, MWIR and LWIR signals were 0.30A/W and 14.9% (λ=2.5μm), 0.41A/W and 12.7% (λ=4μm) and 0.77 A/W and 10.7% (λ=8.94μm) respectively (77K). The

DISTRIBUTION A: Distribution approved for public release.

measured peak specific detectivity for 2π field of view (FOV) and 300K background was of 1.4×10^{10} Jones, 1.8×10^{10} Jones and 1.5×10^{9} Jones for SWIR, MWIR and LWIR signals has been observed.

3.3.3 Dual-band T2SL Detectors

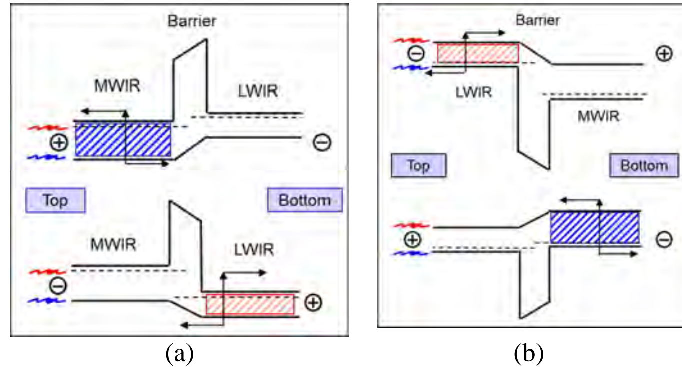

Figure 45. Schematic of (a) nBn and (b) pBp T2SL dual-band detector operation. [Plis et al, IEE Photonics Journal 3, 234, 2011]

UNM worked on development of T2SL detectors for dual-band IR detection targeting MW/LWIR [60] and LW/LWIR [61] wavelength ranges. Fig. 45 demonstrates the schematics of nBn and pBp dual-band T2SL detectors. Typical dual-band T2SL detector with barrier design is composed by two narrow band-gap absorbers aimed at the different IR regions separated by ~ 100 nm thick wide-band-gap material layer with a large barrier for majority carriers and no barrier for minority carriers. As a result, the majority carrier current between the two electrodes is blocked by the large energy offset, while there is no barrier for photo-generated minority carriers. Detector with pBp design is expected to demonstrate faster operation with smaller integration times, due to the higher mobility of the minority carriers, electrons.

Fig. 46 shows the normalized spectral response of dual-band MW/LWIR InAs/GaSb T2SL detector with (b) nBn and (b) pBp design measured at 77K. Measurements were performed with Fourier transform IR spectrometer (FTIR) equipped with glow-bar black body source. Both detectors were composed by 2 µm thick MWIR absorber grown on top of 2 µm thick LWIR absorber separated by a 100 nm barrier.

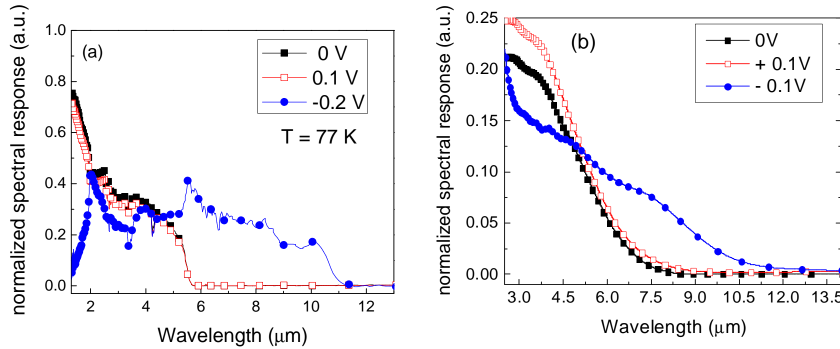

Figure 46. Normalized spectral response of dual-band InAs/GaSb SLS detector with (a) nBn and (b) pBp designs measured at 77 K. [Plis et al, IEE Photonics Journal 3, 234, 2011]

For nBn detector, under forward bias, which is defined as positive voltage applied on the top contact, the photo carriers are collected from the MWIR T2SL absorber. When the device is under reverse bias, which is defined as negative voltage applied on the top contact, the photo carriers from the LWIR T2SL absorber are collected, while those from the MWIR absorber are blocked by the barrier.

The zero-response cut-off wavelengths ($\lambda_{50\%}$) of MWIR and LWIR absorbers were equal to ~5 µm and ~ 10.0 µm, respectively (77 K).

For pBp detector, under forward bias, which is defined as negative voltage applied on the bottom contact, the photo-generated carriers are collected from the MWIR absorber. When the device is under reverse bias, which is defined as positive voltage applied on the bottom contact, the photo-generated carriers from the LWIR absorber are collected, while those from the MWIR absorber are blocked by the barrier. The zero-response cut-off wavelengths ($\lambda_{50\%}$) of MWIR and LWIR absorbers were equal to ~5 µm and ~ 9.0 µm, respectively (77 K).

Fig. 47 presents temperature dependent dark current densities of dual-band InAs/GaSb T2SL detector s with nBn and pBp designs measured at various temperatures. For nBn design, at 77 K, the dark current density was equal to 1.4 x 10^{-3} A/cm^2 at -0.16 V (LWIR absorber) and 7.6 x 10^{-4} A/cm^2 at + 0.1 V (MWIR absorber). For pBp design, at the same temperature, the dark current density was equal to 6 x 10^{-5} A/cm^2 at +0.1 V (MWIR absorber) and 5 x 10^{-4} A/cm^2 at - 0.1 V (LWIR absorber). The dual-band detector with pBp design has demonstrated the considerably lower dark current at (-0.3V; +0.5V) region of applied bias.

DISTRIBUTION A: Distribution approved for public release.

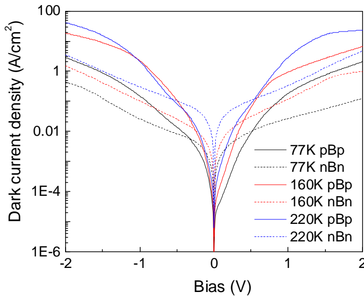

Figure 47. The temperature dependent dark current densities of dual-band InAs/GaSb T2SL detectors with nBn and pBp designs. [Plis et al, IEE Photonics Journal 3, 234, 2011]

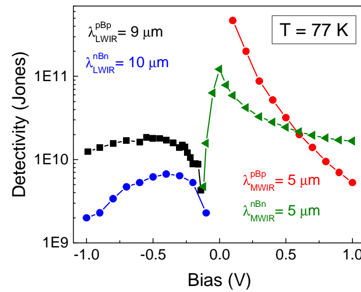

Figure 48. Detectivity D* of InAs/GaSb dual-band T2SL detector with nBn and pBp designs estimated at 77K [Plis et al, IEE Photonics Journal 3, 234, 2011]

Specific detectivity D* estimated for T2SL MW.LWIR detectors with nBn and pBp designs is presented in fig. 48 For nBn detector, values of specific detectivity at 77 K has reached the maximum values of 1.2 x 10^{11} Jones (at λ = 5 µm and V_b = 0 V) and 1.8 x 10^{10} Jones (at λ = 10 µm and V_b = -0.45 V) for MWIR and LWIR absorbers, respectively.

For pBp detector, values of specific detectivity at 77 K has reached the maximum values of 5 x 10^{11} Jones (at λ = 5 µm and V_b = + 0.1 V) and 2.6 x 10^{10} Jones (at λ = 9 µm and V_b = -0.4 V) for MWIR and LWIR absorbers, respectively.

It should be noted the detector is operated under small values of applied bias compared to nBn dual-band T2SL detector, thus suggesting the higher mobility of carriers.

3.4 Heterogeneous Material Integration

3.4.1. *Imaging with Metamaterial Spatial Light Modulators (SLM)*

UNM participated in a collaborative effort between Boston and Duke Universities to demonstrate compressive techniques allowing the acquisition of high-frame-rate, high fidelity images. The proposed system is all solid-state with no moving parts, yields improved signal-to-noise ratios over standard raster-scanning techniques and uses a source orders of magnitude lower in power than conventional set-ups. The demonstrated imaging system establishes a new path for terahertz imaging that is distinct from existing focal-plane-array-based cameras. Schematic of the single-pixel imaging process utilizing an SL is presented in Fig. 49 (a). An image is spatially modulated by the metamaterial and the resulting radiation is sent to the single-pixel detector. Photograph of the SLM (courtesy of K. Burke, Boston College Media Technology Services) is shown in Fig. 49 (b), the total active area of the SLM is (4.8 mm^2). Spatial map of maximum differential absorption for an example Hadamard mask over a photograph of the SLM device is presented in Fig. 49 (c). Color bar reflects maximum differential absorption for that pixel. Frequency-dependent absorption of a single pixel (referenced to a gold mirror) for two bias voltages, 0 V reverse bias (blue curve) and 15 V reverse bias (red curve) is presented in Fig. 49 (d). Finally, differential absorption (A15V – A0V) as a function of frequency is demonstrated in Fig. 49 (c).

DISTRIBUTION A: Distribution approved for public release.

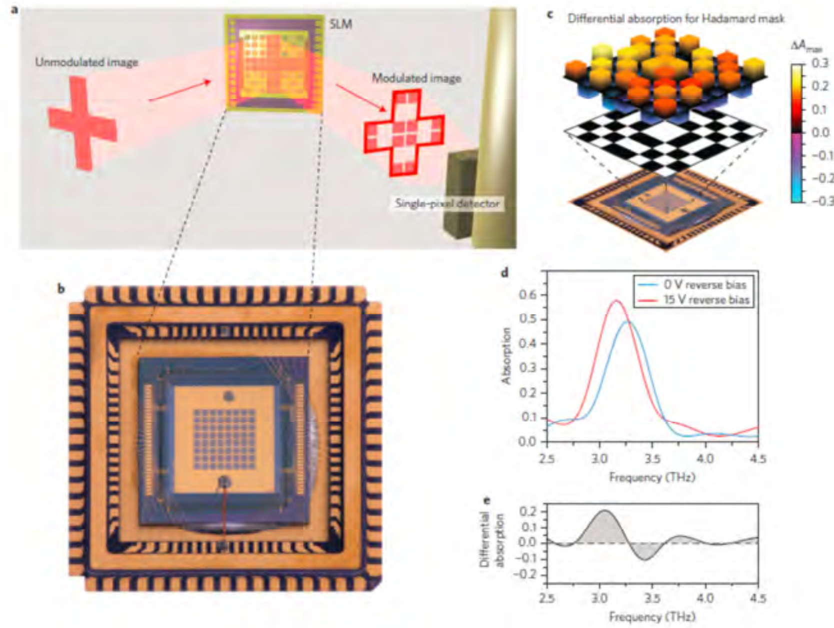

Figure 49. (a) Schematic of the single-pixel imaging process utilizing an SLM. An image is spatially modulated by the metamaterial and the resulting radiation is sent to the single-pixel detector. (b) Photograph of the SLM (courtesy of K. Burke, Boston College Media Technology Services); total active area of the SLM is (4.8 mm2). (c) Spatial map of maximum differential absorption for an example Hadamard mask over a photograph of the SLM device. Colour bar: maximum differential absorption for that pixel. (d) Frequency-dependent absorption of a single pixel (referenced to a gold mirror) for two bias voltages, 0 V reverse bias (blue curve) and 15 V reverse bias (red curve). (e) Differential absorption (A15V – A0V) as a function of frequency [Watts et al, Nature Photonics 8, 605, 2014]

3.4.2. Semiconductor Nano-scale Transistors on Insulating Layers

UNM (with collaboration with University of Berkeley) explored the approach of T2SL integration on alternate substrates, such as Si. The transfer of InAs ultrathin membranes onto Si/SiO_2 substrates to form high-performance n-type FETs (n-FETs), termed "XOI" was demonstrated first. Then the XOI concept was extended to $InAs_xSb_{1-x}$ material. Details of XOI process are presented in Fig. 50. The epitaxially grown, single-crystal InAs films are patterned with PMMA and wet etched into nano-ribbon arrays. A subsequent selective wet etch of the underlying AlGaSb layer and the transfer of nano-ribbons by using an elastomeric PDMS slab result in the formation of InAs nano-ribbon arrays on Si/SiO_2 substrates. The nanoribbons are ~ 10 µm long, 18nm high, and 300nm wide.

DISTRIBUTION A: Distribution approved for public release.

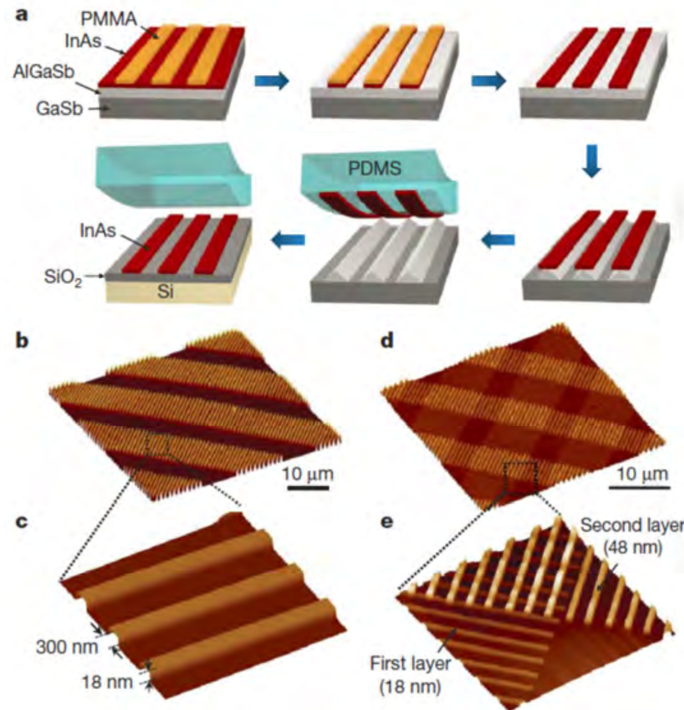

Figure 50. Fabrication scheme for ultrathin InAs XOI, and AFM images. (a) Schematic procedure for the assembly of InAs XOI substrates by an epitaxial transfer process. (b, c) AFM images of InAs nanoribbon arrays on a Si/SiO_2 substrate. (d, e) AFM images of InAs nanoribbon superstructures on a Si/SiO_2 substrate, consisting of two layers of perpendicularly oriented nanoribbon arrays with 18- and 48-nm thicknesses, as assembled by a two-step epitaxial transfer process. Adapted from Ko *et al*, Nature **468**, 286 (2010).

3.4.3. MWIR T2SL Detectors Integrated with Plasmonic Coupler

Recently, UNM demonstrated resonant enhancement at 4 µm in InAs/GaSb T2SL detectors through coupling with plasmonic structures [62]. Corrugated metal surface (CMS) consisting of 2-D square array of Germanium (Ge) posts covered with a 250nm-thick gold (Au) film, has been fabricated on top of a of T2SL MWIR detector with 200 nm thick active region. Ge has been used as a higher refractive index material to localize the SPW modes to the surface. For substrate side illumination (SSI), the CMS provides strong coupling to SPWs resulted in up to three times enhancement of the QE compared to a reference T2SL detector at 77 K.

Fig. 51 demonstrates the detector and plasmonic coupler fabrication process. First, normal incidence single-pixel detectors with 300 µm apertures and 410 µm ×410 µm mesas were realized using standard optical photolithography techniques. Next, about 100 nm thick Ge blanket layer was deposited in the device apertures followed by the fabrication of 2D Ge post arrays Interferometric Lithography (IL). Diameter and height of individual posts in 2D arrays were ~ 0.5 um and 100 nm, respectively, with period of ~ 1µm. Finally, CMS was obtained by covering 2D Ge arrays with 250 nm layer of Au. This layer was covered the aperture area with 280 µm diameter and 250 nm thickness.

In order to demonstrate the effect of CMS plasmonic coupler integrated with the T2SL detector, the SSI spectral response, dark current density and QE were evaluated for the single pixel detector with fabricated CMS inside the optical aperture and compared to the reference device (bare device with no metal and no Ge which). SSI spectral response measurements were performed with a Fourier transform IR spectrometer (FTIR) equipped with a glow-bar blackbody source. SSI spectral response curves for the CMS and reference devices measured at 77K and zero applied bias are shown in Fig. 52 (a) The 100% cut-off wavelength for both detectors was ~ 5 µm. The broadband spectral response was enhanced by factor of 2.5 with the resonance peak at 3.8 µm. It was attributed to the 1µm period 2D CMS array. The measured dark current densities of the CMS and reference devices, at 77K are presented in Fig. 52 (b). Since surface-to-volume ratio is the same for both devices, they are, as expected, demonstrated the same noise level (dark current density is $8.5e^{-6}$ A/cm^2 at negative 0.01 volts).

DISTRIBUTION A: Distribution approved for public release.

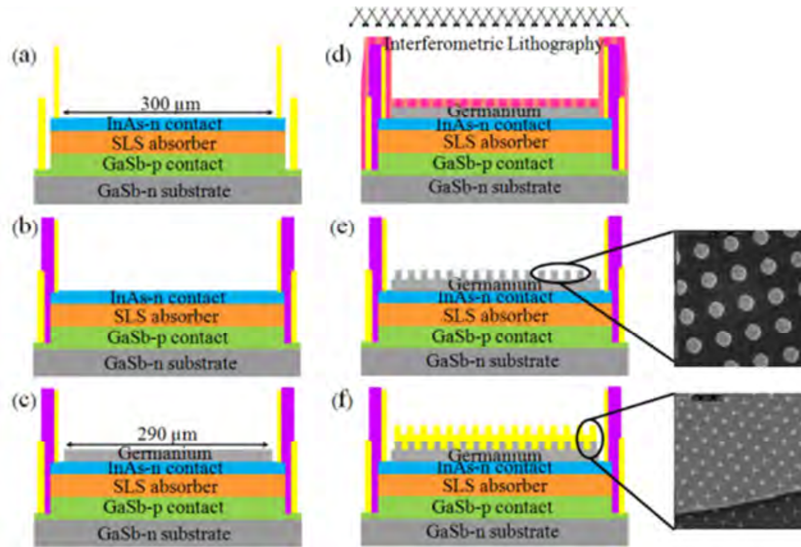

Figure 51. Detector and plasmonic coupler fabrication process: (a) mesa definition and metal contact deposition, (b) passivation, (c) Ge blanket deposition, (d) I , (e) Ge post deposition, (f) metal (Au) deposition. [Zamiri et al, Proc SPIE 90700, 9700Y, 2014]

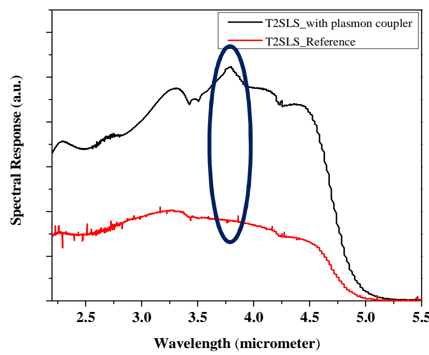

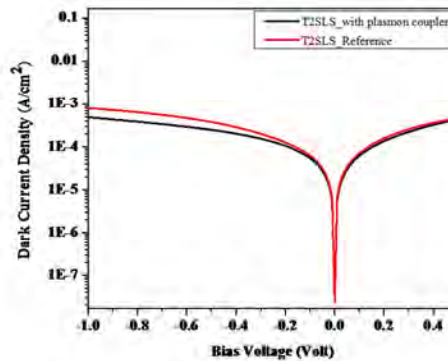

(a) (b)

Figure 52. (a) SSI spectral response of the T2SL device with plasmon coupler and reference device at 77K (b) Dark current densities of CMS T2SL and reference detectors measured at 77K. [Zamiri et al, Proc SPIE 90700, 9700Y, 2014]

DISTRIBUTION A: Distribution approved for public release.

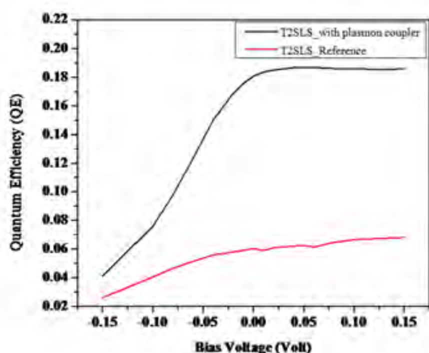

Figure 53. QE of CMS T2SL and reference detectors. A factor of three enhancement is obtained for the device that utilizes light coupling through a plasmonic structure. [Zamiri et al, Proc SPIE 90700, 9700Y, 2014]

The QE measurement was used to compare the signals produced by devices. QEs were measured with a calibrated
blackbody at 627ºC. It should be noted that the photoresponse for device with CMS on its optical aperture was clearly enhanced over the reference (bare) device. Fig. 53 shows that the QE results for the reference device under 0 mV bias and 77K is ~ 6%; and the QE increases to ~ 18% for the device with plasmonic coupler. Since dark current was the same for both devices, while the QE was enhanced by a factor of three by using the CMS and a thinner T2SL absorber, a larger detectivity or SNR is obtained.

3.5 Passivation of T2SL Detectors

Fabrication of InAs/GaSb T2SL detectors involves definition of the physical dimensions of the device, which results in the exposure of its sidewalls formed by InAs, GaSb and, in part, InSb and GaAs layers. During the individual pixel isolation process, the periodic crystal structure terminates abruptly resulting in formation of unsatisfied (dangling) chemical bonds responsible for generation of surface states within the bandgap. These states cause pinning of the surface Fermi level near the midgap and, as a consequence, enhance the surface leakage currents. Moreover, the surface leakage currents become a dominant contributor to the dark current for FPA pixels with mesa dimensions of ~20 µm. Thus, in order to improve the overall device performance, methods for elimination of surface currents, i.e. passivation treatments, have to be developed for InAs/GaSb T2SL material system.

Work on passivation of InAs/GaSb T2LS detectors follows in two main directions. The first one is deposition of relatively thick insulator layers of dielectrics, organic materials (polyimide and various photoresists), or widerband gap III-V materials. In this case, the semiconductor/insulator heterojunction with properties defined by the density of states at the interface is formed. The second direction is modification of the atomic structure of the surface by foreign atoms which changes the electronic structure of the semiconductor surface. This is chalcogenide passivation, i.e. saturation of unsatisfied bonds on semiconductor surface by S-atoms.

We compared different passivation schemes applied to the T2SL detectors with pBiBn PIN designs operating in the LWIR spectral region (100% cut-off wavelength of ~ 12 µm at 77K) [63]. In particular, we studied dielectric passivation (silicon nitride and silicon oxide), photoresist (SU-8), chalcogenide (ammonium sulfide and zinc sulfide), and electrochemically deposited sulfur passivation treatments. Details of every passivation treatment are summarized in Table 4. It should be noted that in case of $(NH_4)_2S$ passivation the native oxides are etched by $(NH_4)OH$ formed in water solution of ammonium sulfide.

Table 4. Studied passivation techniques

Passivation Technique	Pre-passivation treatment	Deposition Technique	Deposition Temperature	Final Thickness
SiN_x	H_3PO_4:H_2O_2:H_2O (1:2:20)-20sec dip	PECVD	300 °C	2000 Å
SiO_2		E-beam-evaporator	170 °C	2000 Å
ZnS			RT	2000 Å
SU-8		Spun		1.5 µm
ECP		Wet bath-Na_2S in Ethylene glycol		A few MLs
$(NH_4)_2S$	N/A	Wet bath-20% $(NH_4)_2S$:H_20 (1:4)		A few MLs

DISTRIBUTION A: Distribution approved for public release.

Device fabrication was initiated using standard optical photolithography to define a variable area diode array (VADA) patterns with areas ranging from 30 µm x 30 µm to 400 µm x 400 µm. Etching was performed using inductively coupled plasma (ICP) reactor with BCl_3 gas. The resulting etch depth corresponded to the middle of the bottom contact layer of the detector. Next, ohmic contacts were evaporated on the bottom and top contact layers using Ti (500 Å) / Pt (500 Å) /Au (3000 Å) in both cases. Passivation efficacy was evaluated by measuring current-voltage (I-V) dependence at 77 K for VADA detectors. All I-V measurements were conducted on variable-temperature Janis ST-500 micromanipulated probe station under zero field of view.

Fig. 54 (a) shows the dark current density of PIN T2SL detectors unpassivated and passivated by various treatments measured at 77 K as a function of VADA mesa area. The dielectric and photoresist passivation treatments (SiN_x, SiO_2, and SU-8) resulted in improvement of dark current density by factors of ~ 2.5, 6, and 13, respectively, compared with the unpassivated device with the same area. We attribute this to the band bending at the semiconductor surface caused by the nature of band alignment at the pasisivant-semiconductor interface and the presence of fixed charges inside the passivation layer. The fixed charge density in electron-beam evaporated ZnS is expected to be lower than in SiN_x deposited under a plasma environment [64]. In addition, ZnS facilitates saturation of surface states by formation of sulphur bonds by constituent atoms of InAs/GaSb T2SL. Both of these factors should result in better passivation efficacy of ZnS. However, we found improvement of dark current density in ZnS passivated devices by a factor of 3, which is comparable with that obtained by using SiN_x passivation. This may be the result of the inferior quality of deposited ZnS film. The electrochemical sulphur (ECP) deposition and ammonium sulfide treatment appeared to be the best passivants, reducing dark current density of 50 µm x 50 µm devices by factors of ~ 200 and 25, respectively. Both of these passivants saturate the surface states by sulphur and create an ordered layer of sulphur adatoms on the semiconductor surface [65]. Only these passivation treatments have been used for the passivation of pBiBn detector.

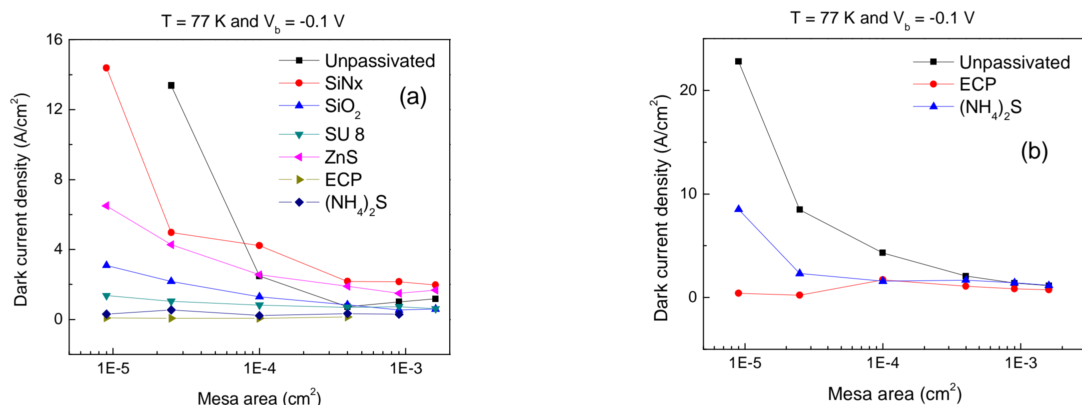

Figure 54. (a) Dark current density vs mesa area of (a) unpassivated and passivated by various treatments T2SL detector with PIN design and (b) unpassivated and passivated by ECP and ammonium sulfide T2SL detector with PbIbN design measured at 77 K [Plis et al, Inf. Phys. Tech 55, 772, 2012]

Fig. 54 (b) presents the dark current density vs VADA mesa area of unpassivated and passivated by ammonium sulfide and ECP treatments for T2SL detector with PbIbN design measured at 77 K. The dark current density of 30 µm x 30 µm detector was reduced by factors of ~ 3 and 54 for the $(NH_4)_2S$ and ECP treatments, respectively. Thus, chalcogenide passivation through an immersion in a sulfur-containing solution, or deposition of a sulfur based layer, effectively reduces dark currents of T2SL LWIR detectors.

Moreover, UNM investigated the thioacetamide (C_2H_5NS or TAM) passivation as an alternative sulfidizing agent for the passivation InAs/GaSb LWIR photodiodes. Depending on the preparation method, the TAM solution may be acidic or basic, in contrast with always basic aqueous solution of $(NH_4)_2S$. As a result, a TAM treatment offers formation of more stable M–S bonds, where M is Ga, In, As or Sb, than ammonium sulfide treatment resulting in weaker M–O–S bonds Moreover, the TAM treatment does not produce elemental antimony on the semiconductor surface thus eliminating the conduction channel parallel to the semiconductor-atmosphere interface. Electrochemical passivation involves the deposition of elemental sulfur in a controlled electro-chemical bath through the decomposition of Na_2S in ethylene glycol. The electrochemical sulfidization provides a uniform sulfur coating with a high-density of S atoms, as was proven by scanning electron microscopy imaging and (obliquely) by good long-term stability of passivated surfaces, respectively. We compared the effectiveness of the two alternative

DISTRIBUTION A: Distribution approved for public release.

sulfur-based passivations, TAM and electrochemical sulfur deposition, on the performance of LWIR InAs/GaSb T2SL detectors.

The detector heterostructure utilized the graded band gap W-design T2SL with cut-off wavelength of ~ 10.5 µm at 77 K was fabricated into variable-area detector array using standard fabrication techniques.

To perform TAM passivation the samples were immersed in a 0.18 M CH_3CSNH_2 solution for 40 min at 70 C. The pH of the TAM solution was adjusted to be acidic (pH = 2.4) or basic (pH = 10.4) by adding an acetic acid (10%) or NH_4OH(30%), respectively. For comparasion, several detectors were passivated by electrochemical sulfur treatment. The electrochemical cell for the sulfur passivation consisted of the sample (anode), a platinum mesh electrode (cathode) and the electrolyte in a glass beaker at room temperature. The electrolyte was 0.1 M Na_2S in ethylene glycol. Immediately before each passivation treatment the native oxides were removed by placing samples in a phosphoric acid based solution (H_3PO_4:H_2O_2:H_2O = 1:2:20) for 30 s.

Comparison between dark current densities of as-etched devices and devices treated by the different passivations schemes, each having perimeter-to-area ratio (P/A) of 1600 cm^{-1} is shown in figure 55 (a). Under a typical operating bias of -0.1 V, the dark current density decreased from 0.8 A/cm^2 for unpassivated samples to 0.3 A/cm^2 and 0.04 A/cm^2 for acidic and basic solutions in the TAM treatments, respectively, and to 2.7 x 10^{-3} A/cm^2 for the ECP treatment.

Figure 55 (b) presents the estimated shot-noise limited D* as a function of applied bias for the detectors with the various passivation treatments and the control sample evaluated at 77 K. At an operating bias of -0.1 V, the ECP passivated device resulted in an improvement in the shot-limited D* by a factor of 5 compared to the unpassivated device. The quantum efficiency (QE) is equal 12% at the same value of applied bias for the unpassivated and passivated samples.

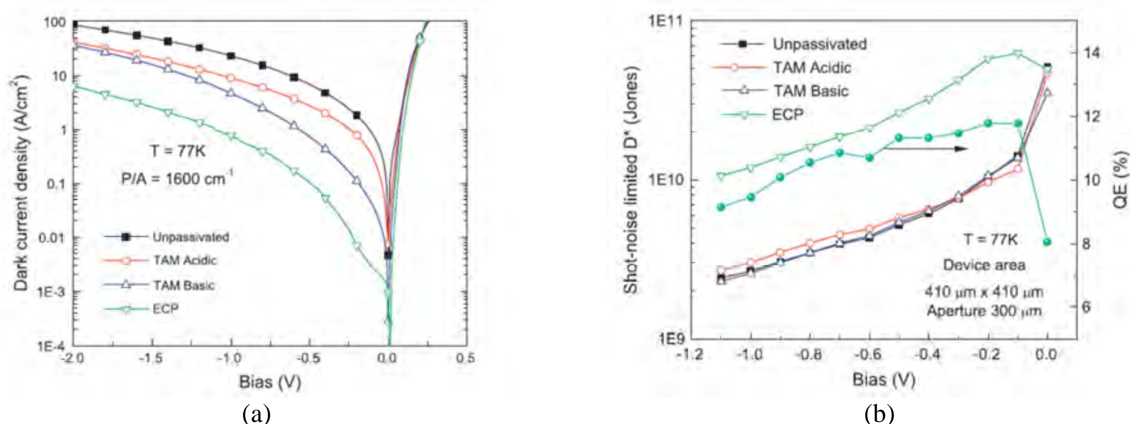

Figure 55. (a) Comparison between dark current densities of as-etched devices and devices treated by the different passivations schemes, each having perimeter-to-area ratio (P/A) of 1600 cm^{-1} (b) the estimated shot-noise limited D* as a function of applied bias for the detectors with the various passivation treatments and the control sample evaluated at 77 K. [Plis et al, Inf. Phys. Tech 55, 772, 2012]

In conclusion, we evaluated the electrical behavior of detectors passivated by two different sulfur-based treatments, TAM (acidic and basic), and ECP. ECP passivated detectors with perimeter-to-area ratio of 1600 cm^{-1} exhibited superior performance with surface resistivity in excess of 10^4 Ohm-cm, dark current density of 2.7 x 10^{-3} A/cm^2, and specific detectivity improved by factor of 5 compared to unpassivated devices (V_{bias} = -0.1 V, 77 K).

3.6 Large-Area Semiconducting Graphene Nanomesh Tailored by Interferometric Lithography

Graphene has risen as a fascinating two-dimensional (2D) material for its high carrier mobility[66], flexibility[67], transparency[68], and its extraordinary ability to withstand mechanical stress[69]. Due to these properties, graphene lends itself to many applications in electronics[70,71], optoelectronics[72],[73], sensing, and energy storage[74,75]. However, graphene lacks a bandgap, which limits its application in digital electronics and optoelectronics. Extensive efforts[76,77,78,79, 80, 81, 82, 83, 84, 85, 86] have been made to create semiconducting graphene without disrupting its exceptional transport properties. One scheme is to obtain bandgap through quantum confinement in graphene nanoribbons (GNRs)[87,88] and graphene nanomesh (GNM)[89] with a critical dimension lower than 10 nm. These nanostructures enable graphene to have potential applications in electronic and photonic devices, such as highly

DISTRIBUTION A: Distribution approved for public release.

sensitive sensors[90,91], in next-generation spintronics[92,93], and in energy harvesting[94,95] devices. Duan and co-workers, fabricated semiconducting graphene using copolymer lithography and demonstrated that GNM-based field-effect transistors (FETs) exhibit comparable ON/OFF current ratios but 100 times higher drive currents than those of the similar devices based on individual GNRs. Furthermore, because of its excellent stability, 2D nature, and high electrical sensitivity, GNM is a good candidate to replace traditional solid-state nanoporours materials in fabrication of composite materials[96] and electrochemical capacitors[97] as well as in DNA sequencing[98].

The fabrication of graphene nanomesh for practical applications demands efficient nanopatterning technologies to inexpensively produce nanoscale periodic modulations over large-areas. To our knowledge, a reliable technology with a wafer-scale fabrication capability for graphene nanomesh has remained a challenge. E-beam lithography is a highly versatile technique to fabricate graphene nanostructures. However, it is not an economically viable approach when large-scale production is required[99,100]. Chemical methods, such as copolymer lithography and imprint lithography[101] can meet the minimum feature size requirement, but they rely on rather complex operations, and are still limited to microscale areas[102].

We demonstrate the use of interferometric lithography (IL)[103,104,105,106,107,108,109] combined with oxygen (plasma treatment to fabricate GNMs with sub-10 nm neck widths and high uniformity over an area. Our approach is facile, inexpensive, and high throughput with well-known processing steps, which have been well characterized for decades, and is compatible with the integrated circuits (IC) manufacturing technology[110]. Atomic force microscopy (AFM) and Raman spectroscopy were used in characterizing the neck width of GNMs fabricated with our approach. The relative intensity of the D band demonstrates an increase with decreasing width. We also observed a blue shift and drastic broadening in the G band of the narrowest GNM, which can be attributed to the size and edge effects. FETs with GNM channel widths of 2 mm were fabricated to demonstrate its application in electronic devices. Transfer characteristics of the GNM-device were studied at room and cryogenic temperatures. The GNM-FET with neck width of ~10 nm shows promising drive current values and ON/OFF current ratio at room temperature. Bandgap modulation was observed by tuning the source-drain voltage. In addition, the ON/OFF current ratio of the GNM-FET displays distinct temperature dependence with a significant enhancement at 77 K.

Figure 56 illustrates the process flow for fabrication of the graphene nanomesh (GNM). We used commercially available single-layer (SL), chemical vapor deposited (CVD) graphene on a 285 nm silicon dioxide /p+ silicon substrate (Figure 56a). The sample is spin-coated with negative photoresist (PR) and a square 2D hole array pattern is impressed in the photoresist by IL (Figure 56b). Subsequently, an isotropic plasma etching is employed to reduce the PR neck width. In addition, the plasma removes the unprotected graphene regions, which leads to a reduction in the graphene width still coated with PR (Figure 56c). After the etching process is completed, the PR is removed by soaking the sample in acetone to obtain the exposed GNM (Figure 56d).

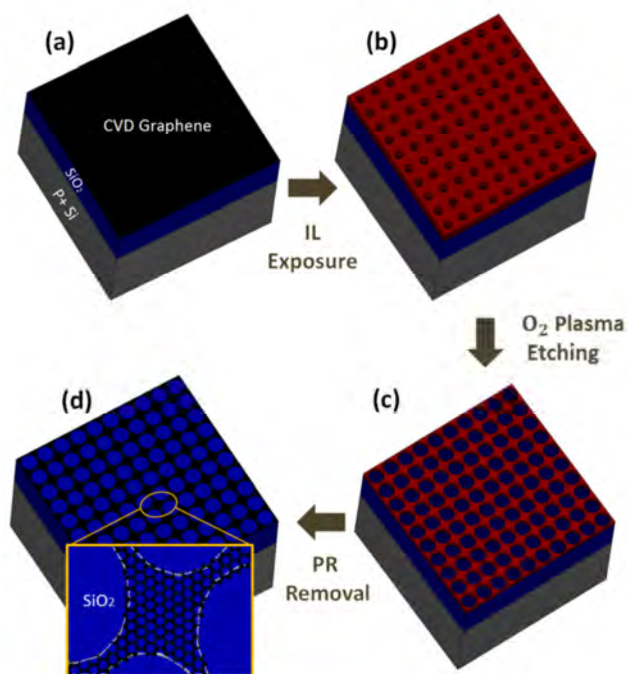

Figure 56. The overall fabrication route of GNM, based on interferometric lithography and plasma etching. (a) SL-CVD graphene on 285 nm-thick layer and p+ Si substrate. (b) The sample is covered with a spin-coated negative photoresist (PR). A square 2D hole array pattern is made in the PR by IL. (c) To define the mesh structure, isotropic plasma etching is performed at high pressures, to reduce the PR line width, which leads to a reduction in the graphene width under the photoresist. (d) The PR mask is removed after a brief soak in acetone solution.

The narrow neck regions of the GNM strongly affect the charge transport through the structure. Hence, the ability to precisely control the neck width is crucial for modulating the electronic properties in GNM. For GNMs made by IL, the neck width is tailored independently by varying the laser exposure dose and

DISTRIBUTION A: Distribution approved for public release.

etching duration (Supplementary Information). We demonstrate the scalability of our approach by first making a highly uniform PR hole array pattern (working as etch mask) on three individual SL-CVD graphene samples and then performing plasma etching on the processed samples for different time durations. The initial PR width and periodicity in the PR are ~70 nm and ~150-200 nm, respectively. Figure 57a, b show the cross section and top-view of a representative hole array mask. An optimized isotropic plasma etching was carried out separately for 30, 60, and 80 seconds on the processed samples. The corresponding SEM images are shown in Figures 57(c-e). The cross-section SEM image in Figure 57a reveals the corrugated sidewalls of the holes in the PR due to standing waves, because no anti-reflection coating (ARC) layer was used in IL exposures. Therefore, a narrower GNM is expected compared to the hole array width on the PR surface. Figure 57g plots the average PR/GNM width as a function of etching time. A low magnification SEM image of the PR pattern on graphene after 80 seconds of etching is shown in Figure 57f to show the uniformity of IL exposure and plasma etch.

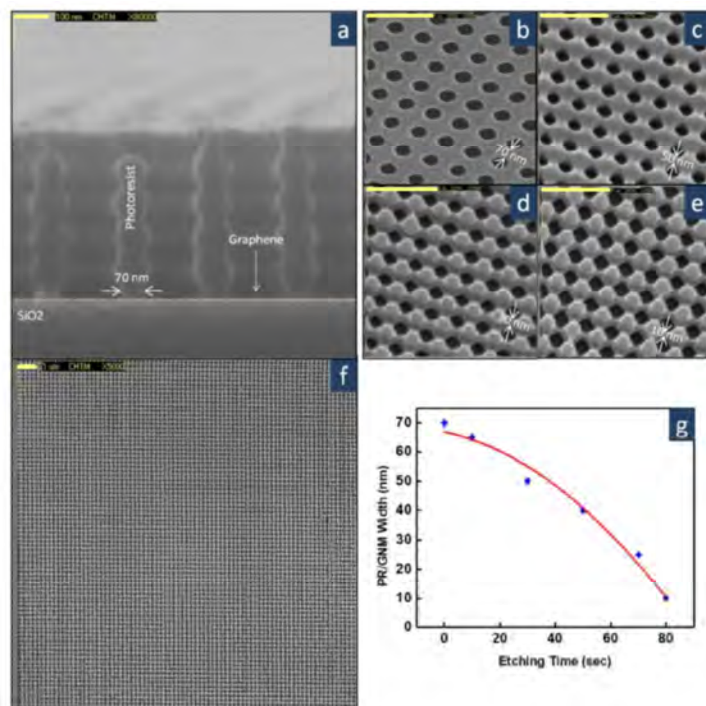

Figure 57. SEM images demonstrate the effect of etching on the PR/GNM line-width. (The scale bar for (a) is 100 nm; all the other scale bars are 1 µm). (a) Side view image of the PR hole array mask made on graphene film after the IL exposure, soft bake, and develop. The nominal PR width above the graphene film is ~70 nm. (b) Top view image of the PR hole array mask. (c) PR pattern after plasma applied for 30 seconds. Due to the high pressure, the etching process was found to be dominantly lateral. The PR width is ~ 50 nm. (d) PR pattern after plasma applied for 60 seconds, PR width ~30 nm. (e) Final step of etching when the PR width is reduced to ~10 nm after 80 seconds of etching. (f) Large-scale top-view image of the PR pattern after 80 seconds of etching. This pattern is continuously written across a wafer. (g) Plot of experimentally measured PR/GNM width as a function of the etching duration, which is fitted with a solid red line.

AFM images to characterize GNM neck-width were acquired from different regions of the GNM (Figures 58 a-c) show GNMs with variable neck widths in the range of 6-20 nm. More than 75% of the GNMs have neck widths between 8 nm and 12 nm. The standard deviation of the neck width is less than 3 nm over the entire GNM sample, and the smallest neck width measured is ~7±1 nm. The AFM height profile of a typical GNM (Supplementary Information) suggests that after the standard cleaning of the sample, a thin PR residue ~15-20 nm is left on the graphene sheet, which potentially introduces some doping[111] in the GNM and also affects the charge carrier mobility[112] in the mesh structure. The nanomesh feature, with very minor breaks, was observed over the wafer. The AFM profile studies on a set of samples with different etching durations (Supplementary Information) clearly reveal that highly uniform GNMs can be obtained with controllable neck widths using interferometric lithography.

DISTRIBUTION A: Distribution approved for public release.

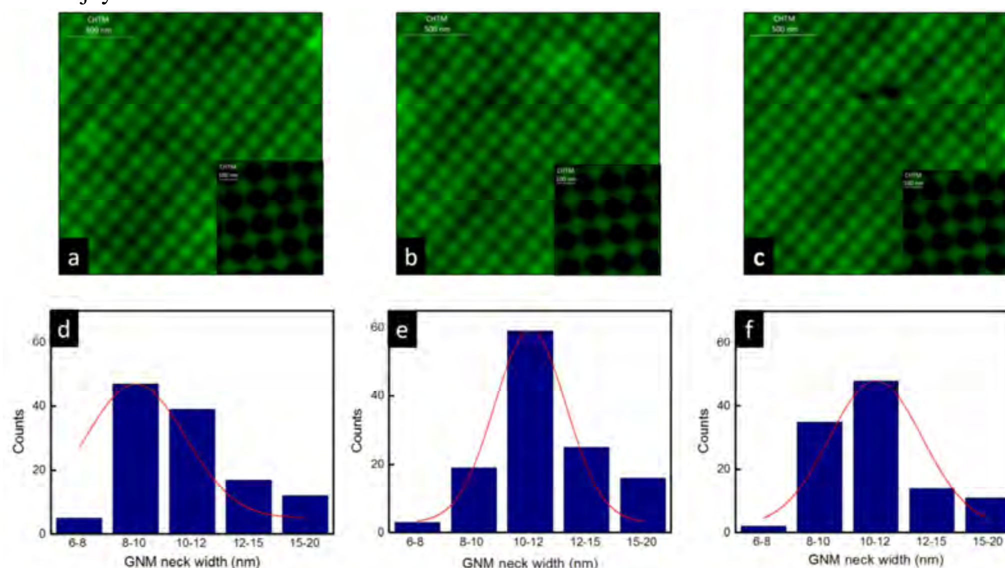

Figure 58. AFM images of the narrowest GNM and statistical analysis of the neck widths. (a)-(c) AFM images acquired from three different spots on the GNM sheet etched for 80 seconds. Insets in a–c, show high-magnification images. (d)-(f) Histograms of neck widths for a–c fitted with a Gaussian function.

In order to study the physical and electronic characteristics of the processed samples, the GNMs with varying neck widths were characterized using Raman spectroscopy. The Raman spectrum acquired from unpatterned graphene (Figure 59a, black line) shows the G band centered at 1587, which corresponds to the stretching vibration of carbon atoms[113]. Also a symmetric 2D band of the double resonance process is found centered at 2685 with a full width at half-maximum (FWHM) of 32. For the unpatterned graphene, only a low-intensity or no D band was observed. In contrast, for GNMs with varying neck widths, we observe an increase in the relative intensity of the D band (centered at 1352) as the mesh neck width decreases (Figure 59a). We attribute this feature to the increasing edge-to-surface ratio areas in samples with smaller neck widths[114]. The ratio of the unpatterned graphene and GNMs with different neck widths are shown in Figure 59b. As shown in Figure 59b, the G band characteristic of the GNM with 10 nm neck width is noticeably broader (10) and blue shifted by 11 compared to the G band dominating the spectrum of unpatterned graphene. This trend may be attributed to quantum confinement or localization effects resulting from edge disorders such as variable edge roughness in GNM[115,116,117]. In addition the GNM mesh was patterned using plasma in a condition that is known to form oxygen-containing functional groups in graphite[118]. Because oxygen is more electronegative than carbon, such functional groups are expected to withdraw π electrons of GNM (i.e., dope with holes) and that potentially can induce a blue shift in the G band[119]. However, for the GNM with neck widths of ~50 nm, no shift or broadening was observed (Figure 59b), which suggests that the doping effect is less dominant. Also, because the narrowest GNM in this study has a sub-10 nm neck width, a non-negligible confinement effect is expected. To validate the observed behavior of the G-band, multiple Raman scans were performed at different locations across the narrowest GNM sample. Figure 59c (inset) shows plots of the G-band peaks acquired at four different locations on the sample. The results plotted in Figure 59c show that all of the G band peaks tend to stay at approximately 1605 by a maximum shift of 17 with respect to the unpatterned graphene. Also, the measured FWHM of the G bands at the four locations are within a range of 42-47, indicating that, on average, the G band of the GNM is 10 broader than that of the unpatterned graphene. The blue shift and broadening of the G band for the narrowest GNM is likely due to the lateral quantum confinement and localization effects and/or chemical doping by functional groups on the GNM edges.

DISTRIBUTION A: Distribution approved for public release.

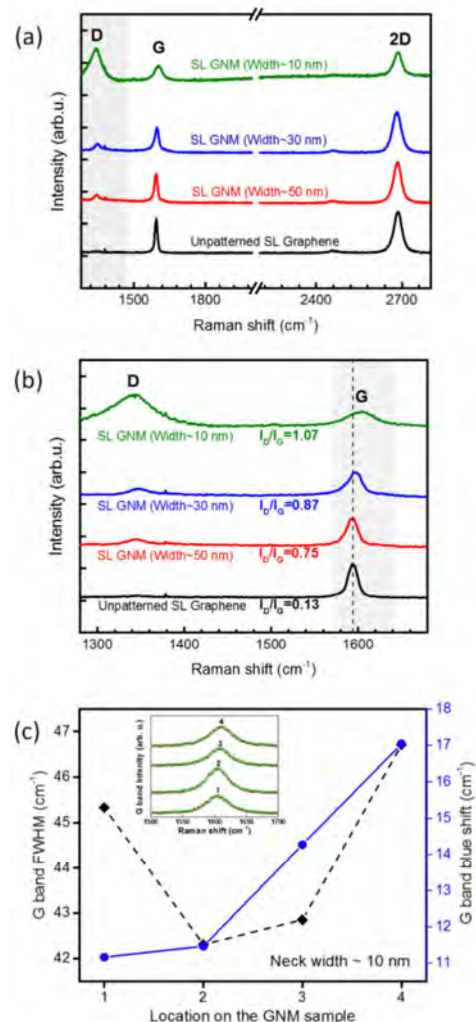

Figure 59. Raman Spectra of single-layer CVD GNM. (a) Raman spectra of the GNM films with different neck widths compared to pristine single-layer graphene spectrum. The spectra were offset for clarity. (b) Close-up view of the spectra showing the G and D bands for the mesh structures compared to the pristine graphene sheet. (c) Inset: G-band peaks acquired from four Raman scans on four different locations on the narrowest GNM sample. The intensity bands are fitted using Gaussian functions. The FWHM and blue shift of the G bands of the Raman spectra acquired from four different locations on the narrowest GNM sample. The G band FWHM is referred to as the left axis while the G band blue shift is referred to as the right axis. Inset shows the G band intensity of the spectra for those four locations.

In order to study the transport characteristics of the GNM, a field-effect transistor (Supplementary Information) with the mesh structure serving as the conduction channel was fabricated. Due to its 2D nature, the drive current of graphene devices, can be scaled up by increasing the device area. This is of great significance for realizing high-frequency devices with sufficiently high drive current in large circuits[120]. Since our IL technique enables the fabrication of GNMs over of an area, the channel length and width of the transistor are chosen to be 14 and 2 mm, respectively. Figure 60a shows a schematic representation of the GNM-FET. Plots of source-drain current (I_d) as a function of gate voltage (V_g) at a constant source-drain voltage (V_{ds}) are shown in Figure 60b. The SL GNM-device delivered ~3.9 μA/μm current with an ON/OFF current ratio of ~9 at = -1V. This is due mainly to a large GNM conduction channel filled with high density graphene ribbons capable of driving high currents. Importantly, at V_{ds} = -100 mV, although the ON-state current density is reduced to ~2.5 μA/μm, the ON/OFF current ratio has increased up to ~35. The modulation of the ON/OFF current ratio by varying the source-drain voltage is characteristic of the GNM as it is not been reported for pristine graphene devices[121]. The measured dependence of the ON/OFF current ratio on V_{ds} indicates the semiconducting nature of the GNM. This behavior is attributed to the formation of an electronic bandgap in graphene as a result of quantum confinement, edge and localization effects[122]. The latter also suggests that the blue shift and broadening in the G band for the narrowest mesh is likely due to confinement and localization effects. Multiple minor conduction plateaus are found in the transfer curves (Figure 60b), possibly due to the formation of electronic subbands in the GNM. Therfore, the GNM transistor (Figure 60c) is non-linear, regardless of the applied gate voltage. In addition, although Fermi-level modulation by the gate voltage is present, no saturation regions of the curves are observed. The ON-state current of the GNM-FET is approximately 9 orders of magnitude lower than the one measured for an unpatterned graphene device (Figure 60d). The ON current obtained from the GNM-FET is comparable to the results obtained for few-layer GNM-FETs[123], and it is considerably higher than reported GNR-FETs with similar width[124,125]. Moreover, the gate voltage sweeping range in the GNM-device is found to be smaller than that of the unpatterned graphene device. This might be due to the increased leakage through the gate oxide after patterning. The reduced level of current compared to the bulk device comes from the limited current pathway and the introduction of edge defects. The comparison (Figure 60d) also shows that the charge neutrality point for the GNM is shifted toward higher positive gate voltage regions. This phenomenon is attributed to the absorption of charged impurities at the edge terminations induced by oxidation during the plasma treatment and polymer residues[126]. Despite the fact that absorption of charged impurities by edge terminations in the GNM in principle plays a role in doping of the structure, it's impact on the semiconductor behavior of the GNM (i.e. bandgap, ON/OFF ratio, etc.) could be affected by many different factors[127]. Such factors

DISTRIBUTION A: Distribution approved for public release.

may include the type of doping, the position of the dopant with respect to the ribbon edges, the ribbon width, and type of ribbon symmetry (i.e. zigzag and armchair edges). Isolating these various effects would require further systematic investigations. The electronic properties of GNM made by IL along with neck-width and sheet coverage area are compared with previously reported results in Table 1.

Table 5.Comparison of dimensions and electronic properties of GNMs fabricated by different techniques.

Properties	Fabrication Technique						
	Block Copolymer Litho[20]	Block Copolymer Litho[21]	Nano Imprint Litho[36]	Aluminum Oxide Templating[37]	Nano-Sphere Litho[57]	Nano-Sphere Litho[58]	Interferometric Litho[*]
Graphene type	SL[*]/ML[ϒ]	SL	SL	SL	N.R[Ŧ]	SL	SL
Sheet Coverage (μm^2)	N.R	1E6	4	N.R	N.R	N.R	1E8
Min Neck width (nm)	5	18	7	15	20	65	10
ON/OFF Ratio[ǂ]	100	39	80	10	10	2	35
Mobility[ǂ] (cm^2V.S)	N.R	>1	1000	N.R	N.R	31	80
Band gap[ǂ] (meV)	100	102	N.R	N.R	N.R	0	30
Channel width (µm)	3	N.R	2	5.8	1.5	1	2
Channel Length (µm)	2.3	N.R	2	2	20	2	2000

[*]Single Layer graphene, [ϒ]Multilayer/Few Layer graphene, [ǂ]At room temperature. Note that the ON/OFF current ratio is a function of source-drain voltage (), and to obtain a reasonable comparison, one should look at the ratios at the same, [Ŧ]Not reported

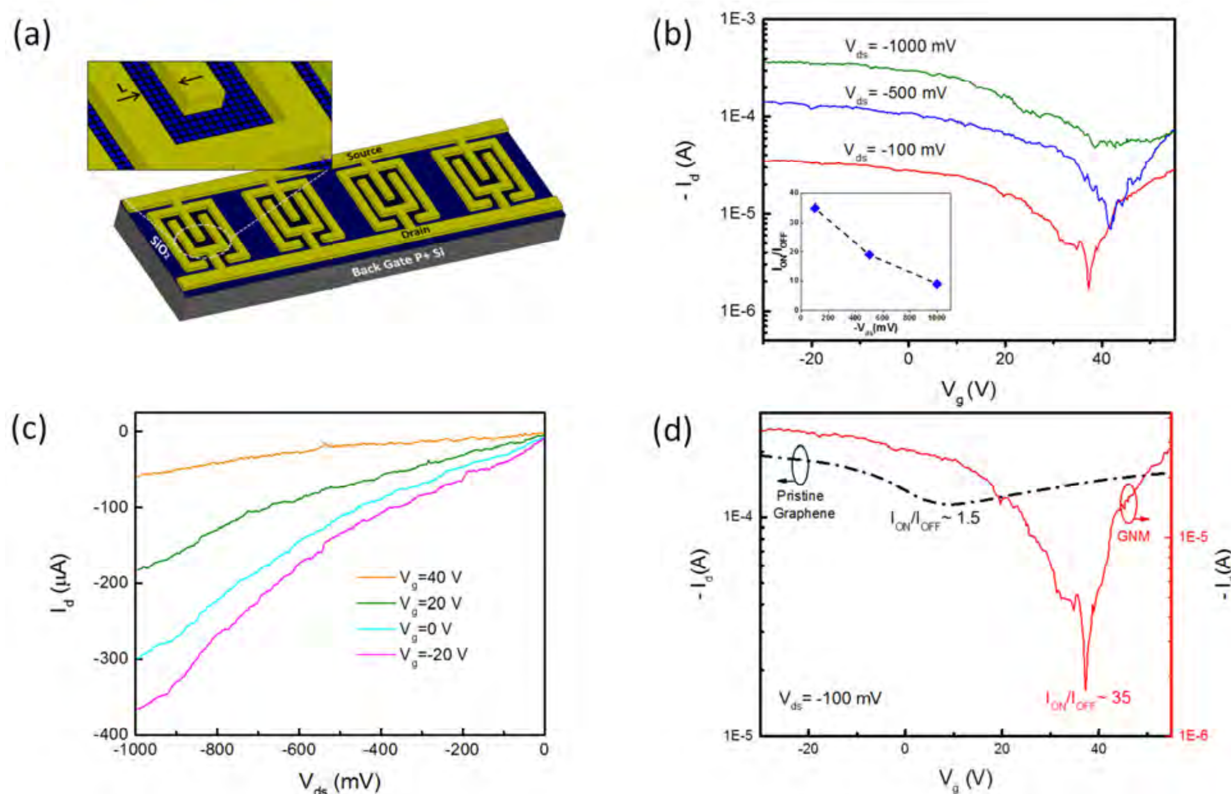

Figure 60. Transfer characteristics of graphene nanomesh. (a) A schematic representation of the GNM-FET. The graphene mesh structure with average neck width of ~10 nm was fabricated on heavily doped silicon substrate with 285 nm-thick layer as the gate dielectric. The channel length L and width W of the GNM-device are 14 µm and 2 mm, respectively. (b) versus gate voltage (V_g) recorded at different source-drain voltages obtained at room

DISTRIBUTION A: Distribution approved for public release.

temperature. (c) Source-drain current (I_d) versus source-drain voltage (V_{ds}) recorded at different gate voltages acquired at room temperature. (d) Comparison of for bulk (dashed black curve) and GNM-devices (solid red curve) at =-1 mV at room temperature. The current for bulk graphene-device is referred to as the left axis while the current for GNM-device is referred to as the right axis.

The overall current of the GNM displayed a significant temperature dependence (Figure 61a), where back-gate modulation at increased from ~9 at room temperature to ~215 at 77 K. The ON/OFF current ratio of a FET-device exponentially scales with the bandgap as $I_{ON}/I_{OFF} \propto exp(-E_g/k_BT)$, where is Boltzmann constant and T is the absolute temperature[128]. We speculate that, at very low temperatures, carriers did not have sufficient energy ($k_BT \ll E_g$), to tunnel through the gap or hop through edge states and therefore the OFF-current state drops markedly. This temperature dependence is in strong contrast to that observed in unpatterned graphene FETs, where the pristine graphene is semi-metallic with a zero bandgap, and the temperature dependence of the transfer curves was negligible. Moreover, we noticed that the current plateau features are more pronounced at lower temperatures. The plateau structures are highly reproducible under different thermal cycles, and they generally become more well-defined as the temperature becomes lower than 120 K. The former change in the plateau peaks is attributed to either stronger charge hopping through a series of quantum dots or to conduction associated with multiple one dimensional (1D) subbands generated in the mesh structure at lower temperatures.

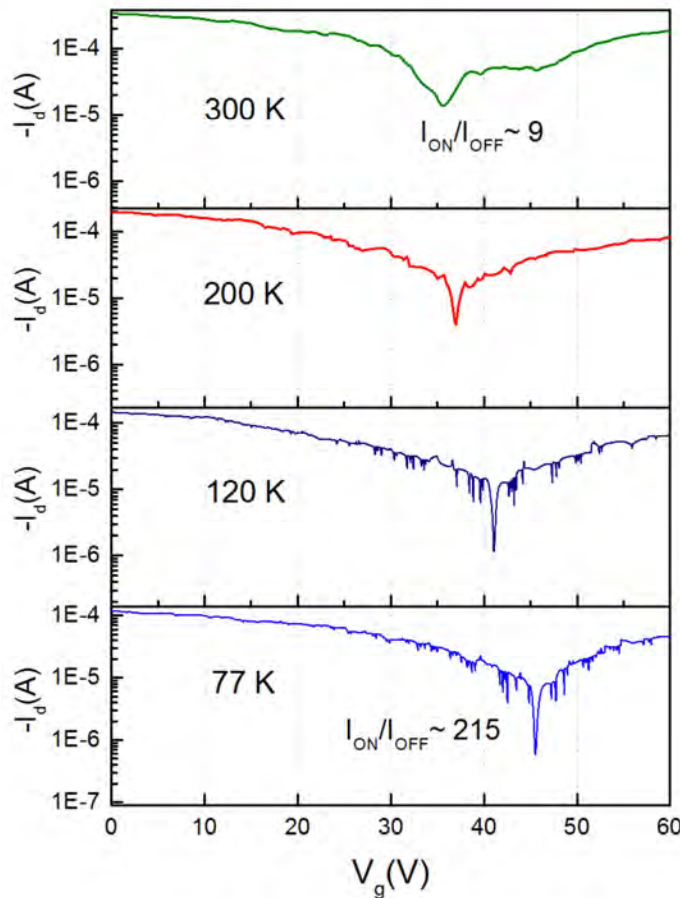

Figure 61. Temperature study of GNM transfer characteristics. Comparison of curves of the GNM-FET with ~ 10 nm neck width recorded at = -1 V and at different temperatures 300, 200, 120, and 77 K.

The hole effective carrier mobilities in the SL-GNM produced by IL are estimated to be ~80 and ~165 at room temperature and 77 K, respectively. The charge carrier mobility in GNM is limited by intrinsic scattering, phonon scattering from the supporting substrate, impurity scattering, and line edge roughness (LER) scattering[129]. The relative importance of these scattering mechanisms varies with the temperature, Fermi-level location, and the neck width of the graphene mesh[130]. Therefore, the observed increase in the hole carrier mobility of the GNM, suggests that the net scattering mechanism is less effective at lower temperatures. These calculated values are relatively higher than reported carrier mobilities for single and few layer GNMs with the same average neck width (Table 5). The electronic bandgap of GNMs inversely scales with the average neck width ($E_g \sim a/w$) by the experimentally derived equation , where is between 0.3 and 1.5 with unit [nm eV][131]. Also the ON/OFF current ratio of GNM-FETs varies exponentially with the bandgap, as specified by the following equation 1:

$$I_{ON}/I_{OFF} \propto exp(-E_g/k_BT) \qquad (1)$$

DISTRIBUTION A: Distribution approved for public release.

Using the measured ON/OFF current ratio at various temperature and inverting Eq. 1 to calculate the bandgap, we estimate for a GNM with an average neck width of ~10 nm. As shown in Table 5, this value is in the range of those previously reported in the literature for a GNM comparable ribbons width.

In summary, we have proposed and demonstrated a simple yet effective approach to produce highly uniform graphene nanomesh structures with sub-10 nm neck width across areas. The fabrication of GNM based on IL is scalable and can be performed using standard top-down fabrication methods. The resulting GNM exhibit a semiconducting behavior with an estimated bandgap ~30 meV. GNMs with various neck widths in the range of 50-10 nm have been fabricated on a macroscopic scale with an unprecedented level of control. Raman studies have shown a significant broadening and blue shift of the G band for the narrowest GNM. Such blue shift is attributed to quantum confinement effects. The GNM devices have been fabricated and they have shown drive currents ~3.9 μA/μm, ON/OFF current ratios ~35 at room temperature and ~215 at 77 K, and mobilities suitable for field-effective devices operating at room temperature. The availability of direct bandgap GNMs over large areas provides exciting opportunities for graphene-based photodetectors[132] and highly interconnected graphene networks[133]. Further narrowing of the GNM neck width is indeed possible and requires optimization on the etching parameters (i.e. gas pressure, RF power, etc.) to provide a finer control over transition from 10 nm neck width to 5 nm. Additionally, state of the art techniques such as scanning transmission electron microscopy (STEM) or AFM with carbon nanotube (CNT) tip will offer a more precise characterization for narrower mesh structures. IL parameters could also be used as additional variables in the GNM fabrication. Specifically, the laser wavelength and incident angle could be adjusted to make a structure with smaller periodicities, which in turn improves the drive current of the GNM-device.

4.0 Papers published with the support of this grant

Plis, E. InAs/GaSb Type-II Superlattice Detectors. Advances in Electronics 2014 (2014) DOI/10.1155/2014/246769

E. Plis, B. Klein, S. Myers, N. Gautam, E. P. Smith, and S. Krishna, “High Operating Temperature Midwave Infrared InAs / GaSb Superlattice Photodetectors,” *IEEE Electron Device Lett.*, vol. 34, no. 3, pp. 426–428, 2013.

Plis, E., Klein, B., Myers, S., Gautam, N., and Krishna, S.: (111) InAs/GaSb type-II strained layer superlattice material for high operating temperature detection, physica status solidi c 10, 748 (2013)

Fang, H., Bechteld, H. A., Plis, E., Martin, M. C., Krishna, S., Yablonovitch, E., Javey, A. Quantum of optical absorption in two-dimensional semiconductors. Proceedings of the National Academy of Sciences of the United States of America 110, p. 11688 (2013)

Takei, K., Kapadia, R., Li, Y., Plis, E., Krishna, S., Javey, A. Surface Charge Transfer Doping of IIIV Nanostructures. The Journal of Physical Chemistry C 117, p. 17845 (2013)

Gautam, N., Myers, S.,Barve, A. V., Klein, B., Smith, E. P., Rhiger, D., Plis, E., Kutty, M. N., Henry, N., Schuler-Sandy, T., Krishna, S.: Band engineered HOT midwave infrared detectors based on type-II InAs/GaSb strained layer superlattices, Infrared Physics and Technology 59, p. 72 (2013)

Asplund, C., Marcks von Wrtemberg, R.,Lantz, D., Malm, H., Martijn, H., Andersson, J., Plis, E., Gautam, N., and Krishna, S.: Performance of mid-wave T2SL detectors with heterojunction barriers, Infrared Physics and Technology (2013)

Plis, E., Naydenkov, M., Myers, S., Klein, B., Gautam, N., Krishna, S. S., Smith, E. P., Johnson, S., and Krishna, S.: Dual-band pBp detectors based on InAs/GaSb strained layer superlattices, Infrared Physics and Technology (2013)

Karim, A., Marcks von Wrtemberg, R., Asplund, C., Malm, H., Andersson, J., Plis, E., and Krishna, S.: Characterization of InAs/GaSb type-II superlattice photodiodes for mid-wave IR with different mesa sidewall passivation schemes, physica status solidi (c) 9, p. 1690 (2012)

Nah, J., Fang, H., Wang, C.,Takei, K., Lee, M. H., Plis, E., Krishna, S., and Javey, A.: IIIV Complementary metal-oxide-semiconductor electronics on silicon substrates, Nano Letters 12, p. 3592 (2012)

DISTRIBUTION A: Distribution approved for public release.

Wang, C., Chien, J.-C., Fang, H., Takei, K., Nah, J., Plis, E., Krishna, S., Niknejad, A. M., and Javey, A.: Self-aligned, extremely high frequency IIIV metal-oxide-semiconductor field-effect transistors on rigid and flexible substrates, Nano Letters 12, p. 4140 (2012)

N. Gautam, S. Myers, A. V. Barve, B. Klein, E. P. Smith, D. R. Rhiger, L. R. Dawson, and S. Krishna, "High operating temperature interband cascade midwave infrared detector based on type-II InAs/GaSb strained layer superlattice", Appl. Phys. Lett. 101, 021106 (2012)

H. Fang, S. Chuang, K. Takei, H. S. Kim, E. Plis, C.-H. Liu, S. Krishna, Y.-L. Chueh, and A. Javey, "Ultrathin-Body High-Mobility InAsSb-on-Insulator Field-Effect Transistors", IEEE Electron Device Lett. 33(4), 2012

E. A. Plis, M. N. Kutty, and S. Krishna, "Passivation techniques for InAs/GaSb strained layer superlattice detectors", Laser Photonics Rev., 1–15 (2012)

K. Takei, S. Chuang, H. Fang, R. Kapadia, C.-H. Liu, J. Nah, H. S. Kim, E. Plis, S. Krishna, Y.-L. Chueh, and A. Javey "Benchmarking the performance of ultrathin body InAs-on-insulator transistors as a function of body thickness ", Appl. Phys. Lett. 99, 103507 (2011)

S. J. Lee, Z. Ku, A. Barve, J. Montoya, W.-Y. Jang, S.R.J. Brueck, M. Sundaram, A. Reisinger, S. Krishna, and S. K. Noh, "A monolithically integrated plasmonic infrared quantum dot camera", Nature Communications 2, 286 (2011)

N. Gautam, M. Naydenkov, S. Myers, A. V. Barve, E. Plis, T. Rotter, L. R. Dawson, and S. Krishna, "Three color infrared detector using InAs/GaSb superlattices with unipolar barriers", Appl. Phys. Lett. 98, 121106 (2011)

B Klein, E Plis, M N Kutty, N Gautam, A Albrecht, S Myers and S Krishna, "Varshni parameters for InAs/GaSb strained layer superlattice infrared photodetectors", J. Phys. D: Appl. Phys. 44, 075102(2011)

E. Plis, M.N. Kutty, S. Myers, H.S. Kim, N. Gautam, L.R. Dawson, S. Krishna, "Passivation of Long-wave Infrared InAs/GaSb Strained Layer Superlattice detectors", Infrared Physics & Technology 54, 252 (2011)

H. Ko, K. Takei, R. Kapadia, S. Chuang, H. Fang, P. W. Leu, K. Ganapathi, E. Plis, H. S. Kim, S.Y. Chen, M. Madsen, A. C. Ford, Y.-L. Chueh, S. Krishna, S. Salahuddin, and A. Javey, "Ultrathin compound semiconductor on insulator layers or high-performance nanoscale transistors", Nature 468 (2010)

Elena Plis, S. Myers, M. N. Kutty, J. Mailfert, E. P. Smith, S. Johnson, and S. Krishna, "Lateral diffusion of minority carriers in InAsSb-based nBn detectors", Appl. Phys. Lett. 97, 123503(2010)

E. A. Plis, M. N. Kutty, S. Myers, A. Rathi, E. H. Aifer, I. Vurgaftman, and S. Krishna, "Performance improvement of long-wave infrared InAs/GaSb strained-layer superlattice detectors through sulfur-based passivation," *Infrared Phys. Technol.*, vol. 55, pp. 216–219, 2012.

M. Zamiri, E. Plis, J. O. Kim, S. C. Lee, A. Neumann, S. Myers, E. P. Smith, A. M. Itsuno, J. G. A. Wehner, S. M. Johnson, S. R. J. Brueck, and S. Krishna, "MWIR superlattice detectors integrated with substrate side-illuminated plasmonic coupler," in *Proc. of SPIE, Infrared Technology and Applications XL*, 2014, vol. 9070, no. 90700Y.

C. M. Watts, D. Shrekenhamer, J. Montoya, G. Lipworth, J. Hunt, T. Sleasman, S. Krishna, D. R. Smith, and W. J. Padilla, "Terahertz compressive imaging with metamaterial spatial light modulators," *Nat. Photonics*, vol. 8, no. 8, pp. 605–609, 2014.

E. A. Plis, S. S. Krishna, N. Gautam, S. Myers, and S. Krishna, "Bias switchable dual-band InAs/GaSb superlattice detector With pBp architecture," *IEEE Photonics J.*, vol. 3, no. 2, pp. 234–240, 2011.

DISTRIBUTION A: Distribution approved for public release.

E. Plis, B. Klein, S. Myers, N. Gautam, T. J. Rotter, R. L. Dawson, S. Krishna, S. J. Lee, and Y. H. Kim, "Type-II InAs/GaSb strained layer superlattices grown on GaSb (111)B substrate," *J. Vac. Sci. Technol. B*, vol. 31, no. 3, p. 03C123, 2013.

T. Schuler-Sandy, S. Myers, B. Klein, N. Gautam, P. Ahirwar, Z.-B. Tian, T. Rotter, G. Balakrishnan, E. Plis, and S. Krishna, "Gallium free type II InAs/InAsxSb1-x superlattice photodetectors," *Appl. Phys. Lett.*, vol. 101, no. 7, p. 071111, Aug. 2012.

B. Klein, N. Gautam, E. Plis, T. Schuler-sandy, T. J. Rotter, S. Krishna, B. Connelly, G. D. Metcalfe, P. Shen, and M. Wraback, "Carrier lifetime studies in midwave infrared type-II InAs / GaSb strained layer superlattice," *J. Vac. Sci. Technol. B*, vol. 32, no. 2, p. 02C101, 2014.

G. A. Umana-Membreno, B. Klein, H. Kala, J. Antoszewski, N. Gautam, M. N. Kutty, E. Plis, S. Krishna, and L. Faraone, "Vertical minority carrier electron transport in p-type InAs/GaSb type-II superlattices," *Appl. Phys. Lett.*, vol. 101, no. 25, p. 253515, 2012.

B. Klein, PhD Thesis, 2014

E. Plis, B. Klein, N. Gautam, S. Myers, M. N. Kutty, M. Naydenkov, S. Krishna. Proc. SPIE 8012, 80120V (2011)

N. Gautam, PhD Thesis, 2012

Z.-B. Tian, S. E. Godoy, H. S. Kim, T. Schuler-Sandy, J. A. Montoya, and S. Krishna. Appl. Phys. Lett. **105**, 051109 (2014)

N. Gautam, H. S. Kim, M. N. Kutty, E. Plis, L. R. Dawson, and S. Krishna, "Performance improvement of longwave infrared photodetector based on type-II InAs/GaSb superlattices using unipolar current blocking layers," *Appl. Phys. Lett.*, vol. 96, no. 231107, p. 231107, 2010.

B. Klein, N. Gautam, S. Myers, and S. Krishna, "Temperature-dependent absorption derivative on InAs/GaSb Type II superlattices," Proc. SPIE, vol. 8353, 2012.

B. Klein et al., Post-etching mesa surface composition investigation of InAs/GaSb type-II strained layer super lattices using XPS characterization, Infrared Phys. Technol. (2014), http://dx.doi.org/10.1016/j.infrared.2014.10.010.

5.0 Bibliographical References

[1] D.L. Smith and C. Mailhiot. J. Appl. Phys. **62**, 2545 (1987)
[2] E. R. Youngdale, J. R. Meyer, C. A. Hoffman, F. J. Bartoli, C. H. Grein, P.M. Young, H. Ehrenreich, R. H. Miles, and D. H. Chow. Appl. Phys. Lett. **64**, 3160 (1994)
[3] M. Razeghi, A. Haddadi, A.M. Hoang, G. Chen, S. Bogdanov, S.R. Darvish, F. Callewaert, P.R. Bijjam, and R. McClintock. J. Electron. Mater. **43** (8), 2802 (2014)
[4] G. Chen, A. Haddadi, A.-M. Hoang, R. Chevallier, and M. Razeghi. Opt. Lett. **40**, 45 (2015)
[5] Z.-B. Tian, S. E. Godoy, H. S. Kim, T. Schuler-Sandy, J. A. Montoya, and S. Krishna. Appl. Phys. Lett. **105**, 051109 (2014)
[6] D. Z. Ting, A. Soibel, S. A. Keo, S. B. Rafol, J. M. Mumolo, J. K. Liu, C. J. Hill, A. Khoshakhlagh, L. Höglund, E. M. Luong, S. D. Gunapala. J. Appl. Remote Sens. **8**, 084998 (2014)
[7] A. Haddadi, S.R. Darvish, G. Chen, A.M. Hoang, B.M. Nguyen and M. Razeghi. AIP Conference Proceedings, **1416**, 56 (2011)
[8] S. D. Gunapala, D. Z. Ting, C. J. Hill, J. Nguyen, A. Soibel, S. B. Rafol, S. A. Keo, J. M. Mumolo, M. C. Lee, J. K. Liu, B. Yang. Photon. Tech. Lett. **22**, 1856 (2010)
[9] E. K.-W. Huang, M.A. Hoang, G. Chen, S. Ramezani-Darvish, A. Haddadi, and M. Razeghi. Opt Lett 37, 4744 (2012)
[10] T. Stadelmann ; A. Wörl ; M. Wauro ; V. Daumer ; J. Niemasz ; W. Luppold ; T. Simon ; M. Riedel ; R. Rehm ; M. Walther. Proc. SPIE **90700V** (2014)

DISTRIBUTION A: Distribution approved for public release.

[11]J. B. Rodriguez, E. Plis, G. Bishop, Y. D. Sharma, H. Kim, L. R. Dawson, and S. Krishna, Appl. Phys. Lett. **91**, 043514 (2007).
[12] B. M. Nguyen, D. Hoffman, P. Y. Delaunay, and M. Razeghi, Appl. Phys. Lett. **91**, 163511 (2007).
[13] I. Vurgaftman, E. H. Aifer, C. L. Canedy, J. G. Tischler, J. R. Meyer, J. H. Warner, E. M. Jackson, G. Hildebrandt, and G. J. Sullivan, Appl. Phys. Lett. **89**, 121114 (2006).
[14] D. Z.-Y. Ting, C. J. Hill, A. Soibel, S. A. Keo, J. M. Mumolo, J. Nguyen, and S. D. Gunapala, Appl. Phys. Lett. **95**, 023508 (2009).
[15] N. Gautam, H., H. S. Kim, M. N. Kutty, E. Plis, L. R. Dawson, S. Krishna. Appl. Phys. Lett. **96**, 231107 (2010)
[16]O. Salihoglu, A. Muti, K. Kutluer, T. Tansel, R. Turan, Y. Ergun, A. Aydinli. Appl. Phys. Lett. **101**, 073505–1 (2012)
[17]P. Martyniuk, A. Rogalski. Infrared. Phys. Technol. (2014) http://dx.doi.org/10.1016/j.infrared.2014.09.026
[18] G. Ariyawansa, E. Steenbergen, L. J. Bissell, J. M. Duran, J. E. Scheihing, M. T. Eismann. Proc. SPIE **9070**, 90701J (2014)
[19] N. Gautam, H. S. Kim, M. N. Kutty, E. Plis, L. R. Dawson, S. Krishna. Appl. Phys. Lett. **96,** 231107, 2010
[20] J. B. Rodriguez, E. Plis, G. Bishop, Y. D. Sharma, H. Kim, L. R. Dawson, and S. Krishna, Appl. Phys. Lett. **91**, 043514 (2007).
[21] B. M. Nguyen, D. Hoffman, P. Y. Delaunay, and M. Razeghi, Appl. Phys. Lett. **91**, 163511 (2007).
[22] I. Vurgaftman, E. H. Aifer, C. L. Canedy, J. G. Tischler, J. R. Meyer, J. H. Warner, E. M. Jackson, G. Hildebrandt, and G. J. Sullivan, Appl. Phys. Lett. **89**, 121114 (2006).
[23] O. Salihoglu, A. Muti, K. Kutluer, T. Tansel, R. Turan, Y. Ergun, A. Aydinli. Appl. Phys. Lett. **101**, 073505–1 (2012)
[24] D. Z.-Y. Ting, C. J. Hill, A. Soibel, S. A. Keo, J. M. Mumolo, J. Nguyen, and S. D. Gunapala, Appl. Phys. Lett. **95**, 023508 (2009).
[25] P. Christol, C. Cervera, R. Chaghi, H. Ait-Kaci, J. B. Rodriguez, L. Konczewicz, S. Contreras, K. Jaworowicz, I. Ribet-Mohamed. Proc. SPIE 7608, 76081U (2010)
[26] B. Klein, J. Montoya, N. Gautam, S. Krishna. Applied Physics A 111(2) (2012)
[27] D. R. Rhiger. J. Electron. Mater. 40 (8), 1815 (2011) and references therein.
[28] E.A. Plis. Mid-IR type-II InAs/GaSb nanoscale supperlattice sensors, in: Department of Electrical and Computer Engineering, University of New Mexico, Albuquerque, 2007.
[29] J. B. Rodriguez, E. Plis, G. Bishop, Y. D. Sharma, H. Kim, L. R. Dawson, S. Krishna. Appl. Phys. Lett. 91, 043514 (2008).
[30] Khoshakhlagh, E. Plis, S. Myers, Y. Sharma, L.R. Dawson, S. Krishna. J. Cryst. Growth 311, 1901 (2009)
[31] E. Plis, B. Klein, N. Gautam, S. Myers, M. N. Kutty, M. Naydenkov, S. Krishna. Proc. SPIE 8012, 80120V (2011)
[32] B. C. Connelly, G. D. Metcalfe, H. Shen, M. Wraback, C. L. Canedy, I. Vurgaftman, J. S. Melinger, C. A. Affouda, E. M. Jackson, J. A. Nolde, J. R. Meyer, and E. H. Aifer, "Investigation of Trap States in Mid-Wavelength Infrared Type II Superlattices Using Time-Resolved Photoluminescence," *J. Electron. Mater.*, vol. 42, no. 11, pp. 3203–3210, Sep. 2013.
[33] M.-C. Wu and C.-C. Chen, "Photoluminescence of high-quality GaSb grown from Ga- and Sb-rich solutions by liquid-phase epitaxy," *J. Appl. Phys.*, vol. 72, no. 9, p. 4275, 1992.
[34] E. Kuramochi, N. Kondo, Y. Takanashi, and M. Fujimoto, "Observation of deep levels in undoped GaSb grown by molecular beam epitaxy," *Appl. Phys. Lett.*, vol. 63, no. 19, p. 2664, 1993.
[35] J. W. McClure, "Field Dependence of Magnetoconductivity," *Phys. Rev.*, vol. 101, no. 6, pp. 1642–1646, 1956.
[36] I. Vurgaftman, J. R. Meyer, C. A. Hoffman, D. Redfern, J. Antoszewski, L. Faraone, and J. R. Lindemuth, "Improved quantitative mobility spectrum analysis for Hall characterization," *J. Appl. Phys.*, vol. 84, no. 9, pp. 4966–4973, 1998.
[37] G. A. Umana-Membreno, B. Klein, H. Kala, J. Antoszewski, N. Gautam, M. N. Kutty, E. Plis, S. Krishna, and L. Faraone, "Vertical minority carrier electron transport in p-type InAs/GaSb type-II superlattices," *Appl. Phys. Lett.*, vol. 101, no. 25, p. 253515, 2012.
[38]B. Klein, N. Gautam, E. Plis, T. Schuler-Sandy, T. J. Rotter, S. Krishna, B. C. Connely, G. D. Metcalfe, P. Shen, M. Wraback. J. Vac. Sci. Technol. B **32**, 02C101 (2014)
[39] A. Rogalski, K. Adamiec, J. Rutkowski. Narrow-gap semiconductor photodiodes. SPIE Press monograph. P. 86 (2000)
[40] W. Walukiewicz. Proc. Mat. Res. Soc. Symp. 148, 137 (1989)
[41] S. P. Svensson, D. Donetsky. D. Wang, H. Hier, F. J. Crowne, G. Belenky. J. Cryst. Growth. 334, 103 (2011)

DISTRIBUTION A: Distribution approved for public release.

[42] G. Belenky, G. Kipshidze, D. Donetsky, S. P. Svensson, W. L. Sarney, H. Hier, L. Shterengas, D. Wang, Y. Lin. Proc. of SPIE, 8012, 80120W-1 (2011)
[43] G. C. Dente, M. L. Tilton, J. Appl. Phys. 86, 1420 (1999)
[44] D. R. Rhiger. J. Electron. Mater. 40, 1815 (2011)
[45] H. Kroemer. Physica E **20**, 196 (2004)
[46] R. Tsu, L. Esaki, B.A. Sai-Halasz. Appl. Phys. Lett. **30,** 651 (1977).
[47] D.L. Smith, C. Mailhiot. J. Appl. Phys. **62**, 2545 (1987)
[48] F. Szmulowicz., G. Brown. Proc. SPIE **6900**, 69000L-1, (2008)
[49] G.P. Schwartz, G.J. Gualtieri, W.A. Sunder. J. Cryst. Growth. **102**, 147 (1990)
[50] Y. Wei, A. Hood, H. Yau, A. Gin, M. Razeghi, M. Z. Tidrow, V. Nathan. Appl. Phys. Lett. **86**, 233106 (2005)
[51] C. Cervera, I. Ribet-Mohamed, R. Taalat, J.P. Perez, P. Christol, J.B. Rodriguez. J. Electron. Mater. DOI: 10.1007/s11664-012-2035-4 (2012)
[52] J. B. Rodriguez, E. Plis, G. Bishop, Y. D. Sharma, H. Kim, L. R. Dawson, S. Krishna. Appl. Phys. Lett. **91**, 043514 (2007)
[53] J. V. Li, C. J. Hill, J. Mumolo, S. Gunapala, S. Mou, S.-L. Chuang. Appl. Phys. Lett. **93**, 163505 (2008)
[54] Y. Wei, A. Hood, H. Yau, A. Gin, M. Razeghi, M. Z. Tidrow, V. Nathan. Appl. Phys. Lett. 86, 233106 (2005)
[55] J. V. Li, C. J. Hill, J. Mumolo, S. Gunapala, S. Mou, S.-L. Chuang. Appl. Phys. Lett. **93**, 163505 (2008)
[56] J. B. Rodriguez, E. Plis, G. Bishop, Y. D. Sharma, H. Kim, L. R. Dawson, S. Krishna. Appl. Phys. Lett. 91, 043514 (2007)
[57] S. J. Lee1, Z. Ku, A. Barve, J. Montoya, W.-Y. Jang, S.R.J. Brueck, M. Sundaram, A. Reisinger, S. Krishna, and S. K. Noh. Nature Communications 2, 286 (2011)
[58] N. Gautam, M. Naydenkov, S. Myers, A. V. Barve, E. Plis, T. Rotter, L. R. Dawson, S. Krishna. Appl. Phys. Lett. 98, 121106 (2011)
[59] R. Rehm, M. Walther, J. Fleissner, J. Schmitz, J. Ziegler, W. Cabanski, R. Breiter. Orlando (Kissimmee), FL, USA, 2006 (unpublished).
[60] E. Plis, S. S. Krishna, E. P. Smith, S. Johnson, and S. Krishna. Electron. Lett. **47**, 133 (2011)
[61] E. A. Plis, S. S. Krishna, N. Gautam, S. Myers, S. Krishna. IEEE Photonics J. **3**, 234 (2011)
[62] M. Zamiri, E. Plis, J. O. Kim, S. C. Lee, A. Neumann, S. Myers, and S. Krishna. Proc SPIE 90700, 9700Y (2014)
[63] E. Plis, M. N. Kutty, S. Myers, H. S. Kim, N. Gautam, L. R. Dawson, and S. Krishna, Inf. Phys. Technol. 54, 252 (2010).
[64] K. Banerjee, S. Ghosh, S. Mallick, E. Plis, S. Krishna. J Electron. Mater. **38**, 1944 (2009)
[65] A. Hood, Y.Wei, A. Gin, M. Razeghi, M. Z. Tidrow, V. Nathan. Proc. of SPIE **5732**, 316 (2005)
[66] Geim, A. K. & Novoselov, K. S. The rise of graphene. Nat. Mater. 6, 183-191 (2007).
[67] Xu, Y., Bai, H., Lu, G., Li, C. & Shi, G. Flexible graphene films via the filtration of water-soluble noncovalent functionalized graphene sheets. J. Am. Chem. Soc. 130, 5856-5857 (2008).

[68] Kim, K. S. et al. Large-scale pattern growth of graphene films for stretchable transparent electrodes. Nature 457, 706-710 (2009).
[69] Rafiee, M. A. et al. Enhanced mechanical properties of nanocomposites at low graphene content. ACS nano 3, 3884-3890 (2009).
[70] Schwierz, F. Graphene transistors. Nat. Nanotechnol. 5, 487-496 (2010).
[71] Vaziri, S. et al. A graphene-based hot electron transistor. Nano Lett. 13, 1435-1439 (2013).
[72] Eda, G. & Chhowalla, M. Chemically Derived Graphene Oxide: Towards Large-Area Thin-Film Electronics and Optoelectronics. Adv. Mater. 22, 2392-2415 (2010).
[73] Bonaccorso, F., Sun, Z., Hasan, T. & Ferrari, A. Graphene photonics and optoelectronics. Nat. Photon. 4, 611-622 (2010).

[74] Shao, Y. et al. Graphene based electrochemical sensors and biosensors: a review. Electroanalysis 22, 1027-1036 (2010).
[75] Lu, C. H., Yang, H. H., Zhu, C. L., Chen, X. & Chen, G. N. A graphene platform for sensing biomolecules. Angew. Chem. 121, 4879-4881 (2009).
[76] Son, Y.-W., Cohen, M. L. & Louie, S. G. Energy gaps in graphene nanoribbons. Phys. Rev. Lett. 97, 216803 (2006).
[77] Zhou, S. et al. Substrate-induced bandgap opening in epitaxial graphene. Nat. Mater. 6, 770-775 (2007).

DISTRIBUTION A: Distribution approved for public release.

[78] Hicks, J. et al. A wide-bandgap metal-semiconductor-metal nanostructure made entirely from graphene. Nat. Phys. 9, 49-54 (2013).
[79] Choi, S.-M., Jhi, S.-H. & Son, Y.-W. Effects of strain on electronic properties of graphene. Phys. Rev. B. 81, 081407 (2010).
[80] Lusk, M. T. & Carr, L. D. Nanoengineering defect structures on graphene. Phys. Rev. Lett. 100, 175503 (2008).
[81] Lahiri, J., Lin, Y., Bozkurt, P., Oleynik, I. I. & Batzill, M. An extended defect in graphene as a metallic wire. Nat. Nanotechnol. 5, 326-329 (2010).
[82] Balog, R. et al. Bandgap opening in graphene induced by patterned hydrogen adsorption. Nat. Mater. 9, 315-319 (2010).
[83] Ci, L. et al. Atomic layers of hybridized boron nitride and graphene domains. Nat. Mater. 9, 430-435 (2010).
[84] Dvorak, M., Oswald, W. & Wu, Z. Bandgap opening by patterning graphene. Sci. Rep. 3, 2289; DOI:10.1038/srep02289 (2013).
[85] Bai, J., Zhong, X., Jiang, S., Huang, Y. & Duan, X. Graphene nanomesh. Nat. Nanotechnol. 5, 190-194 (2010).
[86] Kim, M., Safron, N. S., Han, E., Arnold, M. S. & Gopalan, P. Fabrication and characterization of large-area, semiconducting nanoperforated graphene materials. Nano Lett. 10, 1125-1131 (2010).
[87] Li, X., Wang, X., Zhang, L., Lee, S. & Dai, H. Chemically derived, ultrasmooth graphene nanoribbon semiconductors. Science 319, 1229-1232 (2008).
[88] Barone, V., Hod, O. & Scuseria, G. E. Electronic structure and stability of semiconducting graphene nanoribbons. Nano Lett. 6, 2748-2754 (2006).
[89] Akhavan, O. Graphene nanomesh by ZnO nanorod photocatalysts. Acs Nano 4, 4174-4180 (2010).
[90] Paul, R. K., Badhulika, S., Saucedo, N. M. & Mulchandani, A. Graphene nanomesh as highly sensitive chemiresistor gas sensor. Anal. Chem. 84, 8171-8178 (2012).
[91] Yu, Young-Jun, and Choon Gi Choi. "Graphene nanoribbon sensor." U.S. Patent 13/797,703. 2013 March 12.
[92] Kato, T. et al. High-efficiency graphene nanomesh magnets realized by controlling mono-hydrogenation of pore edges. Appl. Phys. Lett. 104, 252410 (2014).
[93] Yang, H.-X., Chshiev, M., Boukhvalov, D. W., Waintal, X. & Roche, S. Inducing and optimizing magnetism in graphene nanomeshes. Phys. Rev. B. 84, 214404 (2011).
[94] Ning, G. et al. Gram-scale synthesis of nanomesh graphene with high surface area and its application in supercapacitor electrodes. Chem. Commun. 47, 5976-5978 (2011).
[95] Pumera, M. Graphene-based nanomaterials for energy storage. Energy & Environmental Science 4, 668-674 (2011).
[96] Huang, X. et al. Graphene-Based Materials: Synthesis, Characterization, Properties, and Applications. small 7, 1876-1902 (2011).
[97] Fan, Z. et al. Easy synthesis of porous graphene nanosheets and their use in supercapacitors. Carbon 50, 1699-1703 (2012).
[98] Nelson, T., Zhang, B. & Prezhdo, O. V. Detection of nucleic acids with graphene nanopores: ab initio characterization of a novel sequencing device. Nano Lett. 10, 3237-3242 (2010).
[99] Duan, X. Assembled semiconductor nanowire thin films for high-performance flexible macroelectronics. MRS bulletin 32, 134-141 (2007).
[100] Lu, W. & Lieber, C. M. Nanoelectronics from the bottom up. Nat. Mater. 6, 841-850 (2007).
[101] Liang, X. et al. Formation of bandgap and subbands in graphene nanomeshes with sub-10 nm ribbon width fabricated via nanoimprint lithography. Nano Lett. 10, 2454-2460 (2010).
[102] Zeng, Z. et al. Fabrication of graphene nanomesh by using an anodic aluminum oxide membrane as a template. Adv. Mater. 24, 4138-4142 (2012).
[103] Brueck, Steven RJ, and Saleem H. Zaidi. "Method and apparatus for alignment and overlay of submicron lithographic features." U.S. Patent No. 5,216,257. 1993 Jun 1.
[104] Brueck, Steven RJ, and Saleem H. Zaidi. "Method and apparatus for alignment of submicron lithographic features." U.S. Patent No. 5,343,292. 1994 August 30.
[105] Brueck, Steven RJ, Saleem Zaidi, and An-Shyang Chu. "Method for fine-line interferometric lithography." U.S. Patent No. 5,415,835. 1995 May 16.
[106] Brueck, Steven RJ, and Saleem H. Zaidi. "Obtaining a pattern whose fourier transform contains high spatial frequencies, by combining nonlinear functions of intensity of two exposures combined with one nonlinear processing step intermediate between the two exposures." U.S. Patent No. 6,042,998. 2000 March 28.
[107] Brueck, Steven RJ, et al. "Methods and apparatus for integrating optical and interferometric lithography to produce complex patterns." U.S. Patent No. 6,233,044. 2001 May 15.

DISTRIBUTION A: Distribution approved for public release.

[108] Brueck, S. Optical and interferometric lithography-Nanotechnology enablers. Proceedings of the IEEE 93, 1704-1721 (2005).
[109] Kazemi, A. et al. in SPIE NanoScience+ Engineering. 91680B-91680B-91689 International Society for Optics and Photonics (2014).
[110] Vaziri, S. et al. A manufacturable process integration approach for graphene devices. Solid-State Electron. 84, 185-190 (2013).
[111] Suk, J. W. et al. Enhancement of the electrical properties of graphene grown by chemical vapor deposition via controlling the effects of polymer residue. Nano Lett. 13, 1462-1467 (2013).
[112] Pirkle, A. et al. The effect of chemical residues on the physical and electrical properties of chemical vapor deposited graphene transferred to SiO2. Appl. Phys. Lett. 99, 122108 (2011).
[113] Ferrari, A. C. Raman spectroscopy of graphene and graphite: disorder, electron–phonon coupling, doping and nonadiabatic effects. Solid State Commun. 143, 47-57 (2007).
[114] Gupta, A. K., Russin, T. J., Gutiérrez, H. R. & Eklund, P. C. Probing graphene edges via Raman scattering. Acs Nano 3, 45-52 (2008).
[115] Gillen, R., Mohr, M., Thomsen, C. & Maultzsch, J. Vibrational properties of graphene nanoribbons by first-principles calculations. Phys. Rev. B. 80, 155418 (2009).
[116] Kudin, K. N. Zigzag graphene nanoribbons with saturated edges. ACS nano 2, 516-522 (2008).
[117] Zhou, J. & Dong, J. Vibrational property and Raman spectrum of carbon nanoribbon. Appl. Phys. Lett. 91, 173108 (2007).
[118] Paredes, J., Martinez-Alonso, A. & Tascon, J. Multiscale imaging and tip-scratch studies reveal insight into the plasma oxidation of graphite. Langmuir 23, 8932-8943 (2007).
[119] Liu, L. et al. Graphene oxidation: thickness-dependent etching and strong chemical doping. Nano Lett. 8, 1965-1970 (2008).
[120] Lin, Y.-M. et al. Operation of graphene transistors at gigahertz frequencies. Nano Lett. 9, 422-426 (2008).
[121] Lemme, M. C., Echtermeyer, T. J., Baus, M. & Kurz, H. A graphene field-effect device. arXiv preprint cond-mat/0703208 (2007).
[122] Sinitskii, A. & Tour, J. M. Patterning graphene through the self-assembled templates: toward periodic two-dimensional graphene nanostructures with semiconductor properties. J. Am. Chem. Soc. 132, 14730-14732 (2010).
[123] Wang, M. et al. CVD growth of large area smooth-edged graphene nanomesh by nanosphere lithography. Sci. Rep. , 1238; DOI:10.1038/srep01238 (2013).
[124] Lin, Y.-M., Perebeinos, V., Chen, Z. & Avouris, P. Electrical observation of subband formation in graphene nanoribbons. Phys. Rev. B. 78, 161409 (2008).
[125] Obradovic, B. et al. Analysis of graphene nanoribbons as a channel material for field-effect transistors. Appl. Phys. Lett. 88, 142102 (2006).
[126] Chen, Z., Lin, Y.-M., Rooks, M. J. & Avouris, P. Graphene nano-ribbon electronics. Physica E: Low-dimensional Systems and Nanostructures 40, 228-232 (2007).
[127] Biel, B., Blase, X., Triozon, F. & Roche, S. Anomalous doping effects on charge transport in graphene nanoribbons. Phys. Rev. Lett. 102, 096803 (2009).
[128] Muller, R. S., Kamins, T. I., Chan, M. & Ko, P. K. Device electronics for integrated circuits. (1986).
[129] Chen, J.-H., Jang, C., Xiao, S., Ishigami, M. & Fuhrer, M. S. Intrinsic and extrinsic performance limits of graphene devices on SiO2. Nat. Nanotechnol. 3, 206-209 (2008).
[130] Fang, T., Konar, A., Xing, H. & Jena, D. Mobility in semiconducting graphene nanoribbons: Phonon, impurity, and edge roughness scattering. Phys. Rev. B. 78, 205403 (2008).
[131] Wang, X. et al. Room-Temperature All-Semiconducting Sub-10-nm Graphene Nanoribbon Field-Effect Transistors. Phys. Rev. Lett. 100, 206803 (2008).
[132] Kazemi, A. et al. in Wiley Encyclopedia of Electrical and Electronics Engineering. John Wiley & Sons, Inc., (2014).
[133] Shao, Q., Liu, G., Teweldebrhan, D. & Balandin, A. High-temperature quenching of electrical resistance in graphene interconnects. Appl. Phys. Lett. 92, 202108 (2008).

DISTRIBUTION A: Distribution approved for public release.

1.

1. Report Type

Final Report

Primary Contact E-mail
Contact email if there is a problem with the report.

skrishna@chtm.unm.edu

Primary Contact Phone Number
Contact phone number if there is a problem with the report

505-272-7800

Organization / Institution name

Regents of the University of New Mexico

Grant/Contract Title
The full title of the funded effort.

Heterogenous Material Integration and Band Engineering with Type II Superlattices

Grant/Contract Number
AFOSR assigned control number. It must begin with "FA9550" or "F49620" or "FA2386".

FA9550-10-1-0113

Principal Investigator Name
The full name of the principal investigator on the grant or contract.

Sanjay Krishna

Program Manager
The AFOSR Program Manager currently assigned to the award

Dr. Kenneth Goretta

Reporting Period Start Date

04/15/2010

Reporting Period End Date

10/14/2015

Abstract

InAs/GaSb type-II strained layer superlattice (T2SL) detectors are of great importance for a variety of military and civil applications requiring increased resolution, reliability, and operating temperature, as well as lowered size, weight, power and cost. However, despite extensive efforts on T2SL material growth, detector passivation, and fabrication, T2SL detectors still have not reached the performance level of the Rule 07 for MCT detectors. During this program, the Center for High Technology Materials at the University of New Mexico was investigating high performance heterojunction bandgap engineered infrared focal plane arrays using InAs/GaSb/AlSb strained layer superlattices.

Distribution Statement
This is block 12 on the SF298 form.

Distribution A - Approved for Public Release

Explanation for Distribution Statement
If this is not approved for public release, please provide a short explanation. E.g., contains proprietary information.

SF298 Form
Please attach your SF298 form. A blank SF298 can be found here. Please do not password protect or secure the PDF The maximum file size for an SF298 is 50MB.

DISTRIBUTION A: Distribution approved for public release.

SF-298.pdf

Upload the Report Document. File must be a PDF. Please do not password protect or secure the PDF . The maximum file size for the Report Document is 50MB.

FA955010-1-0113_Final_Report_ver_8-13-2015.pdf

Upload a Report Document, if any. The maximum file size for the Report Document is 50MB.

Archival Publications (published) during reporting period:

Plis, E. InAs/GaSb Type-II Superlattice Detectors. Advances in Electronics 2014 (2014)
DOI/10.1155/2014/246769
E. Plis, B. Klein, S. Myers, N. Gautam, E. P. Smith, and S. Krishna, "High Operating Temperature Midwave Infrared InAs / GaSb Superlattice Photodetectors," IEEE Electron Device Lett., vol. 34, no. 3, pp. 426–428, 2013.
Plis, E., Klein, B., Myers, S., Gautam, N., and Krishna, S.: (111) InAs/GaSb type-II strained layer superlattice material for high operating temperature detection, physica status solidi c 10, 748 (2013)
Fang, H., Bechteld, H. A., Plis, E., Martin, M. C., Krishna, S., Yablonovitch, E., Javey, A. Quantum of optical absorption in two-dimensional semiconductors. Proceedings of the National Academy of Sciences of the United
States of America 110, p. 11688 (2013)
Takei, K., Kapadia, R., Li, Y., Plis, E., Krishna, S., Javey, A. Surface Charge Transfer Doping of IIIV Nanostructures. The Journal of Physical Chemistry C 117, p. 17845 (2013)
Gautam, N., Myers, S.,Barve, A. V., Klein, B., Smith, E. P., Rhiger, D., Plis, E., Kutty, M. N., Henry, N., Schuler-
Sandy, T., Krishna, S.: Band engineered HOT midwave infrared detectors based on type-II InAs/GaSb strained layer
superlattices, Infrared Physics and Technology 59, p. 72 (2013)
Asplund, C., Marcks von Wrtemberg, R.,Lantz, D., Malm, H., Martijn, H., Andersson, J., Plis, E., Gautam, N., and
Krishna, S.: Performance of mid-wave T2SL detectors with heterojunction barriers, Infrared Physics and Technology (2013)
Plis, E., Naydenkov, M., Myers, S., Klein, B., Gautam, N., Krishna, S. S., Smith, E. P., Johnson, S., and Krishna, S.:
Dual-band pBp detectors based on InAs/GaSb strained layer superlattices, Infrared Physics and Technology (2013)
Karim, A., Marcks von Wrtemberg, R., Asplund, C., Malm, H., Andersson, J., Plis, E., and Krishna, S.:
Characterization of InAs/GaSb type-II superlattice photodiodes for mid-wave IR with different mesa sidewall passivation schemes, physica status solidi (c) 9, p. 1690 (2012)
Nah, J., Fang, H., Wang, C.,Takei, K., Lee, M. H., Plis, E., Krishna, S., and Javey, A.: IIIV Complementary metaloxide-
semiconductor electronics on silicon substrates, Nano Letters 12, p. 3592 (2012)
Wang, C., Chien, J.-C., Fang, H., Takei, K., Nah, J., Plis, E., Krishna, S., Niknejad, A. M., and Javey, A.: Selfaligned,
extremely high frequency IIIV metal-oxide-semiconductor field-effect transistors on rigid and flexible substrates, Nano Letters 12, p. 4140 (2012)
N. Gautam, S. Myers, A. V. Barve, B. Klein, E. P. Smith, D. R. Rhiger, L. R. Dawson, and S. Krishna, "High operating temperature interband cascade midwave infrared detector based on type-II InAs/GaSb strained layer
superlattice", Appl. Phys. Lett. 101, 021106 (2012)
H. Fang, S. Chuang, K. Takei, H. S. Kim, E. Plis, C.-H. Liu, S. Krishna, Y.-L. Chueh, and A. Javey, "Ultrathin-Body High-Mobility InAsSb-on-Insulator Field-Effect Transistors", IEEE Electron Device Lett. 33(4), 2012
E. A. Plis, M. N. Kutty, and S. Krishna, "Passivation techniques for InAs/GaSb strained layer superlattice detectors", Laser Photonics Rev., 1–15 (2012)
K. Takei, S. Chuang, H. Fang, R. Kapadia, C.-H. Liu, J. Nah, H. S. Kim, E. Plis, S. Krishna, Y.-L. Chueh, and

A.
Javey "Benchmarking the performance of ultrathin body InAs-on-insulator transistors as a function of body thickness ", Appl. Phys. Lett. 99, 103507 (2011)
S. J. Lee, Z. Ku, A. Barve, J. Montoya, W.-Y. Jang, S.R.J. Brueck, M. Sundaram, A. Reisinger, S. Krishna, and S.
K. Noh, "A monolithically integrated plasmonic infrared quantum dot camera", Nature Communications 2, 286
(2011)
N. Gautam, M. Naydenkov, S. Myers, A. V. Barve, E. Plis, T. Rotter, L. R. Dawson, and S. Krishna, "Three color
infrared detector using InAs/GaSb superlattices with unipolar barriers", Appl. Phys. Lett. 98, 121106 (2011)
B Klein, E Plis, M N Kutty, N Gautam, A Albrecht, S Myers and S Krishna, "Varshni parameters for InAs/GaSb
strained layer superlattice infrared photodetectors", J. Phys. D: Appl. Phys. 44, 075102(2011)
E. Plis, M.N. Kutty, S. Myers, H.S. Kim, N. Gautam, L.R. Dawson, S. Krishna, "Passivation of Long-wave Infrared
InAs/GaSb Strained Layer Superlattice detectors", Infrared Physics & Technology 54, 252 (2011)
H. Ko, K. Takei, R. Kapadia, S. Chuang, H. Fang, P. W. Leu, K. Ganapathi, E. Plis, H. S. Kim, S.Y. Chen, M. Madsen, A. C. Ford, Y.-L. Chueh, S. Krishna, S. Salahuddin, and A. Javey, "Ultrathin compound semiconductor
on insulator layers or high-performance nanoscale transistors", Nature 468 (2010)
Elena Plis, S. Myers, M. N. Kutty, J. Mailfert, E. P. Smith, S. Johnson, and S. Krishna, "Lateral diffusion of minority carriers in InAsSb-based nBn detectors", Appl. Phys. Lett. 97, 123503(2010)
E. A. Plis, M. N. Kutty, S. Myers, A. Rathi, E. H. Aifer, I. Vurgaftman, and S. Krishna, "Performance improvement
of long-wave infrared InAs/GaSb strained-layer superlattice detectors through sulfur-based passivation," Infrared
Phys. Technol., vol. 55, pp. 216–219, 2012.
M. Zamiri, E. Plis, J. O. Kim, S. C. Lee, A. Neumann, S. Myers, E. P. Smith, A. M. Itsuno, J. G. A. Wehner, S. M.
Johnson, S. R. J. Brueck, and S. Krishna, "MWIR superlattice detectors integrated with substrate side-illuminated
plasmonic coupler," in Proc. of SPIE, Infrared Technology and Applications XL, 2014, vol. 9070, no. 90700Y.
C. M. Watts, D. Shrekenhamer, J. Montoya, G. Lipworth, J. Hunt, T. Sleasman, S. Krishna, D. R. Smith, and W. J.
Padilla, "Terahertz compressive imaging with metamaterial spatial light modulators," Nat. Photonics, vol. 8, no. 8,
pp. 605–609, 2014.
E. A. Plis, S. S. Krishna, N. Gautam, S. Myers, and S. Krishna, "Bias switchable dual-band InAs/GaSb superlattice
detector With pBp architecture," IEEE Photonics J., vol. 3, no. 2, pp. 234–240, 2011.
E. Plis, B. Klein, S. Myers, N. Gautam, T. J. Rotter, R. L. Dawson, S. Krishna, S. J. Lee, and Y. H. Kim, "Type-II
InAs/GaSb strained layer superlattices grown on GaSb (111)B substrate," J. Vac. Sci. Technol. B, vol. 31, no. 3, p.
03C123, 2013.
T. Schuler-Sandy, S. Myers, B. Klein, N. Gautam, P. Ahirwar, Z.-B. Tian, T. Rotter, G. Balakrishnan, E. Plis, and S.
Krishna, "Gallium free type II InAs/InAsxSb1-x superlattice photodetectors," Appl. Phys. Lett., vol. 101, no. 7, p.
071111, Aug. 2012.
B. Klein, N. Gautam, E. Plis, T. Schuler-sandy, T. J. Rotter, S. Krishna, B. Connelly, G. D. Metcalfe, P. Shen,

and
M. Wraback, “Carrier lifetime studies in midwave infrared type-II InAs / GaSb strained layer superlattice,” J. Vac.
Sci. Technol. B, vol. 32, no. 2, p. 02C101, 2014.
G. A. Umana-Membreno, B. Klein, H. Kala, J. Antoszewski, N. Gautam, M. N. Kutty, E. Plis, S. Krishna, and L.
Faraone, “Vertical minority carrier electron transport in p-type InAs/GaSb type-II superlattices,” Appl. Phys. Lett.,
vol. 101, no. 25, p. 253515, 2012.
B. Klein, PhD Thesis, 2014
E. Plis, B. Klein, N. Gautam, S. Myers, M. N. Kutty, M. Naydenkov, S. Krishna. Proc. SPIE 8012, 80120V (2011)
N. Gautam, PhD Thesis, 2012
Z.-B. Tian, S. E. Godoy, H. S. Kim, T. Schuler-Sandy, J. A. Montoya, and S. Krishna. Appl. Phys. Lett. 105, 051109 (2014)
N. Gautam, H. S. Kim, M. N. Kutty, E. Plis, L. R. Dawson, and S. Krishna, “Performance improvement of longwave
infrared photodetector based on type-II InAs/GaSb superlattices using unipolar current blocking layers,” Appl. Phys.
Lett., vol. 96, no. 231107, p. 231107, 2010.
B. Klein, N. Gautam, S. Myers, and S. Krishna, “Temperature-dependent absorption derivative on InAs/GaSb Type
II superlattices,” Proc. SPIE, vol. 8353, 2012.
B. Klein et al., Post-etching mesa surface composition investigation of InAs/GaSb type-II strained layer super lattices using XPS
characterization, Infrared Phys. Technol. (2014), http://dx.doi.org/10.1016/j.infrared.2014.10.010.

Changes in research objectives (if any):

Change in AFOSR Program Manager, if any:

Program Manager changed from Dr. Kitt Reinhardt to Dr. James Hwang to Dr. Kenneth Goretta

Extensions granted or milestones slipped, if any:

NCE granted through 10/14/2015

AFOSR LRIR Number

LRIR Title

Reporting Period

Laboratory Task Manager

Program Officer

Research Objectives

Technical Summary

Funding Summary by Cost Category (by FY, $K)

	Starting FY	FY+1	FY+2
Salary			
Equipment/Facilities			
Supplies			
Total			

Report Document

Report Document - Text Analysis

DISTRIBUTION A: Distribution approved for public release.

Report Document - Text Analysis

Appendix Documents

2. Thank You

E-mail user

Oct 20, 2015 17:14:01 Success: Email Sent to: skrishna@chtm.unm.edu

DISTRIBUTION A: Distribution approved for public release.